THE EFFECT OF SUBSURFACE MASS LOSS ON THE RESPONSE OF SHALLOW FOUNDATIONS

A Thesis
Presented to
The Academic Faculty

by

Song-Hun Chong

In Partial Fulfillment
of the Requirements for the Degree
Doctor of Philosophy in the
School of Civil and Environmental Engineering

Georgia Institute of Technology
December 2014

THE EFFECT OF SUBSURFACE MASS LOSS ON THE RESPONSE OF SHALLOW FOUNDATIONS

Approved by:

Dr. J. Carlos Santamarina, Advisor
School of Civil and Environmental Engineering
Georgia Institute of Technology

Dr. Chloé Arson
School of Civil and Environmental Engineering
Georgia Institute of Technology

Dr. Paul W. Mayne
School of Civil and Environmental Engineering
Georgia Institute of Technology

Dr. Christian Huber
School of Earth and Atmospheric Sciences
Georgia Institute of Technology

Dr. Susan E. Burns
School of Civil and Environmental Engineering
Georgia Institute of Technology

Date Approved: August 11, 2014

Be humble in the face of nature

S.H. Chong (1980 - …)

ACKNOWLEDGEMENTS

I wish to extend my sincere appreciation to many people who have made my Ph.D. work possible during my four years at the Georgia Tech. To my advisor, Dr. J. Carlos Santamarina, I extend my deepest gratitude for his sustained support, advice, and sincere criticism. I have frequently been impressed by his knowledge, passion, curiosity, and dedication. Without his guidance, I would not have achieved the level of intellectual and professional development that I have. Also, I want to thank Cecilia and Francisco for thoroughly proofreading my thesis.

I would also like to thank my committee members, Dr. Paul W. Mayne, Dr. Susan E. Burns, Dr. Chloe Arson, and Dr. Christian Huber, for insightful comments and invaluable suggestions. I am also thankful to Dr. Gye-Chun Cho and Dr. Seong-Wan Park who have prepared me as a scholar.

This research was supported by the SRS project under contract from the U.S. Department of Energy, under the leadership of Dr. B. Gutierrez. NRC and external reviewers provided most valuable guidance and feedback. Additional funding was provided by the Goiuzeta Foundation.

Wonderful interactions with the past and current members of the PMRL have enriched my mind and personal life. It has been a privilege to be part of this research group. I am sure that this is the beginning of long-lasting friendships.

Finally, I would like to thank my parents and parents-in-law for their dedicated support and great trust. Above all, I want to thank my precious wife – Heamin, my energetic son – Woosung, my princesses – Jiwoo and Lena for all their sacrifice and patience. Without them, I could not have completed this work.

TABLE OF CONTENTS

LIST OF TABLES

LIST OF FIGURES

SUMMARY

Subsurface volume loss takes place in many geotechnical situations, and it is inherently accompanied by complex stress and displacement fields that may influence the performance of engineered geosystems. This research is a deformation-centered analysis, it depends on soil compressibility and it is implemented using finite elements.

Soil stiffness plays a central role in predicting ground deformation. First, an enhanced Terzaghi's soil compressibility model is proposed to satisfy asymptotic conditions at low and high stress levels with a small number of physically meaningful parameters. Then, the difference between small and large strain stiffness is explored using published small and large-strain stress-strain data. Typically, emphasis is placed on the laboratory-measured stiffness or compressibility; however, there are pronounced differences between laboratory measurements and field values, in part due to seating effects that prevail in small-thickness oedometer specimens. Many geosystems are subjected to repetitive loads; volumetric strains induced by drained repetitive ko-loads are experimentally investigated to identify shakedown and associated terminal density.

The finite element numerical simulation environment is used to explore the effect of localized subsurface mass loss on free-surface deformation and shallow foundations settlement and bearing capacity. A stress relaxation module is developed to reproduce the change in stress associated to dissolution features and soft zone formation. The comprehensive parametric study is summarized in terms of dimensionless ratios that can be readily used for engineering applications.

Field settlement data gathered at the Savannah River Site SRS are back-analyzed to compare measured values with predictions based on in situ shear wave velocity and strain-dependent stiffness degradation. The calibrated model is used to estimate additional settlements due to the pre-existing cavities, new cavities, and potential seismic events during the design life of the facility.

CHAPTER 1

INTRODUCTION

Subsurface volume loss results from natural processes (dissolution, piping erosion, and grain migration) and man-made processes (e.g., mining, tunneling, energy geo-storage systems, CO_2 injection driven dissolution, and resource recovery such as dissociation of methane hydrates). The removal of solid mass inevitably causes stress relaxation and influences the performance of engineered geosystems.

The sediments of the Atlantic Coastal Plain in the vicinity of the Savannah River Site (SRS) consist of quartz sand, clay, limestone, other carbonates, and conglomerate ranging in age from the late Cretaceous to the Holocene. Multiple site investigation studies have shown a complex stratigraphy that resulted from marine and fresh-water depositional environments, including the presence of dissolved cavities and soft zones (WSRC, 1999; Burns and Roe Enterprises, 2001; Shannon and Wilson, 2007; WSRC, 2007; see also Kochanov, 1999).

Subsurface volume loss leads to complex stress and displacement fields which depend on stratigraphy, mechanical parameters (density, stiffness, cementation, diagenesis, and preconsolidation), hydro-geological conditions, the extent of removed mass, depth, and load-dissolution histories (i.e., whether load is applied before or after dissolution). General conclusions may not be provided for such a complex system and simple analytical solutions fail to capture emerging effects and governing parameters. Consequently, numerical simulations are needed to study the implications of soft zone formation in the subsurface.

Dissolution cavities and soft zones in the subsurface at the Savannah River Site (SRS) raise concerns about their potential impact on near-surface infrastructure. The

main objectives of this research are to develop a robust methodology to model localized stress relaxation associated with dissolution features and soft zone formations, to select adequate constitutive models, and to properly calibrate them using laboratory and field data. A case history at the SRS is used for site-specific validation and subsurface model calibration, and is followed by comprehensive simulations of hypothetical cases relevant to the SRS. The thesis is organized around three main themes into the following seven chapters:

I. Physical properties: Stiffness

- Chapter 2 proposes a soil compressibility model based on Terzaghi's equation, which is modified to satisfy asymptotic conditions at low and high stress with a small number of physically meaningful parameters. The modified Terzaghi's equation is validated against an extensive consolidation dataset, which includes remolded clayey soils and natural sedimentary clays.
- Chapter 3 explores the relationship between small and large strain stiffness. Concurrent small and large-strain stress-strain data are collected from the literature including resonant column tests, triaxial tests, and oedometer tests. The small strain stiffness at constant fabric is then compared against the large strain stiffness measured as fabric changes.
- Chapter 4 reports results of an experimental program designed to explore the evolution of volumetric strain during drained repetitive k_o-loads. Emphasis is placed on identifying soil plastic shakedown associated with terminal density.

II. Subsurface volume contraction - Preliminary studies

- Chapter 5 develops the stress relaxation module to simulate dissolution and soft zone formation within a finite element numerical approach. A comprehensive parametric study is performed to explore the effect of various parameters for

different subsurface conditions (soft zone depth z_0, number of nearby soft zones, constant volume shear friction angle ϕ_{cs}, preconsolidation, and internal stress reduction).

- Chapter 6 explores the effect of subsurface volume contraction on shallow foundations. The parametric study considers footing size B, soft zone location D, dilation angle ψ, and load-dissolution history (i.e., stress relaxation-before-footing and footing-before-stress relaxation).

III. SRS Project

- Chapter 7 documents a simple and robust back analysis procedure for shallow foundations. It includes the selection of adequate constitutive models, subsurface model calibration using laboratory and field data, and site-specific validation.
- Chapter 8 reports a comprehensive study of a hypothetical shallow foundation system at SRS using the subsurface model calibrated in Chapter 7.

Finally, Chapter 9 summarizes salient conclusions of this study.

CHAPTER 2

SOIL COMPRESSIBILITY: PHYSICS INFORMED MODEL

2.1 Introduction

Soils subjected to vertical loading under zero lateral strain conditions always experience contraction regardless of soil type, effective stress level, or prior diagenetic process. Soil compressibility relates the effective stress to volume change, and reflects the loading and long geological history of the sediment. Soil compressibility models are needed for settlement analysis in classical geotechnical design (e.g., foundation, embankment, and ground pumping) and energy geotechnology practice (e.g., oil extraction, long offshore piles, wind turbines, and hydrate bearing sediments).

Suggested soil compressibility models include logarithmic, polynomial, and power law functions. However, these functions lead to unacceptable asymptotic values such as infinite void ratio at $\sigma' \rightarrow 0$, or negative void ratio at high stresses. Clearly, both asymptotic trends are physically incorrect. Thus, an alternative expression is sought in this chapter and tested against an extensive dataset of consolidation tests.

2.2 Previous studies

General 1D soil compression behavior

Sediment compressibility is often analyzed using semi-logarithmic plots. Consolidation data collected from the literature for a wide range of soil mineralogy are shown in Figure 2.1. Compression curves show that finer particles have higher void ratio e_{1kPa} when the confining stress is $\sigma' = 1$ kPa and steeper slope i.e., higher compressibility C_c. Clearly, e_{1kPa} is proportional to C_c. Ultimately, all sediments converge towards a

similar state condition at high stress ($\sigma' \approx 10$ MPa). The complete database used in this study is tabulated in Table 2.1.

Many studies have been performed to assess the effect of soil structure on the mechanical behavior of sedimentary clays, to clarify the difference between natural clays and remolded clays, and to use the compressibility of remolded clays as a basis for the interpretation of the compression characteristic of natural sedimentary clays (Casagrande, 1936; Skempton, 1944; Terzaghi and Peck, 1948; Schmertmann, 1955; Kaufman and Sherman, 1964; Quigley and Thompson, 1966; Leroueil et al., 1979; Walton et al., 1983; Leroueil et al., 1985; Burland, 1990; Schmertmann, 1991; Cotecchia and Chandler, 1997; Cotecchia and Chandler, 2000; Hong et al., 2006; Hong et al., 2012).

Remolding erases the structuring effects, hence, the compression curve of the natural sedimentary clays plots above (i.e., higher void ratio) than the trend for remolded clayey soils. Leroueil et al. (1985) divides the compression characteristics of natural sedimentary clays into intact and destructured states. Hong et al. (2012) separates the destructured states related to the breakage of the natural clay structure into two transitional states.

Low stress regime $\sigma' < \sigma'_L$. The compression characteristics of natural sedimentary clays at low stress $\sigma' < \sigma'_L$ reveal post-depositional diagenetic changes that combine fabric and bonding effects (Mitchell, 1976; Burland, 1990; Rinaldi and Santamarina, 2008). Diagenetic processes include mechanical actions (e.g., erosion, past glaciations, and excavation or removal of prior structure, moisture fluctuations, clay migration and flocculation), thermal processes (thermo-osmosis and thermal cyclic loading), and chemical processes (e.g., dissolution, particle reprecipitation, thixotropic hardening, fluid viscosity, mineral transformation, weathering, leaching, van der Waals attraction, and ionic concentration). These processes have pronounced effects on the compressibility of natural sedimentary clays.

Intermediate stress regime $\sigma'_L < \sigma' < \sigma'_H$. The stress regime $\sigma'_L < \sigma' < \sigma'_H$ is of main interest in classical geotechnical practice. Many studies have empirically correlated compressibility characteristics with index properties. In particular, the compression index C_c has a strong correlation with the liquid limit LL, or the void ratio at the liquid limit e_{LL} (Skempton, 1944; Terzaghi and Peck, 1948; Burland, 1990; Sridharan and Nagaraj, 2000). Prior coupled processes still influence the soil compression characteristics in this stress regime including the effects of cementation and aging (Mesri et al., 1975; Schmertmann, 1983; Schmertmann, 1984; Schmertmann, 1991), initial water content $w_{initial}$ (Hong et al., 2010; Hong et al., 2012), and the temperature (Campanella and Mitchell, 1968; Baldi et al., 1988; Leroueil, 1996; Sultan et al., 2002). In addition, consolidation curves are affected by experimental procedures such as sampling disturbance (Casagrande, 1936; Terzaghi and Peck, 1948; Schmertmann, 1955; Rochelle et al., 1981; Hight et al., 1992; Santagata and Germaine, 2002) and imposed strain rate (Hanzawa, 1989; Leroueil, 1996; Leoni et al., 2008).

High stress regime $\sigma' > \sigma'_H$. At high stress, particle compressibility and creep effects prevail in sedimentary volume changes (Barden, 1965; Mesri and Godlewski, 1977; Mesri and Castro, 1987). Past history looses relevance, and the sediments converge to a similar condition regardless of their natural sedimentary clay or remolded clay origin, as shown in Figure 2.1 (Terzaghi and Peck, 1948; Chilingar and Knight, 1960; Skempton, 1969; Burland, 1990; Hong et al., 2012). The evolution of porosity at high stress can be expressed by using either exponential or power law functions (Athy, 1930; Aplin et al., 1995).

Soil compressibility models

Compressibility at the molecular scale – Gases. Boyle's law assumes no molecular size and no interactions, and concludes that pressure and volume are related as:

$$PV=\alpha \rightarrow V=\alpha/P \qquad (2.1)$$

van der Waals corrected this expression to take into consideration the size of molecules and re-wrote Boyle's equation in terms of the volume that can contract V', i.e., the total volume V_{total} minus the volume "excluded" $V_{excluded}$ by the molecules, $V'=V_{total}-V_{excluded}$. He also considered intermolecular interactions and the additional stress due to uncompensated attraction at the boundaries.

From gases to soils - Power function. Following a parallel analysis, and taking into consideration electrical interaction forces in fine grained soils $\sigma_A - \sigma_R$, a proper equation for soil compressibility becomes

$$\left(\sigma' + \sigma_A - \sigma_R\right)\left(V_{total} - V_{solids}\right) = \alpha \qquad (2.2)$$

If the volume of solids is assumed constant, this equation can be written in terms of void ratio $e = (V_{total}-V_{solids})/V_{solids}$ and becomes

$$\left(\sigma - u + \sigma_A - \sigma_R\right)e = \alpha' \qquad (2.3)$$

Therefore, there is an inverse relationship with void ratio e and effective stress σ' (Table 2.2). Similar equations have been suggested for isotropic compression of soils. Power expressions lead to infinite void ratio as the $\sigma' \rightarrow 0$ unless a minimum lower stress is included, for example to consider electrical force.

Empirical polynomial fit. Burland (1990) compiled void ratio data with depth in natural sediments and oedometric data gathered with remolded specimens. Data trends show that the void ratio decreases linearly with the logarithm of effective stress at intermediate stress (similar to Terzaghi's equation) but at a lower rate at high stress. Based on remolded clay data, he proposed a polynomial relationship between e and log (σ) with both with linear and cubic terms. Asymptotic values for low and high stress levels are

physically inadequate; in fact, this equation predicts an increase in void ratio at high stress.

S-shaped curves. Sigmoidal functions define inverse S-shaped trends with two asymptotes. The basic assumption is that the rate of growth is defined by the current state of growth (Gompertz, 1825); this model resembles the effective stress-dependent compression behavior of soils. The integral of Gompertz function is the sigmoid function, but it is asymmetric at the inflection point (Berger, 1981; Baumgartl and Köck, 2004; Gregory et al., 2006). The arctangent function satisfies the two asymptotic requirements but it is symmetrical. The arctangent function can be modified by enforcing two boundary conditions. Both sigmoid and arctangent functions were tested in this study. Results show some deviations in all cases (Figure 2.2). The rest of this analysis places emphasis on semi-log functions, in line with the prior geotechnical experience.

Semi-logarithmic. The classical e-log(σ') trend fits the soil response closer than the power expression derived from the gas law. This semi-logarithmic expression implies that the sediment compressibility $d\sigma'/d\varepsilon$ scales linearly with effective stress $d\sigma'/d\varepsilon=2.3(1+e)\ (\sigma'/C_c)$. This linear scaling highlights frictional resistance to volume contraction as captured in Coulomb's relation $\tau=\sigma'\tan\phi$.

2.3 Proposed model - Examination

Guiding objectives

The 1D soil compression under zero lateral strain conditions shows a nonlinear effective-stress dependent response; the inverse S-shaped trend has two asymptotes at low stress $\sigma' < \sigma'_L$ and high stress $\sigma' > \sigma'_H$. A single 1D soil compressibility model criterion is sought that:

- Uses a small number of physically meaningful parameters (Ockham's criterion). A large number of parameters improve data fitting, but input parameters lack a physical basis and the model lacks robustness (Santamarina and Fratta, 2005). Hardin's (1987) model has 7 parameters.
- Satisfies asymptotic trends at low and high stresses.
- Benefits from the accumulated knowledge in the field.

Enhanced Terzaghi's equation

The classical semi-logarithmic model predicts $e \to \infty$ as $\sigma' \to 0$ and $e < 0$ as $\sigma' \to \infty$. We modify Terzaghi's equation to accommodate asymptotic conditions at low and high stresses

$$e = e_{ref} - C_c \log\left(\frac{\sigma_{ref}'}{\sigma' + \sigma_L'} + \frac{\sigma_{ref}'}{\sigma_H'} \right)^{-1} \tag{2.4}$$

The enhanced Terzaghi's equation involves four parameters: σ'_L and σ'_H are the low and high stresses, C_c is the compression index, and e_{ref} is the reference void ratio at σ' = 1kPa. The lower and upper void ratio plateaus e_L and e_H that correspond to the asymptotic stresses σ'_L and σ'_H are obtained from equation 2.4

$$\sigma_H' = \sigma_{ref}' \cdot 10^{\frac{e_{ref} - e_H}{C_c}} \qquad \text{when } \sigma' \to \infty \tag{2.5a}$$

$$\sigma_L' = \frac{\sigma_H'}{10^{\frac{e_L - e_H}{C_c}} - 1} \qquad \text{when } \sigma' \to 0 \tag{2.5b}$$

Figure 2.3 shows that the proposed model properly captures the 1D soil compression response in the full stress range.

Model examination

Preliminary tests. The enhanced Terzaghi's equation is preliminary tested by fitting remolded and undisturbed clayey soil data. Results show that the proposed model adequately captures the compression trends from low- to high- stress regimes in all cases (Figure 2.4). The selected dataset show more brittle behavior of natural sediments, and the effects of ion type, ionic concentration, and pH (Mesri and Olson, 1971; Santamarina et al., 2001); in particular, high-valent cations and high-ionic concentration promotes denser packing as predicted by double layer based analysis.

Remolded vs. Natural clays. An extensive 1D consolidation dataset was compiled. It includes data for remolded clays and natural sedimentary clays. However, the bilinear compression trends obtained with high sensitive clays are not included. Fitting parameters are obtained within the available effective stress ranges. Empirical relations between C_c and e_{1kPa} are established for remolded clayey soils and natural sedimentary clays (Figure 2.5).

$$e_{1kPa} = 3.4 \cdot C_{c-remolded} + 0.48 \qquad \textit{for remolded clayey soils} \qquad (2.6a)$$

$$e_{1kPa} = 3.1 \cdot C_{c-natural} + 0.48 \qquad \textit{for natural sedimentary clays} \qquad (2.6b)$$

The high correlation between C_c and e_{ref} suggest a lower level of model complexity: from 4 unknowns to almost 3 unknowns. Everything else being equal, these conditions suggest the impact of sampling on the soil compressibility to be about $C_{c\text{-natural}} \approx 1.1 C_{c\text{-remolded}}$ due to destructuring. Structures of remolded clayey soils evolve during kneading and involve the interparticles slippage, while the natural sedimentary clays are laid down grain by grain. These compressibility relations confirm that laboratory tests provide an upper bound for compressibility of natural sedimentary clays.

Figure 2.6 shows the relations between compression index and liquid limit for the remolded clayey soils

$$C_{c-remolded} = 0.008 \cdot \lfloor LL - 10 \rfloor \qquad \textit{for remolded clayey soils} \qquad (2.7)$$

This trend resembles well-known empirical equation for remolded clayey soils (Skempton, 1944) and natural sedimentary clays (Terzaghi and Peck, 1948), and highlights the variation of the compression index with LL ranges.

2.4 Discussion

Large-strain tangential stiffness. For undisturbed, remolded-aged, and remolded clays, the consolidation curves in Figure 2.7(a) show that diagenesis and cementation constrain the elastic deformation and extend the low stress regime. In particular, the sudden change in the compression index for the undisturbed clay reflects the brittle nature of the natural structure (Mesri et al., 1975; Dìaz-Rodrìguez et al., 1992). The derivative of the stress-strain trend defines the tangent modulus (Table 2.2). The tangent 1D constrained modulus is estimated using the fitted trend [Figure 2.7(b)]. Clearly, the early diagenesis process induces higher stiffness, and subsequent loading breaks the interparticle bonds. The tangential constrained modulus of undisturbed clays appears to asymptotically approach that of remolded clays at large strains.

Practical application. If sedimentary clays, the compressibility depends on complex processes, and the settlement can only approximated (Carrier and Beckman, 1984). There are many methods to determine the yield stress or preconsolidation (Casagrande, 1936; Janbu, 1969; Pacheco, 1970; Sallfors, 1975; Butterfield, 1979; Becker et al., 1987; Oikawa, 1987; Jose et al., 1989; Sridharan et al., 1991; Onitsuka et al., 1995; Grozic et al., 2003; Clementino, 2005; Ku and Mayne, 2013). These methods lead to large deviation among yield stress values, which affects the reliable calculation of settlement (Boone, 2012). The proposed stress-strain model explicitly contains preloading effect, and graphical interpretations are not required for the estimation of the yield stress.

2.5 Conclusions

Various soil compressibility models have been suggested; semi-log, polynomial, and power law functions. However, these functions fail to capture asymptotic trends, and can predict infinite void ratio as the stress approaches $\sigma' \rightarrow 0$, or negative void ratio at high stresses. Clearly, both asymptotic trends are physically incorrect. Thus, we propose an alternative expression by adopting a modified version of Terzaghi's equation which accommodates asymptotic conditions at low and high stress. The model is fitted to data gathered for the remolded clays and natural sedimentary clays. Results show that the proposed model captures the 1D soil compression behavior in a wide range of stress. The compression curve of natural sedimentary clays plots above that of remolded clayey soils until the effective stress is below the σ'_H. The compression index for remolded clays and natural clays is related as $C_{c\text{-natural}} \approx 1.1 C_{c\text{-remolded}}$. The trends converge at high stress. For settlement analysis, the compressibility equation is more suitable than the conventional method when a large stress range was involved. This is because the proposed model explicitly included preloading effects without the need for graphical interpretation of the preconsolidation stress.

Table 2.1. Soil type and fitted parameters from proposed model.

(a) Remolded clayey soils

	Soil type	LL [%]	e_{ref} [ ]	Cc [ ]	References
1	Kleinbelt Ton	127	4.19	1.0	Burland (1990)
2	Argile plastique	128	3.55	0.87	
3	London clay	77	2.16	0.47	
4	Wiener Tegel	46.7	1.46	0.30	
5	Magnus Clay	35	1.27	0.25	
6	Lower Cromer Till	25	0.84	0.17	
7	Bothkennar soil from 6.5m depth	-	2.44	0.54	
8	Sail clay	159	5.10	1.17	Nagaraj and Murthy (1986)
9	Black cotton clay	97.3	3.44	0.85	
10	Boston blue clay	39	1.24	0.21	
11	Whangamarino clay	136	3.34	0.82	
12	Red soil	45.3	1.28	0.25	
13	Silty clay	56.4	1.58	0.30	
14	Vienna clay	47	1.41	0.28	
15	Silty clay	36.2	0.96	0.16	
16	Soft clay	78	2.60	0.55	
17	Townsville 1	86	3.15	0.87	Morris (2002)
18	Rosslyn Bay 2	46	1.73	0.44	
19	Urangan 1	53	1.90	0.51	

20	Brisbane River 1		37	1.25	0.30	
21	Brisbane River 2		79	2.88	0.74	
22	Brisbane River 3		99	3.20	0.81	
23	Manly 1		103	3.40	0.94	
24	Coomera River 2		62	2.35	0.62	
25	Nerang Canals 3		53	1.65	0.41	
26	Ariake clay		-	2.65	0.64	Hong et al. (2006)
27	Oita Diatomite		-	2.85	0.76	
28	Clay		-	1.43	0.28	Karig and Hou (1992)
29	Savannah River 1		24	0.85	0.05	In this study
30	Savannah River 2		200	5.60	1.57	In this study
31	Kaolinite and Bentonite		100	3.94	0.93	Griffiths and Joshi (1990)
32	Kaolinte		45	2.56	0.59	
33	Montmorillonite and Quartz		74	1.32	0.16	Sridharan and Nagaraj (2000)
34	Illite and Quartz		39	1.25	0.23	
35	Lianyungang clay	$w_{initial}$ = 50%	74	1.72	0.36	Hong et al. (2010)
36		$w_{initial}$ = 59 %		1.92	0.42	
37		$w_{initial}$ = 68 %		2.10	0.47	
38		$w_{initial}$ = 78 %		2.38	0.55	
39		$w_{initial}$ = 85 %		2.65	0.69	
40		$w_{initial}$ = 119 %		3.12	0.83	
41		$w_{initial}$ = 135 %		3.20	0.94	

42	Baimahu clay	$w_{initial}$ = 72 %	91	2.33	0.55	
43		$w_{initial}$ = 64 %		2.23	0.50	
44		$w_{initial}$ = 83 %		2.51	0.61	
45		$w_{initial}$ = 91 %		3.00	0.80	
46		$w_{initial}$ = 101 %		3.13	0.83	
47		$w_{initial}$ = 143 %		3.21	0.81	
48		$w_{initial}$ = 180 %		3.47	0.85	
49	Kemen clay	$w_{initial}$ = 122 %	61	2.60	0.61	
50		$w_{initial}$ = 99 %		2.33	0.53	
51		$w_{initial}$ = 80 %		2.10	0.50	
52		$w_{initial}$ = 66 %		1.80	0.38	
53		$w_{initial}$ = 48 %		1.49	0.28	
54		$w_{initial}$ = 43 %		1.43	0.26	

	Soil type	**e_L [ ]**	**e_{ref} [ ]**	**Cc [ ]**	**References**
55	Na Montmorillonite (0.001 N and pH=7)	36.0	47.5	18.5	Mesri and Olson (1971)
56	Ca Montmorillonite (0.001 N and pH=7)	7.3	8.7	3.1	
57	Na Montmorillonite (0.1 N and pH=7)	21.4	31.5	12.3	
58	Ca Montmorillonite (0.001 N and pH=5)	9.3	10.8	4.5	
59	Mexico City Clay	10.2	16.0	4.4	Mesri et al. (1975)
60	Mexico City Clay (Aged)	10.6	18.0	5.0	

(b) Natural sedimentary clays

	Soil type	e_L [ ]	e_{ref} [ ]	C_c [ ]	Reference
1	Port Allen clay	1.00	2.20	0.46	Boone (2010)
2	New Liskeard clay	1.63	4.70	1.30	
3	Sault Ste. Marie clay 1	2.00	4.40	1.20	
4	Sault Ste. Marie clay 2	1.64	4.45	1.30	
5	Sault Ste. Marie clay 3	1.48	2.90	0.70	
6	Sault Ste. Marie clay 4	1.44	2.80	0.75	
7	Ontario soil 1	0.85	1.31	0.24	
8	Ontario soil 2	0.45	0.77	0.14	
9	Haltenbanken clay	0.43	0.74	0.12	Grozic et al. (2003)
10	Busan A	1.46	2.30	0.67	Yoon et al. (2011)
11	Incheon A	1.04	1.51	0.29	
12	Kwangyang A	1.19	1.62	0.35	
13	Beaufort sea silty clay	0.84	1.33	0.22	Becker et al. (1987)
14	Wallaceburg clay 1	1.22	1.94	0.41	
15	Wallaceburg clay 2	1.12	2.31	0.55	
16	Bothkennar soil from 6.5m	1.98	4.40	1.40	Burland (1990)
17	Black shale	0.32	0.52	0.07	Hendron et al. (1969)
18	Gray shale	0.30	0.42	0.06	
19	Saguenay clay 1	3.32	5.25	1.51	Perret et al. (1995)
20	Saguenay clay 2	2.63	4.18	1.10	

21	Saguenay clay 3	2.40	3.58	1.00	
22	Saguenay clay 4	2.21	2.45	0.60	
23	Saguenay clay 5	1.72	2.30	0.50	
24	Mexico City Clay	11.0	22.4	6.5	Mesri et al. (1975)

Table 2.2. Comparisons of soil compressibility models

	References	Parameters	Equations	Tangent Modulus M or K (*)	Problems
Semi - log	*k_o load* Terzaghi and Peck (1948)	e_{ref}, C_c (2)	$e = e_{ref} - C_c \log\left(\frac{\sigma'}{\sigma_{ref}'}\right)$ *loading & unloading*	$M = 2.3\frac{(1+e)}{C_c}\sigma'$	Asymptotes $\sigma' \rightarrow 0$ ➔ $e \rightarrow \infty$ $\sigma' \rightarrow \infty$ ➔ $e < 0$
	Isotropic load Schofield and Wroth (1968)	v_{ref}, κ (2)	$v = v_{ref} - \kappa \ln\left(\frac{p'}{p_{ref}'}\right)$ *loading & unloading*	$K = \frac{v}{\kappa}p'$	
	k_o load This study	e_{ref}, C_c, $\sigma'_{L,}$ σ'_H (4)	$e = e_{ref} - C_c \log\left(\frac{\sigma_{ref}'}{\sigma'+\sigma_L'} + \frac{\sigma_{ref}'}{\sigma_H'}\right)^{-1}$	$M = \ln(10)\frac{(1+e)}{C_c}(\sigma'+\sigma'_L)\left(1+\frac{\sigma'+\sigma'_L}{\sigma'_H}\right)$	Satisfies low and high stress asymptotes
Power	*k_o load* Hansen, 1969; Juárez-Badillo, 1981; Pestana and Whittle, 1995	e_{ref}, β (2)	$e = e_{ref}\left(\frac{\sigma'}{\sigma_{ref}'}\right)^{-\beta}$ *loading & unloading*	$M = \frac{1}{n\beta}\sigma'$	Solves $\sigma' \rightarrow \infty$ asymptote Modulus independent of volume change
	Isotropic load Butterfield, 1979; Houlsby and Wroth, 1991; Pestana and Whittle, 1995	v_{ref}, β (2)	$v = v_{ref}\left(\frac{p'}{p_{ref}'}\right)^{-\beta}$ *loading & unloading*	$K = \frac{1}{\beta}p'$	

Polynomial	*k_o load* Burland (1990)	e_{ref}, α, β (3)	$e = e_{ref} - \alpha \cdot \log\left(\frac{\sigma'}{\sigma_{ref}'}\right) + \beta \cdot \left[\log\left(\frac{\sigma'}{\sigma_{ref}'}\right)\right]^3$ *loading*	$M = \ln(10)(1+e)\frac{\sigma'}{\alpha - 3\beta\left[\log\left(\frac{\sigma'}{\sigma_{ref}'}\right)\right]^2}$	Wrong low and high stress asymptotes
Other	*k_o load* Gompertz function Gompertz (1825)	e_L, C_c, α, β (4)	$e = e_L - C_c\left[1 - \exp^{-\alpha\left(\frac{\sigma'}{\sigma_{ref}'}\right)^{\beta}}\right]$ *loading & unloading*	$M = \frac{(1+e)}{(e - e_L + C_c)}\frac{\left(\frac{\sigma'}{\sigma_{ref}'}\right)^{1-\beta}}{\alpha\beta}$ kPa	Satisfies low and high stress asymptotes
	k_o load arctangent function (Goldsztein)	e_L, e_H , α, β (4)	$e = \frac{e_L + e_H}{2} + \frac{e_L - e_H}{\pi}.\arctan\left(\frac{\alpha - \frac{\sigma'}{\sigma'_{ref}}}{\beta}\right)$ *loading & unloading*	$M = \frac{\pi(1+e)b}{e_L - e_H}\left[1 + \left(\frac{\alpha - \frac{\sigma'}{\sigma'_{ref}}}{\beta}\right)^2\right]$ kPa	Satisfies low and high stress asymptotes

(*) Note:

1. $M = \frac{\partial\sigma'}{\partial\varepsilon} = \frac{-\partial\sigma'}{\partial e}(1+e)$ and $K = \frac{dp'}{d\varepsilon_v} = \frac{-dp'}{dv}v$

2. *e* is the void ratio, e_{ref} is reference void ratio corresponding to the reference effective stress σ_{ref} = 1 kPa, σ is the applied effective stress, and β is related to the compressibility.

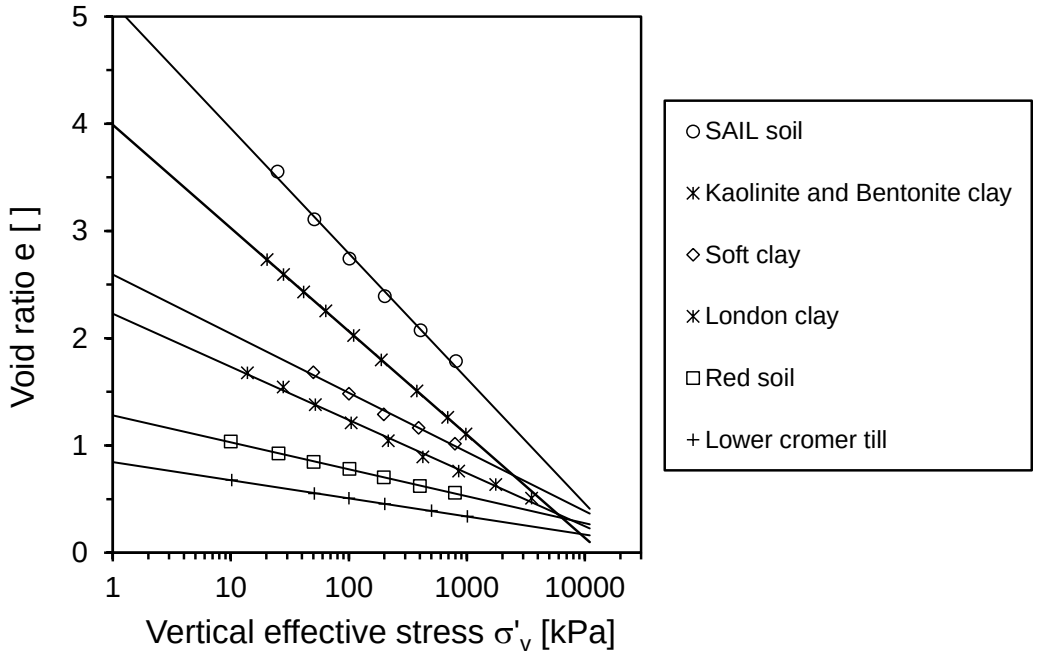

Figure 2.1. Void ratio vs. vertical effective stress relation. Consolidation data for remolded clayey soils: Data source - Burland (1990).

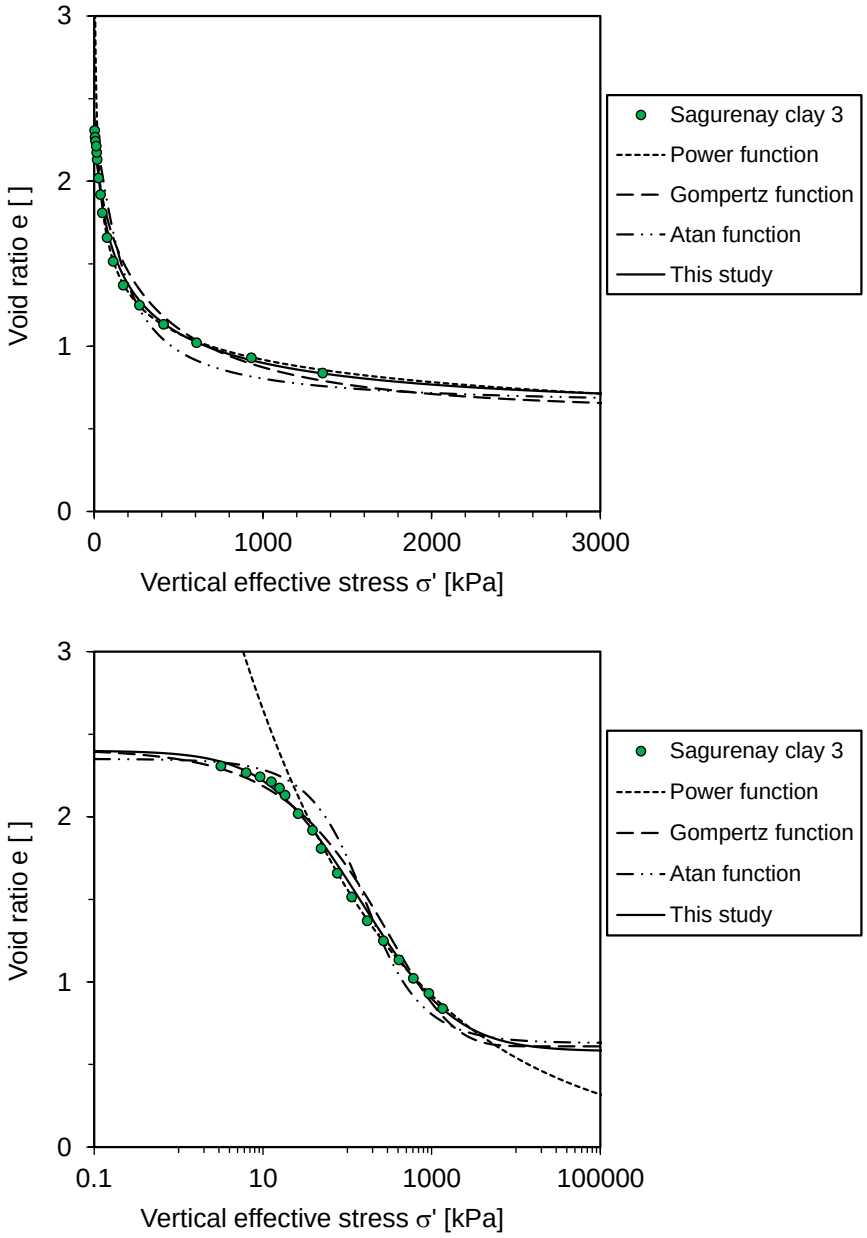

Figure 2.2. Comparison of 1D soil compressibility models. Data source: Perret et al. (1995).

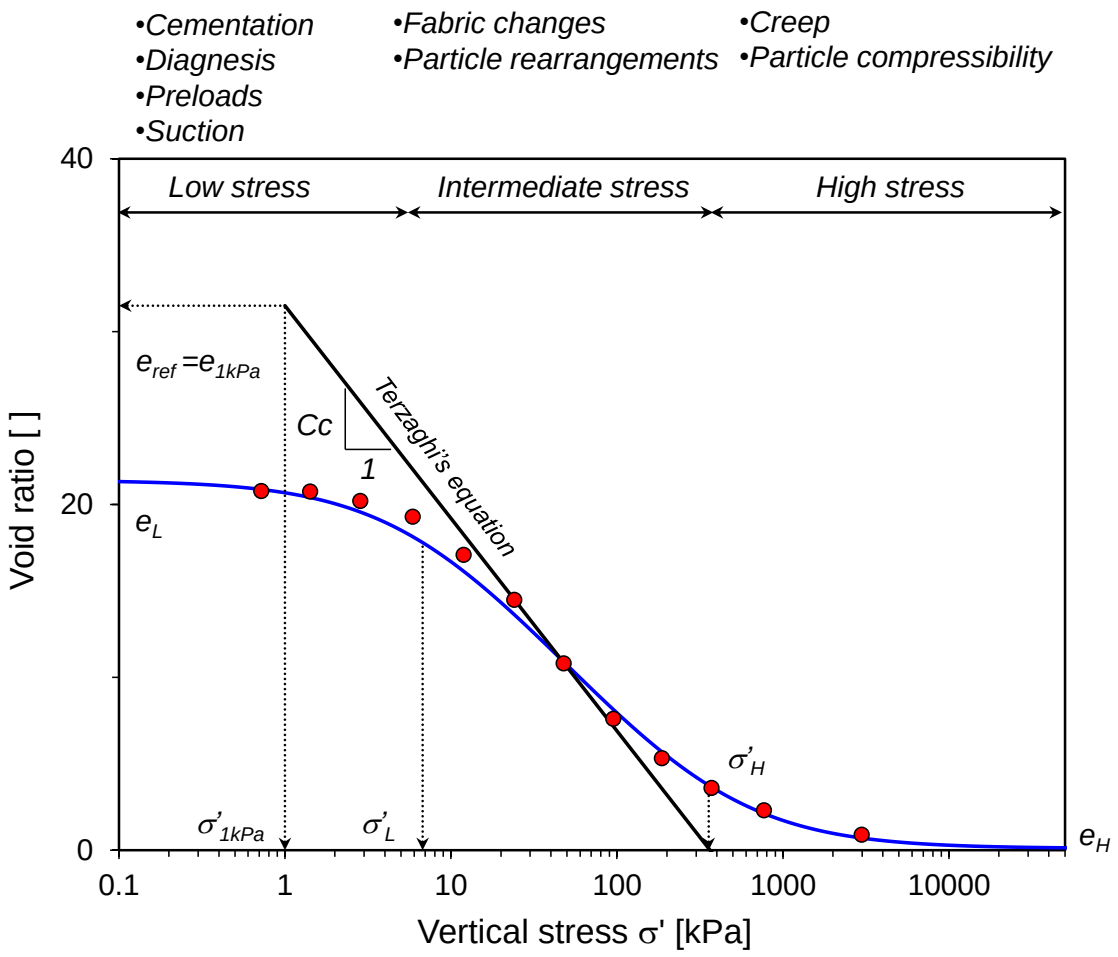

Figure 2.3. Wide stress range 1D compression under zero lateral strain boundary condition. Data are fitted with the double-asymptote model suggested in this study. Sodium montmorillonite at 0.1 N and pH=7. Data source: Mesri and Olson (1971).

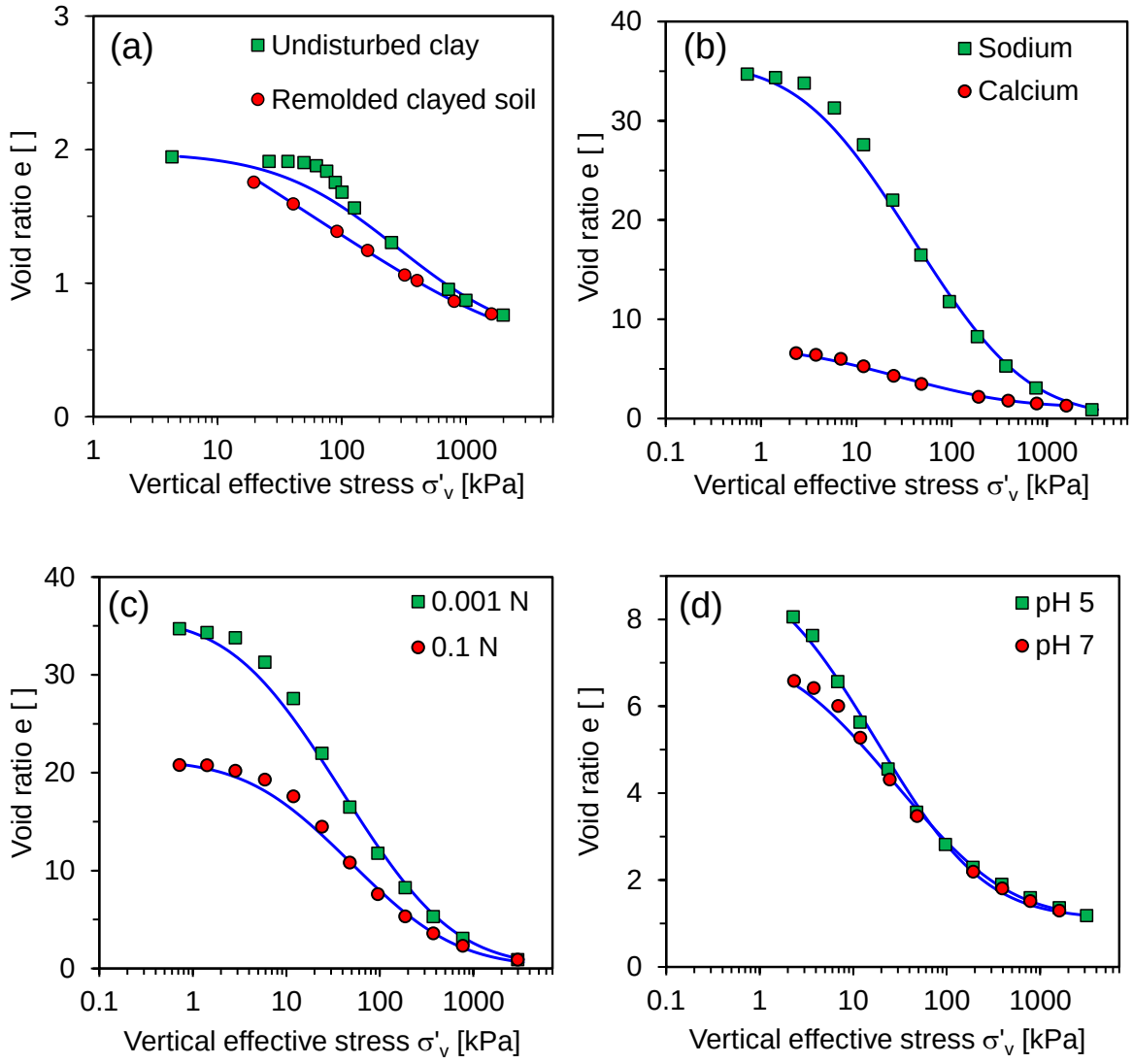

Figure 2.4. The proposed model is tested for natural clays and remolded clays; (a) Bothkennar soil from 6.5 m; (b) Sodium and calcium montmorillonite at 0.001 N and pH=7; (c) Sodium montmorillonite at pH=7; (d) Calcium montmorillonite at 0.001 N $Cacl_2$; Data sources: (a) Burland (1990) and (b)-(d) Mesri and Olson (1971).

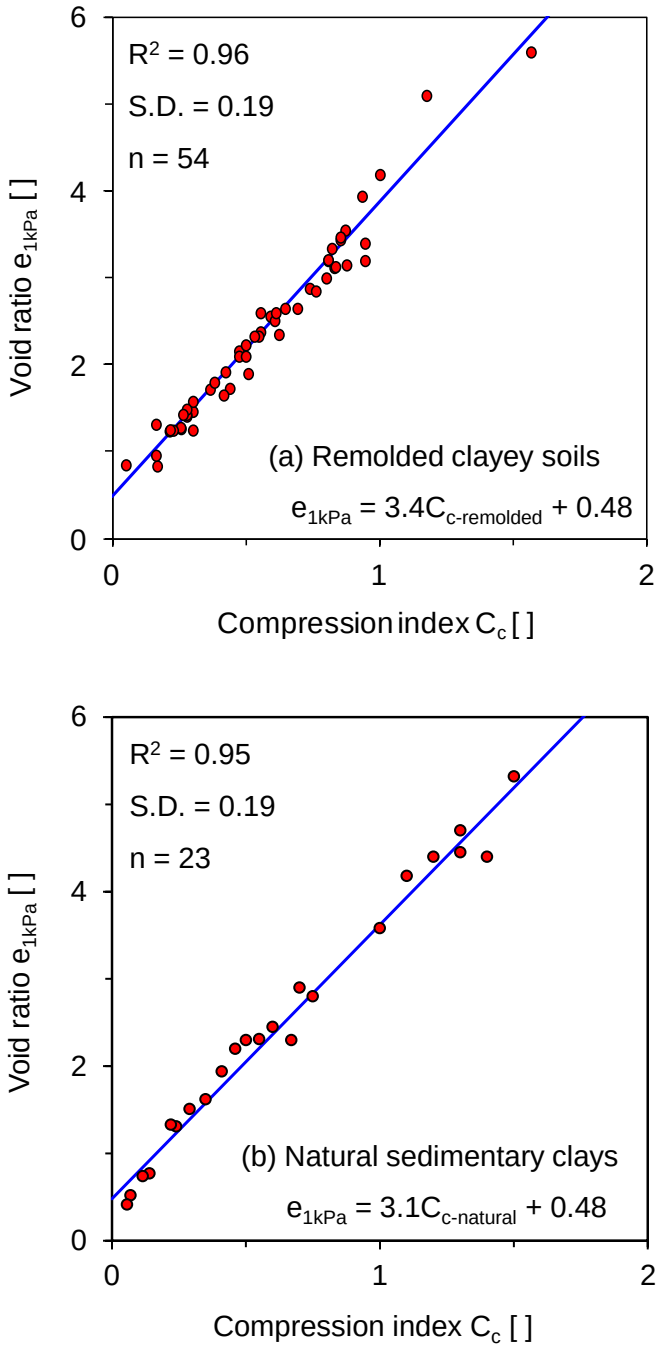

Figure 2.5. Empirical correlations between the e1kPa and C_c based on the published e-log σ' data; (a) Remolded clayey soils; (b) Natural sedimentary clays.

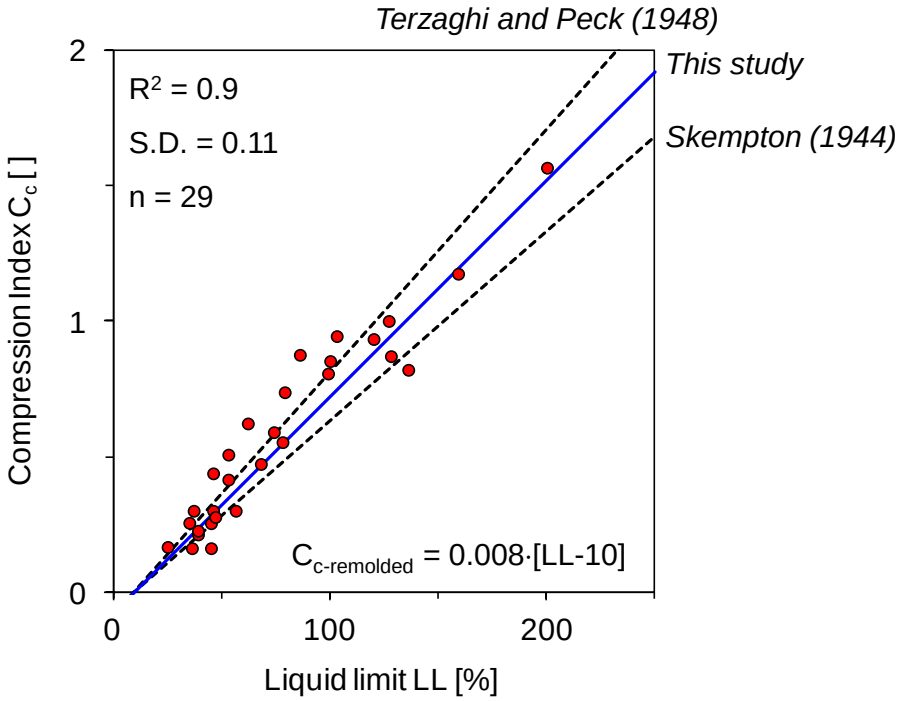

Figure 2.6. Empirical correlation between C_c and LL for remolded clayey soils

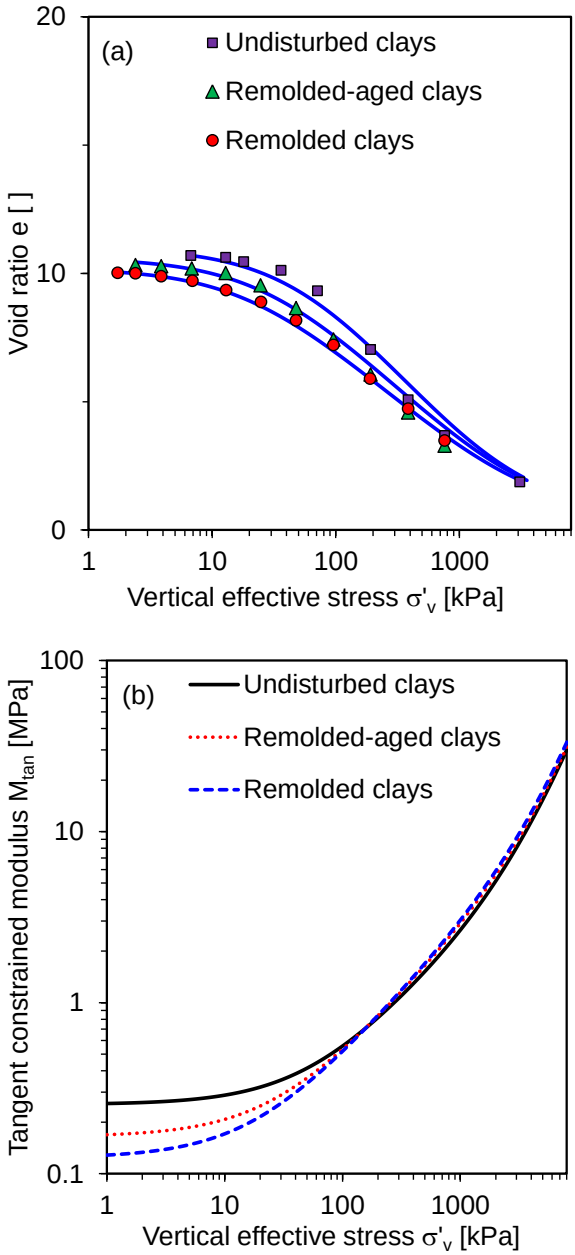

Figure 2.7. Consolidation curves and large-strain stiffness of Mexico City clay: (a) Void ratio vs. Vertical effective stress for Undisturbed, remolded-aged, and remolded clays. The data are fitted with the proposed compressibility model in this study (Data source: Mesri and Olson, 1975); (b) 1D tangential constrained modulus from the derivative of the proposed model.

CHAPTER 3

SMALL AND LARGE STRAIN STIFFNESS

3.1 Introduction

Soil stiffness determines the deformation geo-structures experience. Soil stiffness is measured using laboratory tests (e.g., oedometer and triaxial tests), or in-situ tests (e.g., seismic CPT, pressuremeter, dilatometer, screw plate). The accurate determination of the small-strain stiffness in laboratory device requires local measurements to avoid seating effects (Jardine et al., 1984; Goto et al., 1991) or wave propagation techniques (Thomann and Hryciw, 1990; Santamarina et al., 2001). In addition, these techniques such as resonant columns allow for the assessment of soil stiffness degradation over a wide range of strains (Anderson and Richart, 1976; Vucetic and Dobry, 1991).

Soil stiffness is related to particle-level deformation mechanisms. Low-perturbation shear wave propagation is a constant-fabric phenomenon that causes a strain level below the elastic threshold strain; thereafter, fabric changes take place (Santamarina et al., 2001; Cha et al., 2014). Concurrent measurement techniques permit the measurement of large stress-strain response with simultaneous small-strain measurements (Iwasaki et al., 1978; Viggiani and Atkinson, 1995). The purpose of this study is to discern differences between small and large-strain stiffness in view of engineering applications.

3.2 Stress-strain behavior

The global soil response reflects the integration of particle-to-particle interactions, such as Hertzian and Mindlin-type contact deformation, which render soils inherently nonlinear and nonelastic soils.

Elastic properties

If the wavelength is much greater than the internal scale of the discrete medium (e.g., particle size for soils and joint spacing for joined rock masses), the long wavelength fronts propagate in the medium as in a continuum without experiencing Brillouin dispersion (Santamarina et al., 2001; Cha et al., 2014).

Assuming elasticity, the small strain shear stiffness can be obtained from shear wave velocity measurements. Then, different elastic moduli can be computed, knowing Poisson's ratio, as summarized in Table 3.1. Poisson's ratio $\upsilon=-\varepsilon_{\perp}/\varepsilon_{\parallel}$ relates strains normal $\varepsilon_{\perp}$ and parallel $\varepsilon_{\parallel}$ to the direction of loading. Experimental studies reveal that Poisson's ratio is affected by measurement choices (Figure 3.1.a: local measurement is preferred), strain level, and soil type. The analysis of regular packings of monosized spheres shows that the characteristic skeletal Poisson's ratio is different from the Poisson's ratio of the mineral that makes the particles (Santamarina and Cascante, 1996). Poisson's ratio is υ=0.1 and 0.15 at small strains (Jamiolkowski et al., 1994; Lehane and Cosgrove, 2000 -Figure 3.1.b). For constant volume conditions, Poisson's ratio approaches $\upsilon \rightarrow 0.5$; finally, $\upsilon > 0.5$ reflects soil dilatancy.

Small strain stiffness

The small-strain response takes place at constant fabric, and deformation is localized at contacts. Following Hertzian theory, the small strain stiffness can be expressed as a power function of effective stress (Hardin, 1978; Cascante et al., 1998). Corrections for void ratio can be redundant (Houlsby and Wroth, 1991; Viggiani and Atkinson, 1995; Jovi$\hat{c}$ić and Coop, 1997; Rampello et al., 1997; Cha et al., 2014). In its simplest form, the small strain stiffness depends on the mean stress acting on the plane of shear $\sigma'_m=(\sigma'_1+\sigma'_3)/2$:

$$G_{max} = A\left(\frac{\sigma_1^{'} + \sigma_3^{'}}{2kPa}\right)^{\Omega} \quad (3.1)$$

where the factor A [kPa] and exponent Ω are related to physical and geometrical particle-level soil characteristic (Chang et al., 1991). For simple cubic packing configuration, the factor A is a function of the Poisson's ratio and the shear modulus of the mineral that makes the grains. In a random packing configuration, the two parameters vary with coordination number or void ratio. The exponent Ω captures the shear stiffness sensitivity to the state of stress and ranges from Ω = 1/3 for elastic spherical contacts and Ω = 1/2 for cone-to-plane contacts to greater than Ω > 1.0 for electrical interaction (Santamarina and Cascante, 1996; Cho et al., 2006; Cho et al., 2007; Cha et al., 2014). The exponent accounts for fabric changes during loading.

Large strain stiffness

Fabric changes take place above the elastic threshold strain and define the soil stress-strain response. A number of mathematical models have been proposed to represent the large stress-strain response (Ramberg and Osgood, 1943; Brinch Hansen, 1963; Duncan and Chang, 1970; Fahey and Carter, 1993; Mayne, 1994; Puzrin and Burland, 1996; Puzrin and Burland, 1998; Vardanega and Bolton, 2013). In its simplest form, the global response resembles a hyperbolic trend (Kondner, 1963). Then, the strain γ dependent secant shear stiffness G_{sec} is

$$G_{sec} = \frac{G_{max}}{1 + \frac{\gamma}{\gamma_{ref}}} = \frac{G_{max}}{1 + \frac{\gamma \cdot G_{max}}{\tau_{ult}}} \quad (3.2)$$

where G_{max} is the small strain modulus and τ_{ult} is the ultimate shear strength.

3.3 Results and analyses

Experimental small-strain stiffness and stress-strain data are collected from the literature. Data were gathered under different stress paths, using resonant columns, oedometer tests, and triaxial tests. In all cases, we fit the large strain response with simple models to evaluate the evolution of the tangent modulus along the monotonic stress-strain curve:

$$E_{tan}\Big|_{\varepsilon} = \lim_{\Delta\varepsilon \to 0} \frac{\sigma'(\varepsilon + \Delta\varepsilon) - \sigma'(\varepsilon)}{\Delta\varepsilon} = \frac{d\sigma'}{d\varepsilon}\Big|_{\varepsilon} \qquad (3.3)$$

Stress-strain models and corresponding tangent moduli are tabulated in Table 3.2. Finally, small strain and tangent stiffness are compared in all cases.

Isotropic loading

The isotropic response measured in a resonant-column device shown in Figure 3.2.a is curve-fitted with a Hertzian type power equation (Table 3.2.a; θ=1.25). The fitted model allows for the calculation of the tangent strain stiffness (Table 3.2). Tangent and small-strain measurements compare well in Figure 3.2.a.

k_o loading

A modified oedometric cell was used to measure small-strain shear wave velocity and large strain soil compressibility (Figure 3.2.b - See additional data in Appendix A). The void ratio-stress trend is fitted with the modified Terzaghi model (Table 3.2.b) to compute the tangent stiffness: The measured small-strain stiffness and the computed tangent stiffness increases with the vertical effective stress, however, the small strain stiffness is greater than the tangent modulus at all stress levels (Figure 3.2.b).

Deviatoric loading

Triaxial test data and concurrent small-strain shear stiffness measured with bender elements are compared in Figure 3.2.c. Large strain data are fitted with a hyperbolic trend

(Table 3.2.c). The tangent modulus and the small-strain stiffness are similar within small strains, but the tangent modulus decreases at large strain while the small strain stiffness remains nearly constant.

3.4 Discussion

Small and large strain stiffness susceptible to state of stress

The stress and strain dependent variation in stiffness can be predicted by combining equations (3.1) and (3.2) and assuming Coulomb-type frictional strength. Let's consider two stress conditions as shown in Figure 3.3. By inserting the shear strength $\tau_{ult} = \sigma'_m \cdot \sin\phi'$ into equation (3.2), the secant shear stiffness can be expressed as:

$$G_{sec} = \frac{\sigma'_3 \cdot K \cdot \Lambda \left(\frac{\sigma'_m}{1kPa} \right)^{\Omega}}{\sigma'_3 \cdot K + \gamma \cdot \Lambda \left(\frac{\sigma'_m}{1kPa} \right)^{\Omega}} \tag{3.4}$$

where the maximum stress ratio $K = [\tan^2(45+\varphi/2) - 1]/2$ is determined by the friction angle. Finally, the stiffness ratio at two different mean stress states σ'^{I}_m and σ'^{II}_m becomes:

$$\frac{G^{I}_{sec}}{G^{II}_{sec}} = \left(\frac{\sigma'^{I}_m}{\sigma'^{II}_m} \right)^{\Omega+1} \left[\frac{\sigma'^{II}_3 \cdot K + \gamma \cdot \Lambda \left(\frac{\sigma'^{II}_m}{1kPa} \right)^{\Omega}}{\sigma'^{I}_3 \cdot K + \gamma \cdot \Lambda \left(\frac{\sigma'^{I}_m}{1kPa} \right)^{\Omega}} \right] \tag{3.5}$$

where σ'_m is the mean effective stress (Santamarina et al., 2001). Note that the two extreme conditions are:

$$\frac{G^{I}_{sec}}{G^{II}_{sec}} = \left(\frac{\sigma'^{I}_m}{\sigma'^{II}_m} \right)^{\Omega} \qquad \text{when } \gamma \to 0 \quad \text{small strain stiffness} \tag{3.6a}$$

$$\frac{G^{I}_{sec}}{G^{II}_{sec}} = \frac{\sigma'^{I}_m}{\sigma'^{II}_m} \qquad \text{when } \gamma \to \infty \quad \text{strength-determined} \tag{3.6b}$$

This analysis shows that the effective exponent Ω varies from at $\gamma \rightarrow 0$ to Ω=1 as $\gamma \rightarrow \infty$. These trends were anticipated in Terzaghi and Peck (1948) and are supported by experimental studies (Viggiani and Atkinson, 1995; Jovičić and Coop, 1997).

Small-Strain Stiffness versus Tangent Stiffness

Results in Figure 3.2 highlight fundamental differences between the evolution of the small-strain stiffness and the tangent to large-strain response. In particular, it is important to recognize that:

- Small-strain measurements are an assessment of soil state, i.e., a constant-fabric perturbation
- The tangent stiffness reflects the local rate of soil change with strain during a large strain test.

Differences between these two are highlighted in deviatoric loading tests as shown in Figure 3.2.c.

Oedometric k_o loading

The pronounced differences in the magnitude of stiffness observed in oedometric tests (Figure 3.2.b and Appendix A) can be attributed to inherent experimental difficulties. In particular, seating effects can play a dominant role in small-thickness oedometer specimens (typically ~ 12.7 mm - ASTM D 2435-04). Seating effects have long been recognized in triaxial tests (Jardine et al., 1984; Goto et al., 1991), but remain unresolved in oedometer tests. We can conclude that oedometer tests should be reserved for the study of very soft sediments.

Constitutive models

A preliminary analysis of simple and robust constitutive models frequently used in practice shows that the models fail to capture differences in small and large-strain

stiffness noted above. This observation extends to elasto-plastic Drucker-Prager, hyperbolic, and Cam-Clay type models.

Engineering implications

The use of small strain stiffness is gaining relevance for the prediction of ground deformation, in development of more consistent frameworks for numerical simulation, and in performing back analyses. In fact, the strain field around geo-structures such as foundations, excavations, and tunnels is typically governed by strains that are lower than $\gamma=10^{-1}$% except in the near-field (Jardine et al., 1986; Burland, 1989; Mair, 1993; Mayne et al., 2009). In this strain regime, small-strain stiffness is a good prediction of deformation (Tatsuoka et al., 1997; Atkinson, 2000; Clayton, 2011). Additional biases result from sampling effects (Stokoe and Santamarina, 2000; Dai and Santamarina, 2014).

3.5 Conclusions

The prediction of ground deformation is fully dependent on the stress-and strain-dependent stiffness. Recent design approaches using small strain stiffness tend to show better agreement between predicted and measured settlements than analyses based on conventional lab and field tests. However, concurrent measurements of small and large-strain show pronounced differences that require careful consideration and further developments in constitutive modeling and numerical simulations

Table 3.1. Definition on the elastic modulus and small strain modulus from shear wave velocity.

Parameter	Definition	Small strain modulus from shear wave velocity
Shear modulus	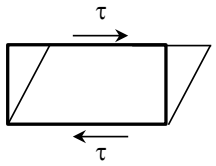 $G = \frac{\tau}{\gamma}$	$G_{max} = Vs^2\rho$
Bulk modulus	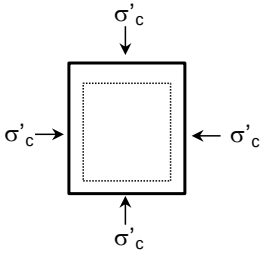 $B = \frac{\sigma'_c}{\varepsilon_{vol}}$	$B_{max} = \frac{2(1+\nu)}{3(1-2\nu)} Vs^2\rho \overset{\nu=0.15}{\approx} 1.1Vs^2\rho$
Young's modulus	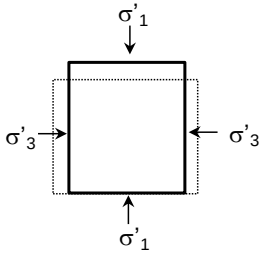 $E = \frac{\sigma'_1 - \sigma'_3}{\varepsilon_1}$	$E_{max} = 2(1+\nu)\cdot Vs^2\rho \overset{\nu=0.15}{\approx} 2.3Vs^2\rho$
Constrain modulus	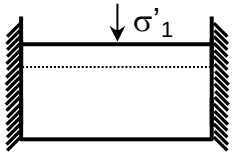 $M = \frac{\sigma'_1}{\varepsilon_1}$	$M_{max} = \frac{2(1-\nu)}{(1-2\nu)} Vs^2\rho \overset{\nu=0.15}{\approx} 2.4Vs^2\rho$

Table 3.2. Stress-strain relations and tangent modulus used in this study

Loading	Stress-strain equations	Tangent modulus	Notes
(a) Isotropic	$\sigma'_c = \chi(\varepsilon_v)^{\theta}$	$B = \chi\theta(\varepsilon_v)^{\theta-1}$	χ: Confinement stress at $\varepsilon_v = 1.0$ θ: Stress dependency related to interparticle contacts and fabric changes during loading
(b) k_o	$e = e_{ref} - C_c \log\left(\frac{1kPa}{\sigma'+\sigma'_L} + \frac{1kPa}{\sigma'_H}\right)^{-1}$	$M = \ln(10)\frac{(1+e)}{C_c}(\sigma'+\sigma'_L)\left(1+\frac{\sigma'+\sigma'_L}{\sigma'_H}\right)$	σ'_L: low stress as $\sigma' \to 0$ σ'_H: High stress $\sigma' \to \infty$ C_c: Compression index e_{ref}: reference void ratio *In this study (Chapter 2)*
(c) Deviatoric	$\sigma'_d = \frac{\varepsilon_z}{a + b\varepsilon_z}$	$E = \frac{a}{(a + b\varepsilon_z)^2}$	$a = \frac{1}{E_{max}}$ and $b = \frac{1}{\tau_{ult}}$ *Kondner (1963)*

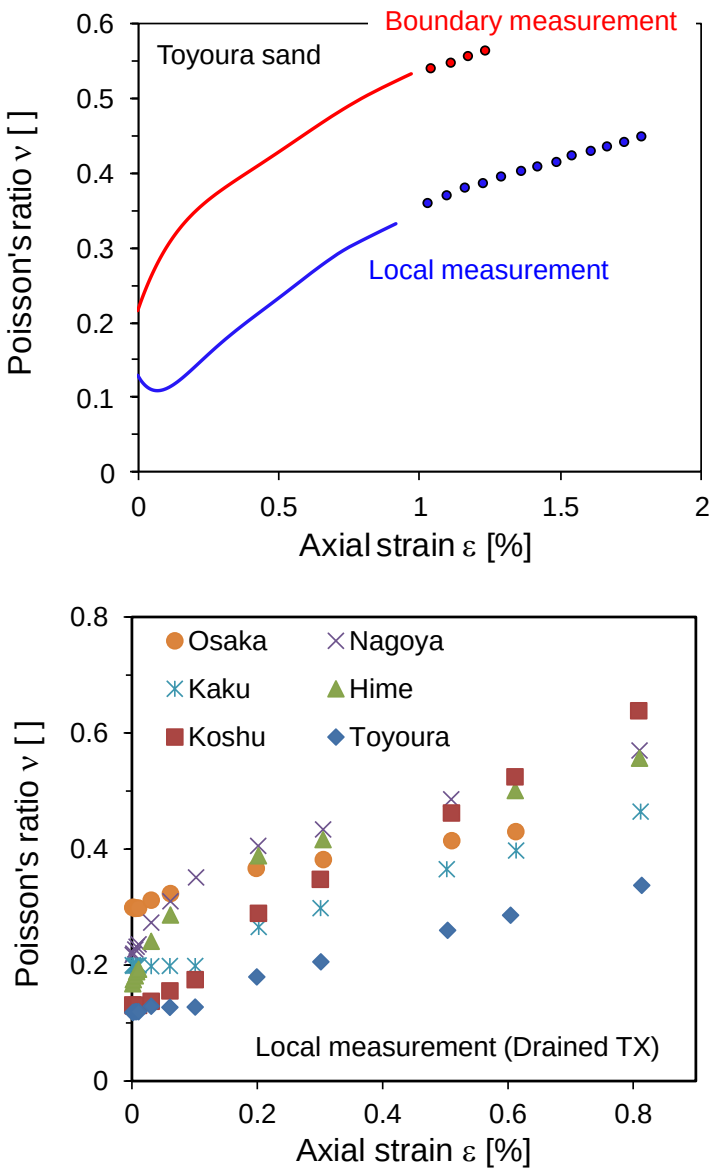

Figure 3.1. Poisson's ratio vs. axial strain; (a) Different measurements; (b) Different sands; Data sources: (a) Jamiolkowski et al. (1994) and (b) Lehance and Cosgrove (2000).

Loading	Stress-strain curve	Stiffness – strain curve	Sediment / Reference
(a) Isotropic loading (Resonont column test)	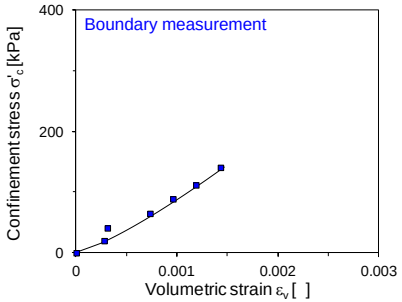	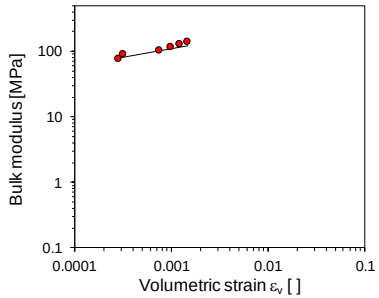	Barco sand / Santamarina and Cascante (1996)
(b) ko loading (with bender elements)	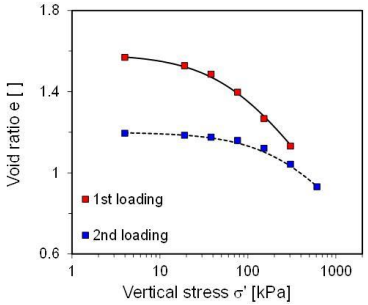	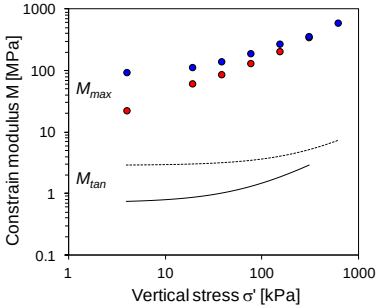	Remolded kaolinite / Fam and Santamarina (1997)
(c) Deviatoric loading (Triaxial test with bender elements)	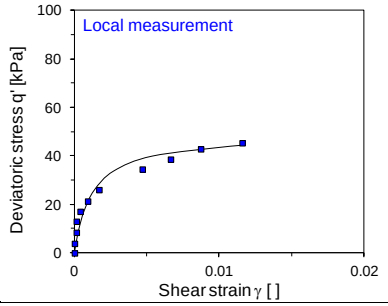	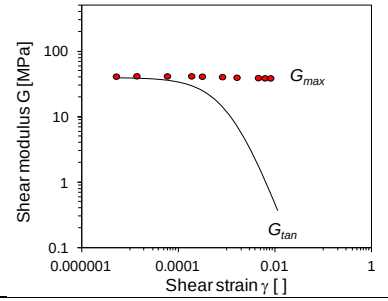	Remolded kaolinite / Viggiani and Atkinson (1995)

Figure 3.2. Strain-dependent soil behavior with different tests; (a) Isotropic loading; (b) Isotropic unloading; (c) Deviatoric loading. The circles represent small strain stiffness from shear wave velocity. Continuous lines are the tangent modulus calculated by fitting stress and shear strain.

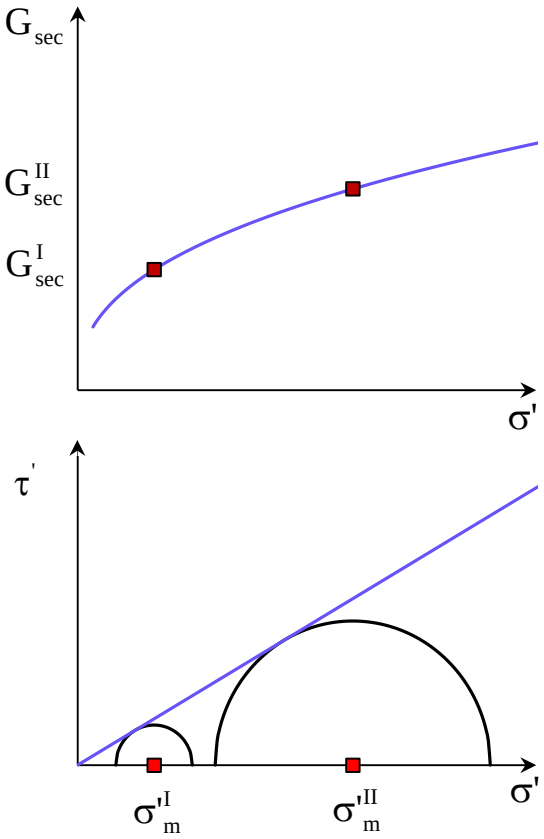

Figure 3.3. Schematic diagram of secant modulus and shear stress with respect to mean effective stress.

	Stress-strain curve	Stiffness – strain curve	Sediment / Reference
(a) Loading steps	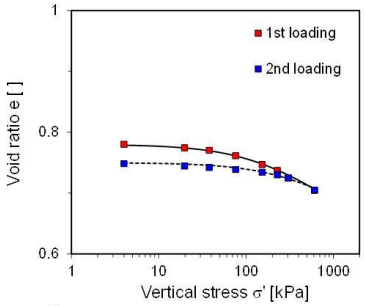	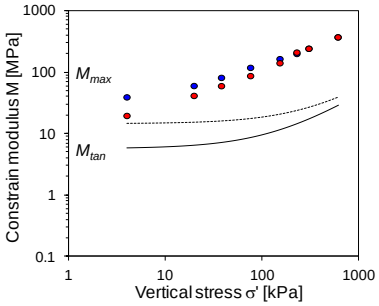	Silica flour / Fam and Santamarina (1997)
(b) Initial packing density	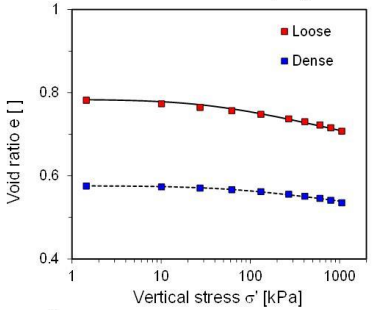	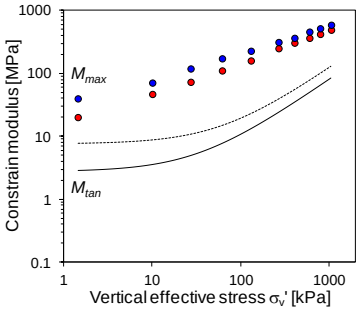	Nevada sand / Yun and Santamarina (2005)
(c) Loading and unloading	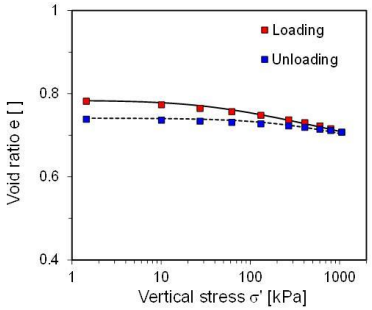	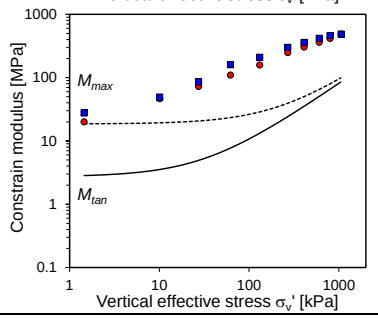	

Appendix to Chapter 3: Strain-dependent soil behavior with Oedometer test: (a) Loading steps; (b) Initial packing density; (c) Loading and unloading. The circles represent small strain stiffness from shear wave velocity. Continuous lines are the tangent modulus calculated by fitting stress and shear strain.

CHAPTER 4

TERMINAL DENSITIES FOR REPETITIVE LOADS

- Zero lateral strain boundary conditions -

4.1 Introduction

Energy is fundamental to preserve and enhance the quality of our life. The massive consumption of fossil fuel creates a stringent demand for new energy sources while also raising serious environmental concerns. Many developed countries have agreed to legally bind to reductions in the emissions of greenhouse gases (Breidenich et al., 1998). As a result, the energy produced from renewable sources and the need for geo-storage is steadily increasing. One of the common characteristics of geo-storage systems is that the surrounding geomaterials experience numerous cycles induced by mechanical processes (Luong, 1980; Sawicki, 1994; Sawicki and Swidzinski, 1995; Wichtmann et al., 2007; Narsilio and Santamarina, 2008; Wichtmann et al., 2010; Wichtmann et al., 2010), thermal processes (Viklander, 1998; Chen et al., 2006), and chemical processes (wetting and drying - Osipov et al., 1987; Pejon and Zuquette, 2002; Tripathy and Subba Rao, 2009). The imposed external forces are characterized by amplitude, frequency, and the cyclic excitation type (Pasten and Santamarina, 2011).

The global response of granular materials to repetitive loads can be divided into elastic deformation and permanent deformation. Accurate prediction of geostructure performance is critically dependent on whether or not soils experience progressive accumulation of plastic deformation.

Soils beneath a wind turbine foundation where the diameter is large compared with the soil depth experience contractive volume change under zero lateral strain

boundary conditions. Soils subjected to k_o-repetitive loads accumulate plastic strain, and can eventually experience considerable displacement: more than 10^7 cycles (a typical offshore wind turbine) may produce an unsafe settlement larger than the structure deformation tolerance even with a relatively small strain amplitude, (Bouckovalas et al., 1984; Yeo et al., 1994; Niemunis et al., 2005; Morgan and Ntambakwa, 2008; Achmus et al., 2009; Ben-Hassine and Griffiths, 2013). Thus, the long-term soil behavior of geotechnical systems subjected to mechanical repetitive loads gives rise to an emergent response that does not take place in monotonic loading usually considered in design.

This study focuses on mechanical load cycles for the design of the energy-related geostructures such as onshore and offshore wind farm foundations. The main purpose of this study is to experimentally investigate the evolution of volumetric strain induced by drained repetitive k_o-loading. Emphasis is placed on identifying soil plastic shakedown and associated terminal density. This study starts with a review of prior studies on granular materials subjected to repetitive loads. The experimental study is presented next followed by an analysis of implications.

4.2 Previous studies

Drained Cyclic Response

Particle-scale simulations have been performed to explore the effect of cyclic loading on interparticle interaction (Alonso-Marroquin and Herrmann, 2004; García-Rojo and Herrmann, 2005). Simulation results show that (1) most of the imposed energy is dissipated within the first few cycles; (2) plastic deformation occurs until particle contacts cease sliding; (3) Eventually, the system reaches a stable state and the net volume change per cycle is zero.

Experimental studies identify a global response similar to that observed in particle-scale simulations (Hendron, 1963; Luong, 1980; Narsilio and Santamarina, 2008).

In particular, cyclic vertical loads under zero-lateral strain conditions cause permanent vertical strain accumulation (Finn and Vaid, 1977; Finn, 1981; Bouckovalas et al., 1984; Sawicki, 1994; Sawicki and Swidzinski, 1995; Wichtmann et al., 2010).

Terminal void ratio

Critical state void ratio reflects the characteristic sediment structure when the soils undergo large monotonic shear deformation at constant volume, constant shear, and normal effective stress (Schofield and Wroth, 1968). Other examples are the minimum and maximum void ratios prescribed by the standard methods (e_{min} - ASTM 4253; e_{max} - ASTM 4254). In general, there is a characteristic terminal void ratio for each process dependency (Narsilio and Santamarina, 2008).

Strain accumulation functions

Strain accumulation functions are defined to predict the permanent deformation or excess pore water pressure when a sediment is subjected to a large number of cyclic loads. These functions depend on strain amplitude, cyclic preloading, average mean pressure, stress obliquity, and void ratio (Niemunis et al., 2005; Wichtmann et al., 2010). Pasten et al. (2014) propose simple but robust empirical functions that depend on the plastic strain during the first load cycle, the stress obliquity and amplitude, and the number of load cycles. Strain accumulation functions are summarized in Table 4.1.

Shakedown and ratcheting

The response of a soil mass subjected to cyclic loading can converge to shakedown or ratcheting (Figure 4.1 - Koiter, 1960; Sawczuk, 1974; Sharp and Booker, 1984; García-Rojo and Herrmann, 2005). When cyclic loads cause a strain level below the elastic threshold strain, the soil mass recovers the original state upon unloading, and the dissipated energy per cycle remains constant thereafter (elastic shakedown). When the

strain level exceeds the elastic threshold strain, the soil undergoes particle rearrangement and fabric changes; the dissipated energy decreases towards an asymptotic value until the soil reaches a stable deformation state, there is no additional accumulation of deformation and the energy dissipation per cycle becomes constant (plastic shakedown). Ratcheting occurs when deformations continue accumulating at a constant rate as the number of cycles increases $N \rightarrow \infty$.

Cyclic strain flow rule

The cyclic strain flow rule can be expressed as the ratio of the shear strain to the volumetric strain, and characterized with the stress obliquity and the stress state prior to cyclic loading (preloading). Experimental studies reveal that the sequence of deviatoric stress amplitudes and hydrostatic preloading (up to p' = 300 kPa) have a minor effect on the change in the flow direction (Wichtmann et al., 2010). However, preloading up to the failure line produces more shear strain than volumetric strain (Chang and Whitman, 1988). Stress obliquity defines the direction of plastic accumulation (Niemunis et al., 2005). The plastic strain in the first load cycle represents the volumetric and shear strain accumulation defined by the plastic potential function in plasticity theory. As the number of cycles increases, soils evolve towards the terminal density and mostly accumulate shear strain (Pasten et al., 2014).

4.3 Experimental study

Experiments are performed by cycling the vertical load while the specimen is maintained under zero lateral strain boundary conditions. Tests involve different particle shapes, initial packing densities, static load magnitude, and monotonic loads. The vertical repetitive stress amplitude is kept constant in all cases ($\Delta\sigma'_{v\text{-repetitive}}$ = 100 kPa). Sample preparation, devices, and procedures are described next.

Selected Sands - Sample Preparation

Three different sands are used to evaluate 1D soil behavior under repetitive loading: blasting sand, ottawa F110, and ottawa 50–70. Microphotographs in Figure 4.2 show clear differences in particle shape; properties are summarized in Table 4.2. Dense specimens are prepared by alternately pouring and tamping with successive soil layers. Loose specimens are formed using the funneling method.

Test Devices

The oedometer cell consists of a steel ring cell (I.D.=72 mm and O.D.=83 mm). The cell is mounted on the loading frame. Emphasis is placed on minimizing noise/vibration during installation and testing. The vertical displacement is continuously recorded using the LVDT mounted on the top cap.

System compliance. True soil strain measurement can be hindered by the compliances of the loading system and load measuring system (Jardine et al., 1984; Jamiolkowski et al., 1994). System compliance adds measurement errors and obstructs the understanding of soil behavior when the system deformation approaches the true soil deformation. System compliance in the oedometer system involves compression of porous stones and preferential compression at the soil-platen interfaces. System compliance is carefully quantified by using a steel dummy. The response during each loading and unloading cycle is shown in Figure 4.3; the corresponding amplitude is subtracted from soil data to accurately estimate the soil volumetric response.

Test Procedure

Parallel monotonic and two repetitive loading tests are conducted to augment data interpretation. Monotonic tests consist of small effective stress increments $\Delta\sigma'_z \approx 10$ kPa. Repetitive load tests are conducted in three steps. First, static loads are applied using the

same procedure as in monotonic test (until the target load is reached, either 100 kPa or 1 MPa). Then, 20sec loading cycles are imposed. Finally, more monotonic load is added to compare the load-deformation sediment response with the monotonic test data.

4.4 Results and Analyses

Figure 4.4 shows the void ratio evolution against the number of cycles for different static loads and initial packing densities. Most of the volumetric change occurs during the early cycles. The change in void ratio per cycle is nonlinear, and it gradually decreases with the number of loading cycles. Void ratio changes are more pronounced in loose sands and at low static load. Thus, higher static load and denser initial packing experience the fastest rate of densification.

Figure 4.5 presents monotonic load and two repetitive loads. Monotonic deformation data superimpose on repetitive loading data. In all cases, changes in void ratio occur between the two extreme void ratios (e_{max} and e_{min}). For the three different sands, the initial packing density characterizes the compression line obtained from the monotonic load test. Upon subsequent monotonic loading, the effects of cyclic strain accumulation are erased, and void ratio trends converge at high stress. It appears that the terminal void ratio is independent of the initial formation density or void ratio, and it may eventually reach the ko-limiting compression curve (Pestana and Whittle, 1995).

A simple mathematical model is proposed to predict the void ratio e_i after the ith cycle from the void ratio e_1 at the first cycle:

$$e_i = e_1 - (e_1 - e_T)\cdot\left[1 - e^{-\alpha(\log i)^{\beta}}\right] \text{ for } i \geq 1 \quad \text{where, } \alpha = \ln\left(\frac{e_1 - e_T}{e_{10} - e_T}\right) \qquad (4.1)$$

where e_T is the terminal void ratio, α is the inverse of the volumetric strain at the 10^{th} cycle, and β controls the rate of volume change after 10 cycles. Both exponents define the rate of convergence toward the terminal void ratio. This model is driven to have a

small number of physically meaningful parameters (Ockham's criterion). The void ratio trends are fitted with the proposed model. The fitted parameters are tabulated in Table 4.3. Figure 4.6 shows that the terminal void ratio e_T is greater than the minimum void ratio e_{min} in all sands. In other words, repetitive k_o-loading leads to a different terminal void ratio e_T than energetic vibration involved in the measurement of e_{min}.

Empirical correlations are established in terms of change in relative density to the terminal void ratio $\Delta D_T = (e_1 - e_T) / (e_{max} - e_{min})$ and the initial relative density $D_{i=1} = (e_{max} - e_1) / (e_{max} - e_{min})$. As shown in Figure 4.7, the densification controlling parameters α and β in equation 4.1 show strong correlation with ΔD_T and $D_{i=1}$.

4.5 Discussion

Soil Plastic Shakedown

The plastic strain in a given load cycle *i* can be computed as $\varepsilon_i = (e_i - e_{i+1})/(1+e_i)$; replacing equation 4.1

$$\varepsilon_i = \frac{\left(e_1 - e_T\right)\cdot\left[e^{-\alpha(\log i)^{\beta}} - e^{-\alpha(\log i+1)^{\beta}}\right]}{1+e_1-\left(e_1-e_T\right)\cdot\left[1-e^{-\alpha(\log i)^{\beta}}\right]} \qquad (4.2)$$

The soil accumulates plastic volumetric strain when the corresponding strain level is above the elastic threshold strain so that slippage friction takes place between particles. Soil plastic shakedown is observed within the first 100 cycles for some specimen shown in Figure 4.8. Soils with a higher static load and a denser initial state quickly settle into a plastic shakedown state and experience smaller volumetric strains as $i \rightarrow \infty$. The soil mineralogy has a pronounced effect on the convergence towards terminal volumetric state. As the process approaches the plastic shakedown condition, the net volume change per cycle becomes zero, and the sediment reaches terminal density.

1D Constrained Modulus

The stiffness is expected to increases during the loading-unloading-reloading processes. Figure 4.9-a shows that the first loading cycle produces the highest plastic deformation Δe_1. The soil compressibility computed for each unloading cycle (Figure 4.9-b) suggests that the 1D constrained modulus increases with the number of events. Soil stiffening may result from increased contact area and/or coordination number (Cascante and Santamarina, 1996).

4.6 Conclusions

Long-term soil behavior gains relevance in the design of energy-related geostructures. The zero lateral strain condition prevails in many cases, such as in wind turbine foundations. An experimental study was performed to investigate the response of sands under repetitive k_o-loading. Results show

- k_o-repetitive loads produce cumulative plastic volumetric strain, particularly, during the early cycles, the rate of accumulation decreases with the number of events, and stiffness increases.
- Dense sands subjected to high static load quickly settle into a plastic shakedown state, after a relatively low plastic volumetric strain. The soil mineralogy affects convergence toward the terminal volumetric state.
- A simple three-parameter model is proposed to capture the evolution in volumetric strain induced by repetitive k_o-loads. Fitted parameters show strong relations with the initial relative density. The terminal void ratio is greater than the minimum void ratio when the terminal void ratio in all tests conducted as part of this study.

Table 4.1. Summary of strain accumulation functions

	Model parameters	Function	Reference
Strain amplitude	ε_{ref} (1)	$f_{amplitude} = \left(\frac{\varepsilon^{amplitude}}{\varepsilon_{ref}} \right)^2$	Niemunis et al., 2005; Wichtmann et al., 2010b
Cyclic preloading	C_{N1}, C_{N2}, C_{N3} (3)	$f_N = \frac{C_{N1} \cdot C_{N2}}{1 + C_{N2} N} + C_{N1} \cdot C_{N3}$	
Average mean stress	C_p, p_{ref} (2)	$f_p = \exp\left[-C_p \left(\frac{p^{av}}{p_{ref}} - 1 \right) \right]$	
Stress obliquity	C_Y (1) Note: $Y^{av} = f(\eta, \phi_{cs})$	$f_Y = \exp\left(C_Y Y^{av} \right)$	
Void ratio	C_Y, e_{ref} (2)	$f_e = \frac{\left(C_e - e \right)^2}{1 + e} \cdot \frac{1 + e_{ref}}{\left(C_e - e_{ref} \right)^2}$	
Polarization of cycles	$C\pi 1$, $C\pi 1$	$f_\pi = 1 + C_{\pi 1} \left[1 - \cos\left(C_{\pi 2} \varepsilon^{amplitude^2} \right) \right]$	
		$\Delta\varepsilon^{acc} = f_{amplitude} f_N f_p f_Y f_e f_\pi$	
Cumulative volumetric strain	a1, a2 (2)	$\varepsilon_v^{acc}\Big\|_N = \varepsilon_v^{acc}\Big\|_{N=1} \cdot \left[1 + \left[a_1 \left(M - \eta \right)^2 + a_2 \right] \cdot \ln\left(N \right) \right]$	Pasten et al. (2014)
Cumulative shear strain	b1, b2,c1 (3)	$\varepsilon_q^{acc}\Big\|_N = \varepsilon_q^{acc}\Big\|_{N=1} \cdot \left[1 - \left(b_1 \eta - b_2 \right) \cdot \ln\left(N \right) + c_1 \eta \cdot \left(N - 1 \right) \right]$	
		$\Delta\varepsilon^{acc} = \frac{1}{3} \Delta\varepsilon_v^{acc} \cdot 1 + \frac{3}{2} \frac{\Delta\varepsilon_q^{acc}}{q_N} \left(\sigma'_N - p'_N \cdot 1 \right)$	

Table 4.2. Materials used in this study

Note: R = roundness, S = sphericity, and ρ = regularity = (R+S)/2.

		Particle Shape			Packing	
	Gs	R	S	ρ	e_{max}	e_{min}
Blasting	2.65	0.50	0.50	0.50	1.03	0.70
Ottawa F110	2.65	0.70	0.70	0.70	0.95	0.56
Ottawa 50-70	2.65	0.90	0.70	0.80	0.86	0.55

Table 4.3. Model parameters extracted from the proposed model.

	σ'_v [kPa]	Initial density	e_T	α	β
Blasting sand	100	Loose	0.897	0.555	1.70
		Dense	0.745	0.281	1.150
	1000	Loose	0.881	0.458	2.40
		Dense	0.742	0.325	1.0
Ottawa F110	100	Loose	0.768	0.182	2.20
		Dense	0.656	0.130	1.350
	1000	Loose	0.748	0.486	1.70
		Dense	0.636	0.204	1.250
Ottawa 50-70	100	Loose	0.727	0.376	1.80
		Dense	0.625	0.203	1.20
	1000	Loose	0.716	1.407	1.70
		Dense	0.618	0.665	1.10

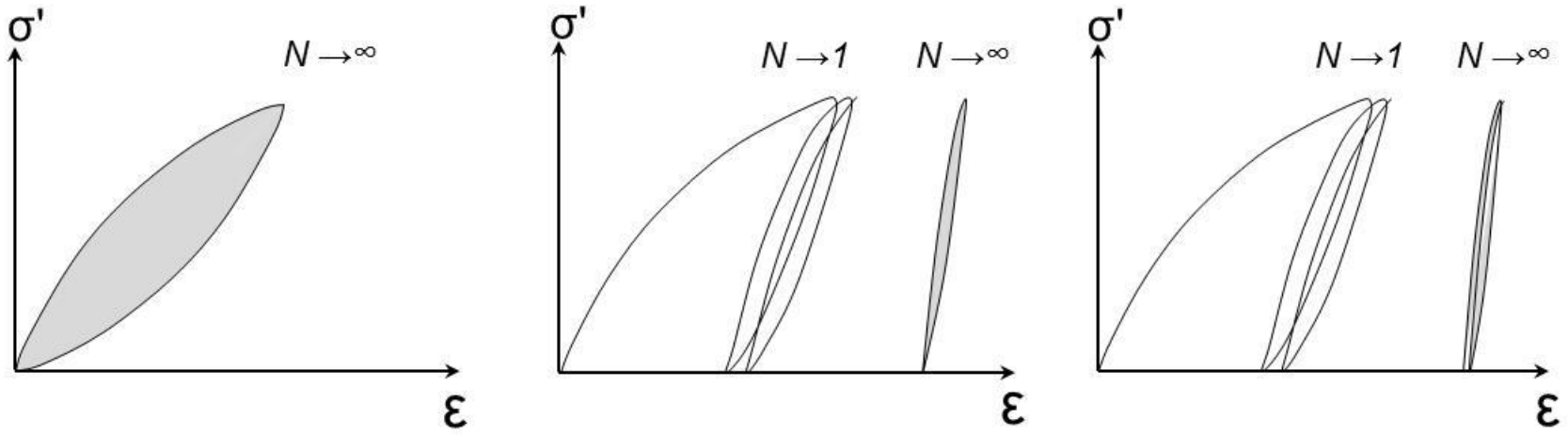

Elastic shakedown	Plastic shakedown	Ratcheting
Below elastic threshold strain	Above elastic threshold strain	
Elastic response	Stabilized and closed cycle of plastic strain ($\delta\varepsilon^p = 0$)	A continuous accumulation of plastic strain ($\delta\varepsilon^p \neq 0$)

Figure 4.1. Long-term soil behavior subjected to drained repetitive loads. The elastic and plastic strains are clearly identified. The energy dissipated in each cycle is the area enclosed by the loading and unloading curves.

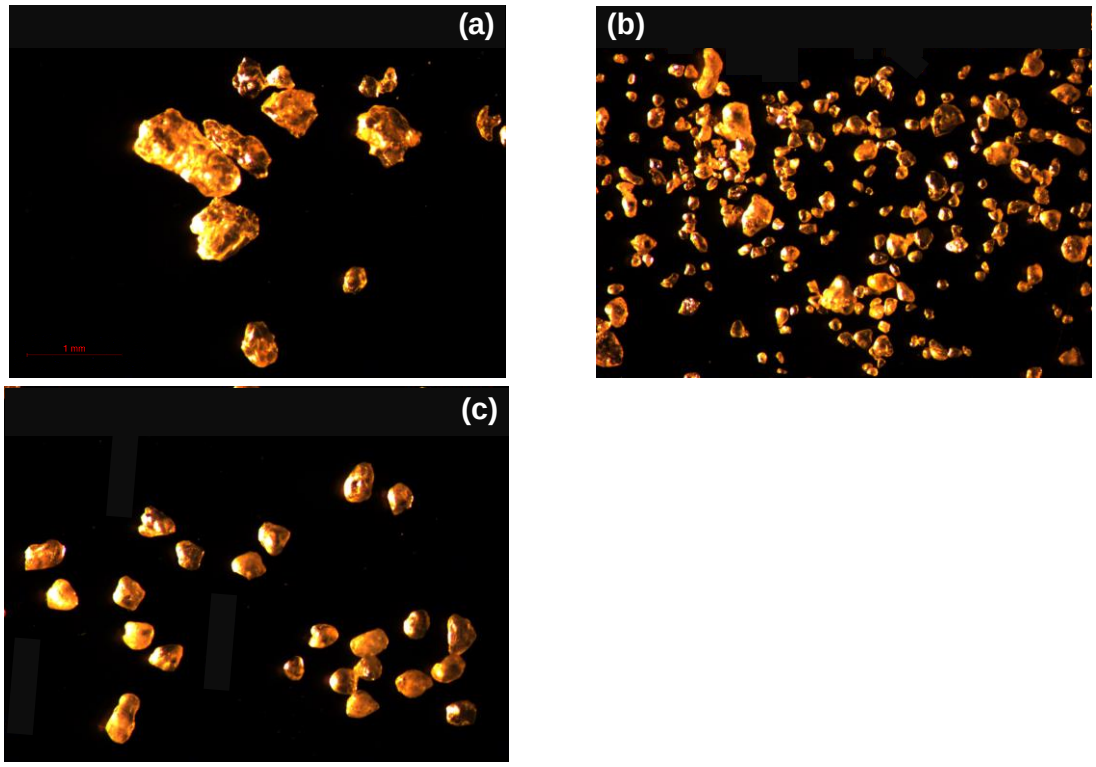

Figure 4.2. Microphotographs on various particle shapes used in this study: (a) Blasting sand; (b) Ottawa F110; (c) Ottawa 50–70.

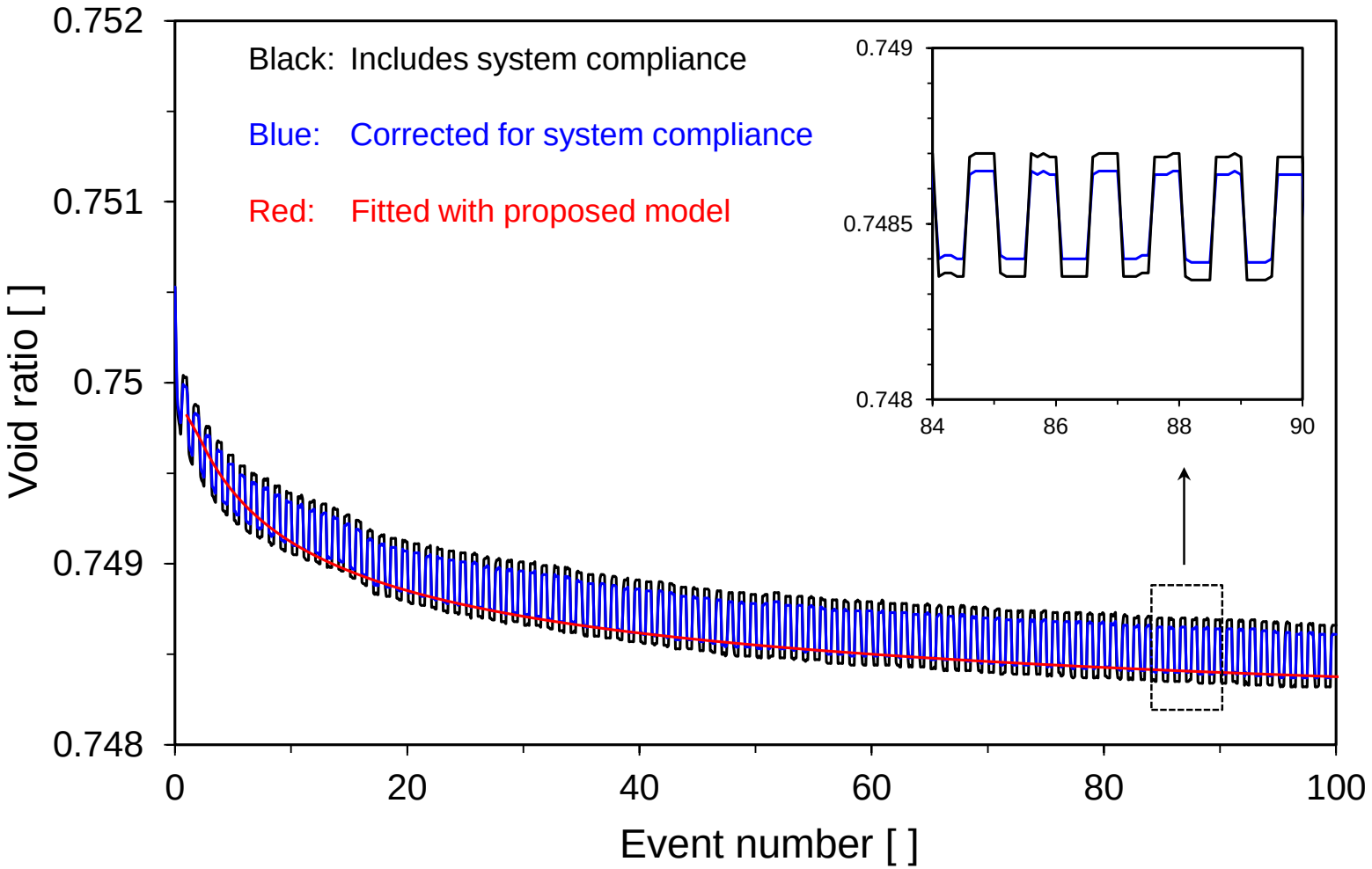

Figure 4.3. The effect of system compliance on void ratio for repetitive ko–loads (σ'_v = 1MPa, $\Delta\sigma'_v$ = 100 kPa, Ottawa F110 sand loose); the trend is computed with equation 4.1.

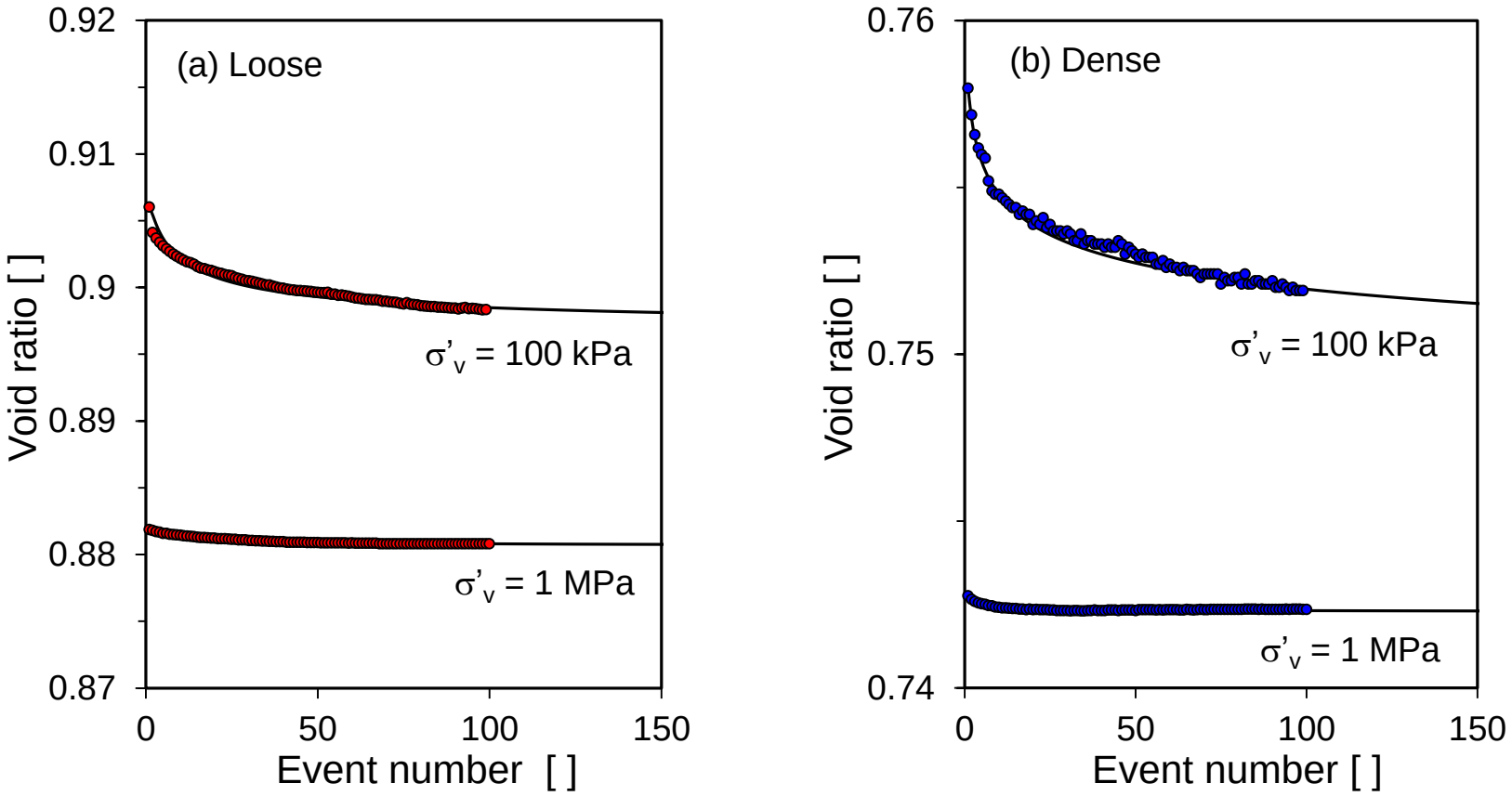

Figure 4.4. The effect of static load magnitude and initial packing density on the void ratio change of blasting sand – (a) Loose and (b) Dense.

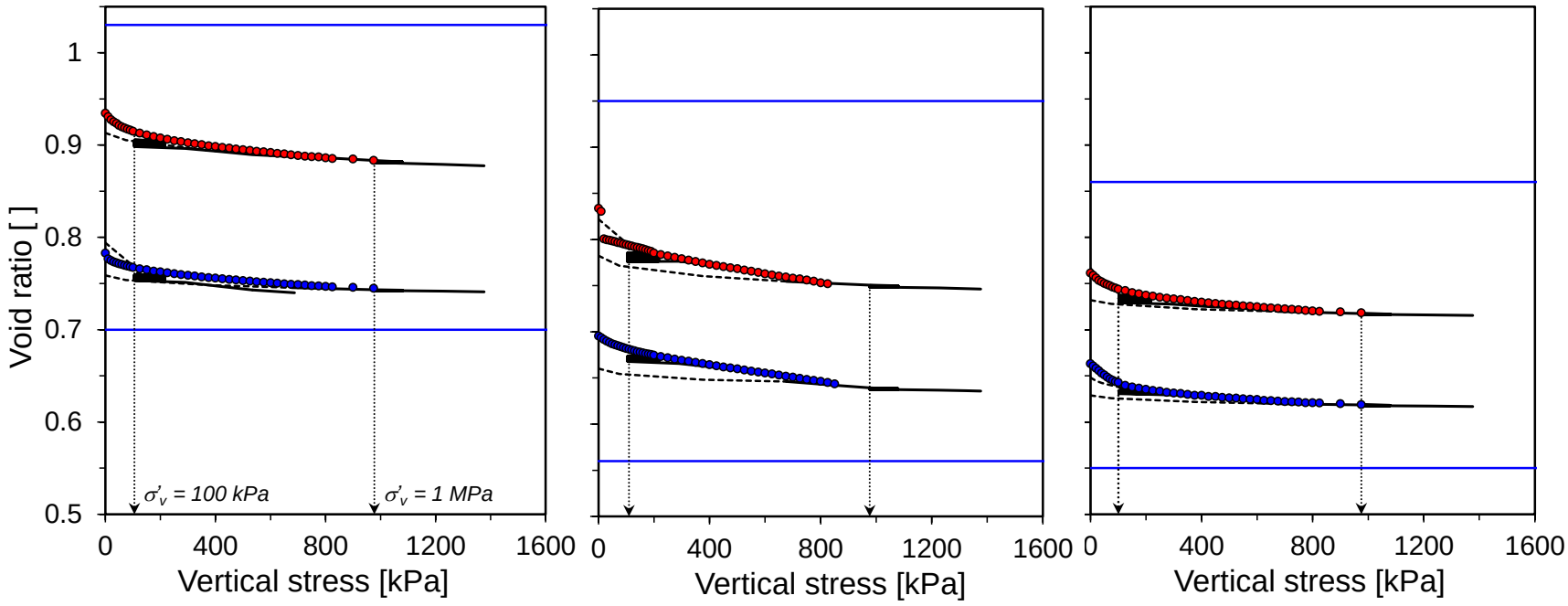

(a) Blasting sand

(b) Ottawa F110 sand

(c) Ottawa 50-70 sand

Figure 4.5. Comparisons of the evolution in the void ratio with different initial densities; comparative tests are performed with the monotonic and repetitive loads. The two extreme lines indicate the e_{max} and e_{min}.

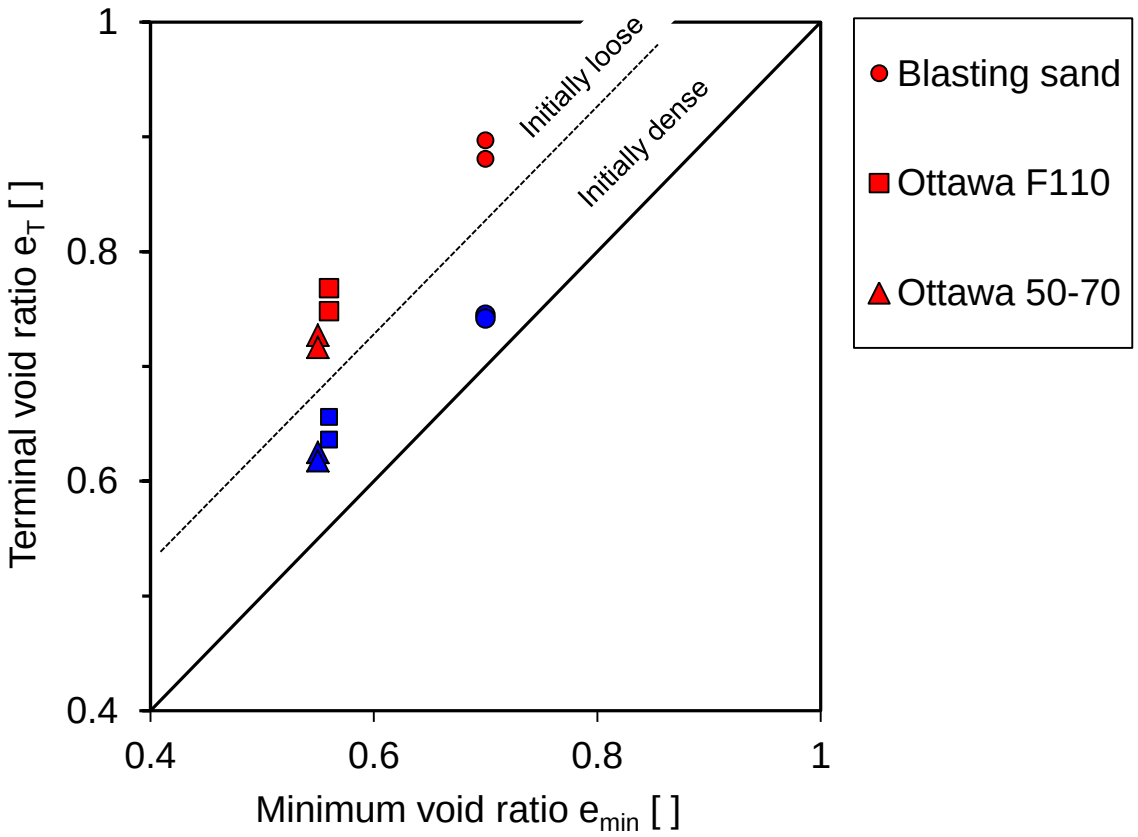

Figure 4.6. Soil characteristic void ratio relations (note that the terminal void ratio is obtained from low and constant amplitude stress).

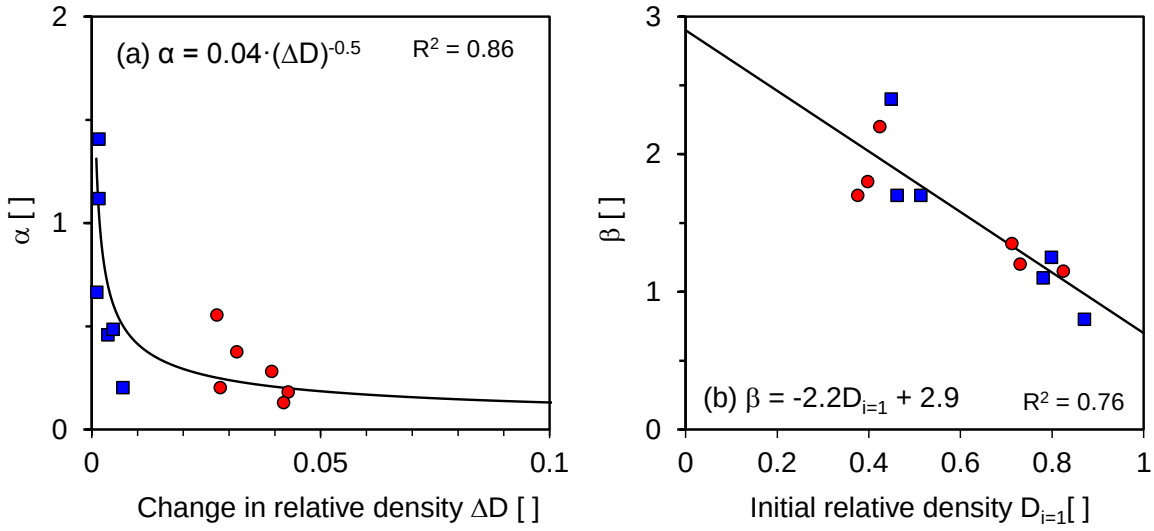

Definition	Equations
Initial relative density $D_{i=1}$ [ ]	$D_{i=1} = \frac{e_{max} - e_1}{e_{max} - e_{min}}$
Change in relative density ΔD [ ]	$\Delta D = \frac{e_1 - e_T}{e_{max} - e_{min}}$
Inverse volumetric strain at 10th cycle α [ ]	$\alpha = \ln\left(\frac{e_1 - e_T}{e_{10} - e_T}\right)$

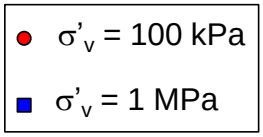

Figure 4.7. Empirical relations extracted from the proposed model; (a) α and ΔD; (b) β and $D_{i=1}$.

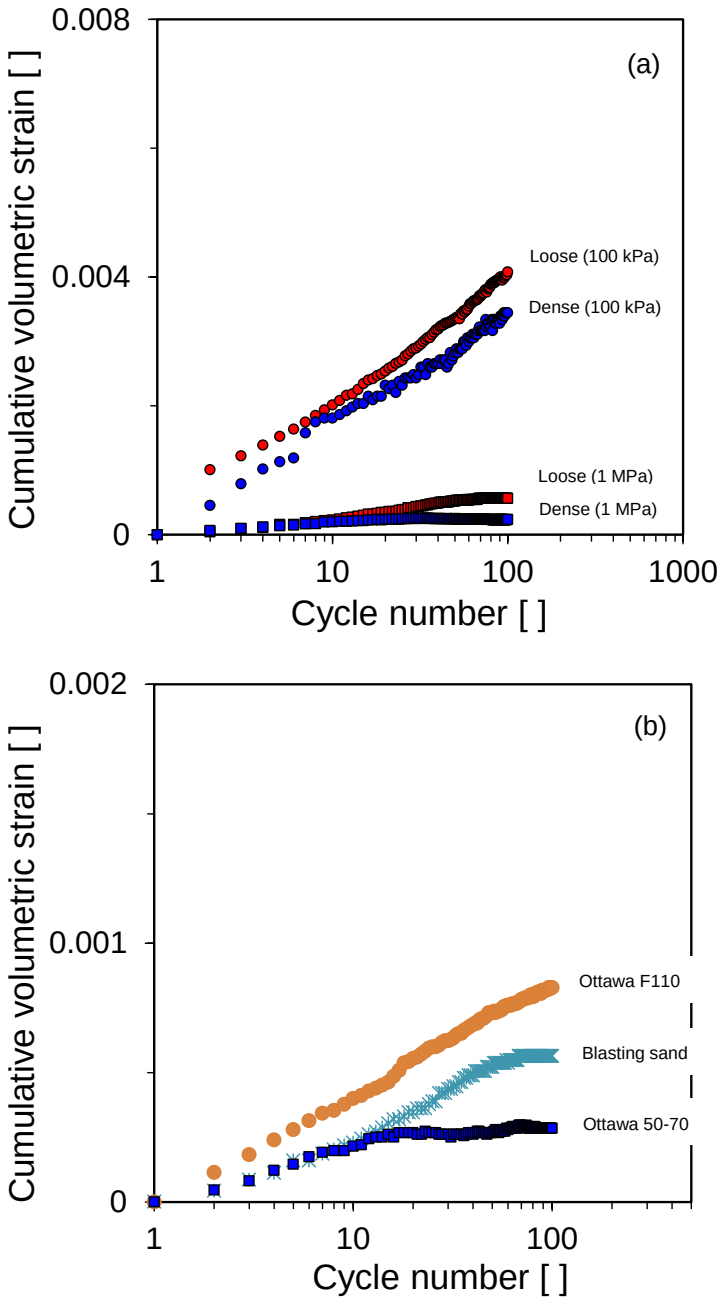

Figure 4.8. Investigation of soil plastic shakedown response. Cumulative volumetric strain vs. cycle number for: (a) Blasting sand, (b) Loose (σ'_v = 1MPa).

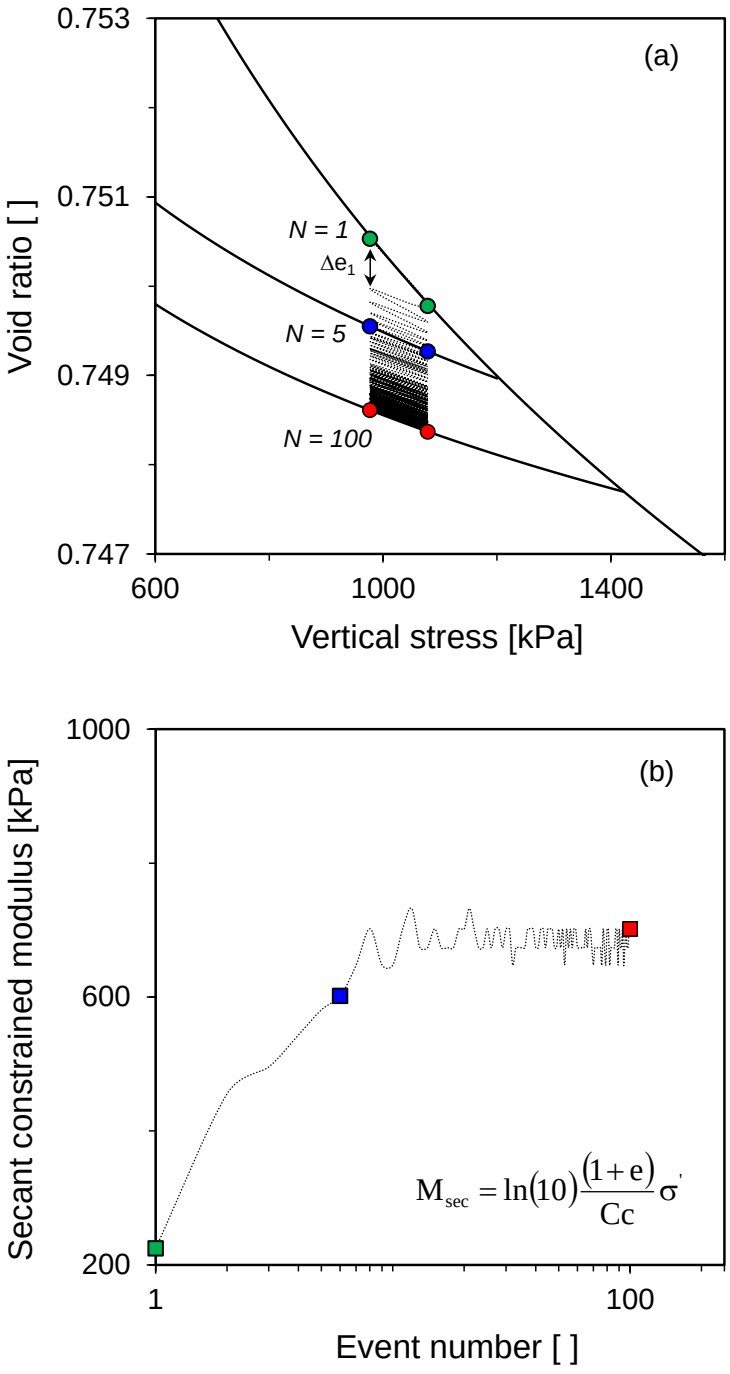

Figure 4.9. 1D soil compressibility behavior for loose F110 sand; (a) Void ratio vs. vertical effective stress; (b) Secant constrained modulus at each load vs. event number.

CHAPTER 5

SETTLEMENT DUE TO SOFT ZONES

5.1 Introduction

Strains and displacement fields are induced by localized mass loss within sediments. Various semi-empirical solutions have been proposed to predict surface settlement and subsurface deformation. However, the complexity of subsurface geological conditions often requires more complex analyses and numerical simulations so that governing parameters can be properly captured to obtain credible results.

This chapter reviews previous studies and presents the stress relaxation module developed within the finite element program ABAQUS. A comprehensive parametric study is performed to explore the effect of various parameters on different subsurface conditions (soft zone depth z_0, number of nearby soft zones, constant volume shear friction angle ϕ_{cs}, preconsolidation, and internal stress reduction). The extensive dataset generated from the numerical study is captured in a summary of simple trends that can be readily used for engineering applications.

5.2 Previous Studies

Closed-form solutions assume perfect plasticity to predict collapse (kinematically and statically admissible conditions - Atkinson and Potts 1977b), and elasticity to estimate stress fields (Kirsch, 1898; Terzaghi and Richart, 1952; Fares, 1987; Verruijt and Booker, 1996; Bobet, 2001). Numerical simulations have explored a wider range of conditions (Mair et al., 1981; Rodrıguez-Roa, 2000; Rodrıguez-Roa, 2002; Franzius and Potts, 2005; Chen et al., 2012). In particular, simulations show that ground movement is significantly affected by stress anisotropy (Guedes and Santos Pereira, 2000). Small scale

(Atkinson et al., 1975; Atkinson and Potts, 1977a; Ahmed and Iskander, 2011) centrifuge model tests (Atkinson and Potts, 1977b; Mair et al., 1981; Jacobsz et al., 2004; Marshall et al., 2012), and field studies have provided extensive surface and subsurface settlement profiles associated to mining and tunneling operations (Peck, 1969; Schmidt, 1969; Clough and Schmidt, 1981; O' Reilly and New, 1982; Mair et al., 1993; Mair, 2008). Displacement fields are regular-smooth in homogeneous media and can be expressed using a few characteristic parameters, as described next.

Surface Settlement. Settlement profiles with limited ground distortions are well matched by the Gaussian function, in terms of two degrees of freedom: the maximum settlement over the centerline S_{max} and the transverse distance from the centerline to the inflection point x_{infl} (Peck, 1969; Schmidt, 1969; Clough and Schmidt, 1981; Cording, 1991). Modifications to the Gaussian trend (Jacobsz et al., 2004) and other published functions with higher degrees of freedom (Celestino et al., 2000; Vorster et al., 2005) are summarized in Table 5.1.

Maximum Settlement S_{max}. The maximum settlement S_{max} is related to the mass loss, its depth and geometry, and the contractive-or-dilative tendency of the soil. Assuming neither dilation nor contraction, the value S_{max} can be obtained from the volume loss V_L and the distance to the inflection point x_{infl} by integrating the Gaussian settlement profile

$$S_{max} = \frac{V_L}{\sqrt{2\pi}\, x_{infl}} \tag{5.1}$$

Distance to Inflection Point x_{infl}. Published statistical regressions based on field data proved estimates of the distance from the centerline to the inflection point x_{infl} (Table 5.2 - Peck, 1969; Schmidt, 1969; Atkinson and Potts, 1977a; Clough and Schmidt, 1981;

Mair et al., 1981; O' Reilly and New, 1982; Mair et al., 1993; Moh et al., 1996). Equations relate the value x_{infl} to the soft zone depth z_0, and size R.

Subsurface Displacements. Subsurface displacements follow a Gaussian function as well. The distance to subsurface inflection points x_{infl} at depth z can be estimated with equations summarized in Table 5.2 (Mair et al., 1993; Moh et al., 1996).

5.3 Numerical simulation: Two dimensional - Code verification

Dissolution pipes are inherently long. Therefore, numerical simulations can be reduced to 2D configurations.

Soft zone formation simulation. The stress relaxation module developed in ABAQUS for this study is based on the internal stress reduction method. The numerical procedure is as follows:

1. The soft zone geometry is pre-defined.
2. The initial internal stress inside the soft zone is equivalent to the value of geostatic k_0-stress.
3. The internal stress is gradually reduced at the same rate everywhere on the soft zone walls.

The main advantage of this approach is the ability to have complete knowledge of the state of stress within the soft zone until numerical instability takes place. The internal stress reduction (ISR) can be expressed

$$\mathrm{ISR}_i = \frac{\sigma_{\mathrm{initial}} - \sigma_i}{\sigma_{\mathrm{initial}}} \tag{5.2}$$

where $\sigma_{initial}$ is initially stress around the soft zone and σ_i is internal stress at the *i* th step.

Code verification. The code is verified for plane-strain conditions. The closed-form Kirsch solution applies to a circular cavity of radius a and internal stress p_i in homogeneous isotropic, linear elastic medium subjected to far-field stresses. The stress distribution around the cavity is (Kirsch, 1898)

$$\sigma_r = p_i \frac{a^2}{r^2} + \frac{\sigma_{v\infty} + \sigma_{h\infty}}{2}\left(1 - \frac{a^2}{r^2}\right) + \frac{\sigma_{v\infty} - \sigma_{h\infty}}{2}\left(1 + \frac{3a^4}{r^4} - \frac{4a^2}{r^2}\right)\cos 2\theta \qquad (5.3a)$$

$$\sigma_\theta = -p_i \frac{a^2}{r^2} + \frac{\sigma_{v\infty} + \sigma_{h\infty}}{2}\left(1 + \frac{a^2}{r^2}\right) - \frac{\sigma_{v\infty} - \sigma_{h\infty}}{2}\left(1 + \frac{3a^4}{r^4}\right)\cos 2\theta \qquad (5.3b)$$

where the radial σ_r and circumferential σ_θ stresses at distance r and at an angle θ are a function of far-field stresses $\sigma_{v\infty}$ and $\sigma_{h\infty}$.

An initial pressure $p_{int} = 5\sigma_{v\infty}$ is applied first and the internal pressure is gradually reduced. A perfect match between the analytical and numerical predictions requires proper mesh refinement near the cavity and implies higher computational costs (see also Potts, 2003; Rajendran, 2010). Figure 5.1 shows the high agreement attained between the closed-form and numerical simulation for the stress relaxation module when a high resolution mesh is used around the cavity.

5.4 Parametric study – Methodology and General Trends

Constitutive model and material parameters. Cavities have a rectangular cross section. The homogeneous soil mass is modeled as a Modified Cam Clay material to capture the pressure-dependent soil strength and volume change upon shear (Roscoe and Burland, 1968). Material properties are summarized in Table 5.3. The initial void ratio is calculated from constitutive parameters, the preconsolidation pressure p_c', and the current geostatic pressure p'.

This comprehensive parametric study explores the effect of soft zone depth z_0, the number of nearby soft zones, critical state friction angle ϕ_{cs}, preconsolidation, and

internal stress reduction ISR within the soft zone (variables are summarized in Table 5.4). Different levels of internal stress reduction ISR capture different degrees of dissolution. The internal stress reduction ISR is limited by numerical instabilities and mesh distortion (the determinant of the Jacobian matrix approaches zero and the stiffness integral cannot be solved). In the absence of any cohesive strength, most simulations presented herein reach numerical instability between ISR~0.8 and 0.95 (Note: there is cohesion in situ, otherwise, there would be no open cavities larger than $3 \cdot D_{50}$ to $5 \cdot D_{50}$ where D_{50} is the median grain size). Preloading effects are simulated by changing the k_0 ratio for a given critical friction angle M. Then, the initial overconsolidation ratio OCR is (Borja and Lee, 1990)

$$OCR = \frac{p_y'}{p_0'} = \frac{p_y'}{p' + \frac{q^2}{M^2 p'}} \tag{5.4}$$

where p_y' is the size of the yield surface and p_0' is the equivalent preconsolidation pressure corresponding to the current stress state p'. Cavities are assumed to be of rectangular shape in agreement with layered stratigraphies observed at SRS, and to facilitate the soft zone simulation. A study of soft zone geometry showed that geometry affects stress conditions at the soft zone springline more than near the crown (Greenspan, 1944), and that deviations from circularity exacerbate stress concentrations that lead to numerical instabilities at lower internal stress reduction ISR values.

Plane strain cases are simulated using eight-node biquadratic reduced integration elements (geometry and boundary conditions are shown in Figure 5.2). The domain size, boundary conditions, and mesh refinement affect the computed surface settlement profile and computational demand (Burd et al., 1994; Pang et al., 2005; Potts, 2003). The absence of lateral boundary effects on the worst case tested in this section is demonstrated in

Figure 5.3: the far-field surface settlement is close to zero and horizontal stresses are identical before and after the stress relaxation.

Governing dimensionless ratio. The normalization of results into dimensionless ratios facilitates the comparison of parametric studies and the identification of salient trends. Given the non-linear nature of the material behavior, we conducted all simulations in a dimensional regime, however, we explore prevailing trends in terms of normalized results using key dimensionless parameters.

Post-Processing. Given the regularity and smoothness of numerically computed displacement fields, each settlement profile at depth z is fitted with a Gaussian function; the inferred distance to the inflection point x_{inf} and the maximum settlement S_{max}. The post-processing module developed in Matlab computes the error e_i between the predicted and numerically computed settlement at node i

$$e_i = S_i^{<num>} - S_i^{<analy>} \tag{5.5}$$

and identifies the set $(x_{inf}, S_{max})_z$ that minimizes the square error norm

$$L_2 = \sqrt{\underline{e}^T \cdot \underline{e}} \tag{5.6}$$

General trends. As the soft zone depth increases in high friction and/or OC sediments, the displacement field evolves towards narrow troughs that may even become carrot-shaped (Figure 5.4 and Figure 5.5). Deeper cavities and higher preconsolidation ratios result in lower surface and subsurface settlements. Furthermore, Figure 5.6 shows fitted surface settlement profiles (z = 0) for two distinct cases, and slices of the error surface presenting the invertibility of the inflection point. The Gaussian model fits the surface settlement better for small stress reductions inside the soft zone (lower residual). However, the higher stress reduction increases the resolvability of the inflection (narrower error surface).

Summary trends for all fitted surface profiles show that the maximum surface settlement increases with higher internal stress reduction, shallower cavities, lower friction angle (higher frictional strength hinders the propagation of plastic deformations towards the ground surface), and in lightly overconsolidated sediments rather than highly overconsolidated sediments (Figure 5.7). The maximum subsurface settlement S/z_0 is only slightly larger near the soft zone than at the ground surface in all cases regardless of soft zone location, soil friction angle, and degree of preconsolidation (Figure 5.8).

The inflection point is a function of the soft zone depth (Figure 5.9): shallower cavities favor vertical displacement vectors and narrower settlement troughs, i.e., lower values of the inflection point. Inflection point trends with depth collapse into a quasi-single trend when the sediment is overconsolidated.

5.5 Analyses and Discussion

Surface settlement area compared to soft zone size. Figure 5.10 shows the area of the surface settlement profile normalized by the area that the *soft zone contracted* as a function of soft zone depth, overconsolidation, and friction angle. The ground volume loss is calculated by numerical integration of the surface settlement. The area ratio decreases for deeper cavities, higher friction angle, and higher preconsolidation. We highlight that surface settlements correspond to an internal stress reduction ISR = 70%, and that the soft zone has not fully vanished.

Applicability of Superposition Principle. The validity of the superposition principle is explored by comparing the sum of surface settlement areas caused by each single soft zone acting separately to that caused by all cavities concurrently formed in the sediment. Results in Figure 5.10 show that linear superposition method overpredicts surface settlements by a large amount in both low-and high-OCR sediments compared to the situation in which all cavities form simultaneously in the non-linear system.

Inflection Point Trends - Underlying Mechanism. The position of the inflection point with depth migrates towards the centerline during soft zone formation (Figure 5.9 and Figure 5.11). Internal stress reduction prompts early elastic deformation, followed by yielding, stress redistribution, and arching; eventually, the plastic zone propagates upward toward the surface. Consequently, inflection point trends are narrower and closer to the centerline at higher ISR.

Comparisons of Inflection Point. The numerically computed trend for inflection points with depth are compared against the empirical equation proposed by Mair et al (1993). Results presented in Figure 5.11 show that the empirical equation applies to overconsolidated sediments, and underestimates the width of the surface and subsurface settlement trough in low OCR sediments. Once again, we highlight the importance of the sediment stress history on displacement fields caused by subsurface soft zone formation.

5.6 Conclusions

Subsurface volume loss takes place in many geotechnical situations, and it is inherently accompanied by stress relaxation and displacements that may reach the surface.

- Subsurface volume loss and soft zone formation can be numerically simulated by gradually reducing the in situ state of stress in the predefined soft zone.
- Smaller and deeper cavities, higher friction angles, and higher preconsolidation ratio lead to smaller settlements at all depths.
- Surface and subsurface settlements are quite regular and can be adequately fitted with a two-parameter Gaussian function in the absence of pronounced distortions (e.g., shear localizations).
- The maximum settlement decreases towards the surface (but only slightly). The position of inflections points widens towards the surface, inflection point trends

with depth are narrower for higher OCR sediments (in fact, carrot-shaped displacement fields can develop for deep cavities in highly dilative media), and inflection points move towards the centerline during soft zone formation.

- Linear superposition of surface settlements caused by neighboring cavities overestimates deformations in low-and high-OCR sediments.
- Published guidelines for the position of the inflection point fail to recognize the profound effect of overconsolidation.

Note that the medium has been assumed to have no cohesion in all cases analyzed. The addition of cohesion could dramatically diminish the impact of soft zones/soft zone formation on displacement fields.

Table 5.1. Surface settlement – Empirical equations

Model parameters	Equation	Reference
S_{max}, x_{infl}	$S(x) = S_{max} \cdot e^{-\frac{1}{2}\left(\frac{x}{x_{infl}}\right)^2}$	Peck (1969)
S_{max}, x_{infl}	$S(x) = S_{max} \cdot e^{-\frac{1}{3}\left(\frac{x}{x_{infl}}\right)^{1.5}}$	Jacobsz *et al.* (2004)
S_{max}, x_{infl}, β Note: $\alpha = f(\beta)$	$S(x) = S_{max} \cdot \frac{1}{1+\alpha\left(\frac{x}{x_{infl}}\right)^{\beta}}$	Celestino *et al.* (2000)
S_{max}, x_{infl}, β Note: $\alpha = f(\beta)$	$S(x) = S_{max} \cdot \frac{\alpha}{(\alpha-1)+e^{\beta\left(\frac{x}{x_{infl}}\right)^2}}$	Vorster *et al.* (2005)

Table 5.2. Inflection point (z_0: cavity depth; R: cavity radius).

(a) *Ground surface*

Equations		Parameters	References
$\frac{x_{infl}}{R} = \left(\frac{z_0}{2R}\right)^n$		z_0, n, R	Peck (1969) Schmidt (1969) Clough and Schmidt (1981)
$x_{infl} = 0.25(z_0 + R)$	Loose sand	z_0, R	Atkinson and Potts (1977)
$x_{infl} = 0.25(1.5z_0 + R)$	Dense sand and OC clay	z_0, R	
$x_{infl} = 0.28z_0 - 0.12$	Sands	z_0	O'Reilly and New (1982)
$x_{infl} = 0.43z_0 + 1.1$	Stiff clay	z_0	
$x_{infl} = 0.5z_0$		z_0	Mair (1993)

(b) *Subsurface*

$x_{infl}(z) = 0.175z_0 + 0.325(z_0 - z)$	K, z_0,z	Mair (1993)
$x_{infl}(z) = R \cdot \left(\frac{z}{2R}\right)^{0.8} \cdot \left(\frac{z_0 - z}{z_0}\right)^n$	R,z, z_0, n	Moh, Z. C. *et al*. (1996)

Table 5.3. Material properties – Modified Cam clay ($\kappa = 0.1 \cdot \lambda$; AC indicates axial compression).

Unit weight γ [kN/m^3]	17
Isotropic compression index λ	0.1
Isotropic recompression index κ	0.01
MCC strength M (for AC)	1.2, 1.42, 1.64
Drained Poisson's ratio υ	0.3
Void ratio at 1kPa e_{1kPa}	1.28
Earth pressure k_0	0.5

Table 5.4. Parametric study.

z_0/h	5	10	25	50
# Soft zones	1	3	5	
ϕ_{cs} [^{0}]	30	35	40	
OCR	1.3		4.0	
ISR	0 – 0.7			

< Soft zone dimensions >

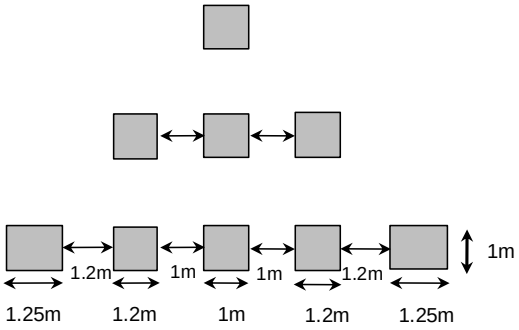

Note:

1. ISR is Internal stress reduction
2. ϕ_{cs} implies the constant volume friction angle
3. The symmetry condition is considered

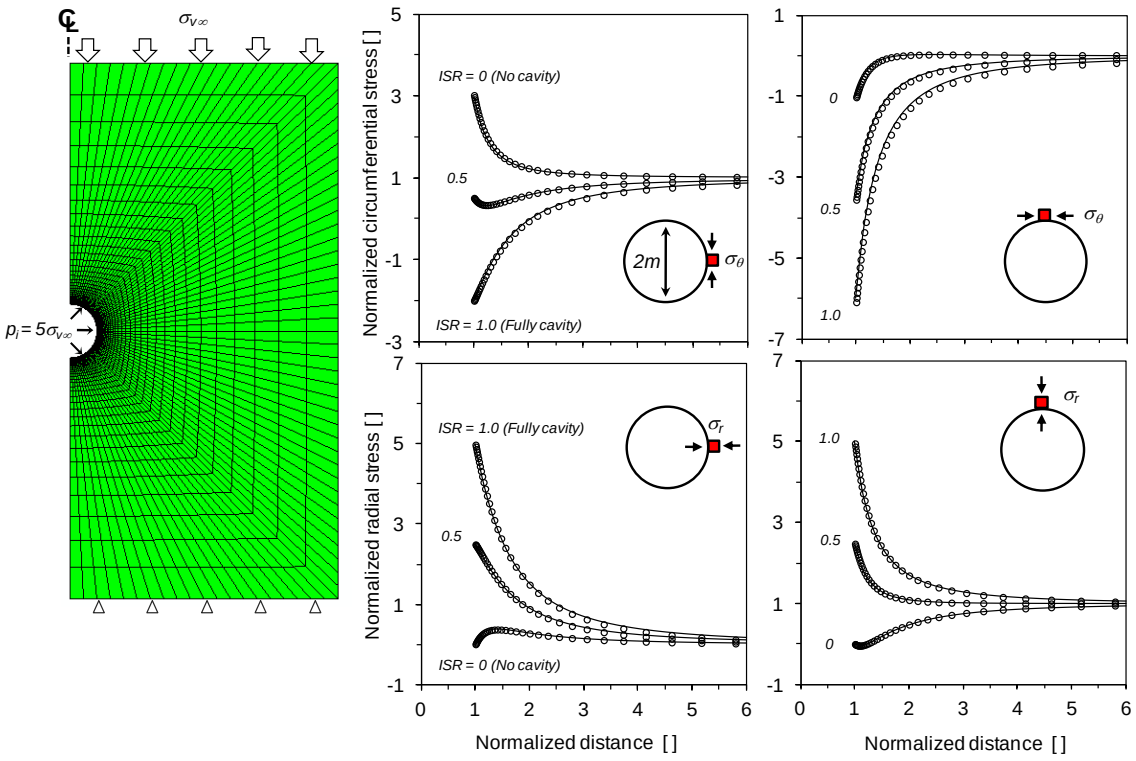

Figure 5.1. Stress relaxation module - Code verification (Solid lines indicate the close-form solution; points are numerically computed values).

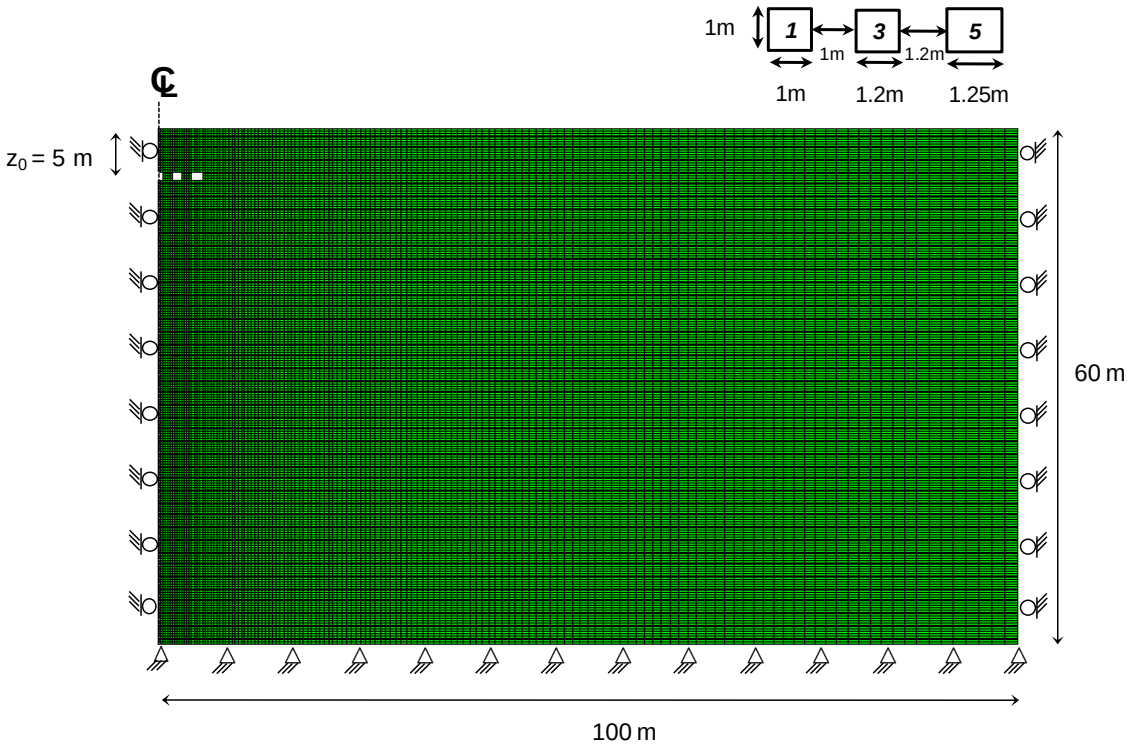

Element type: CPE8R (8-node biquadratic plane strain quadrilateral, reduced integration)

Number of elements: 33600

Figure 5.2. Geometry - Boundary conditions

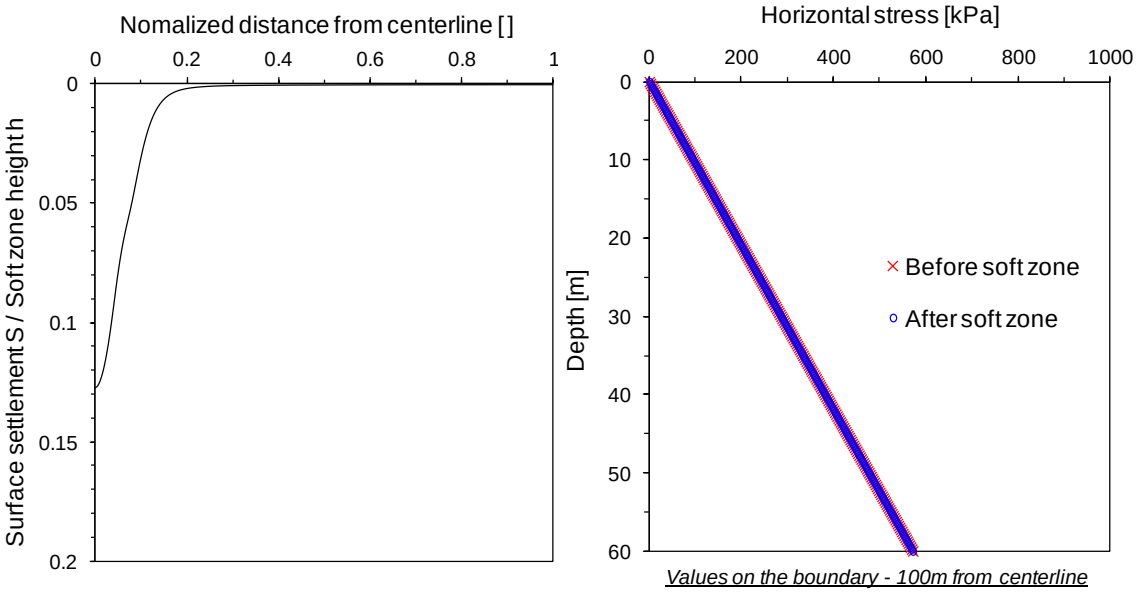

Figure 5.3. Boundary effect (Case: $z_0/h = 5$; $\phi_{cs} = 30^o$; Five soft zones)

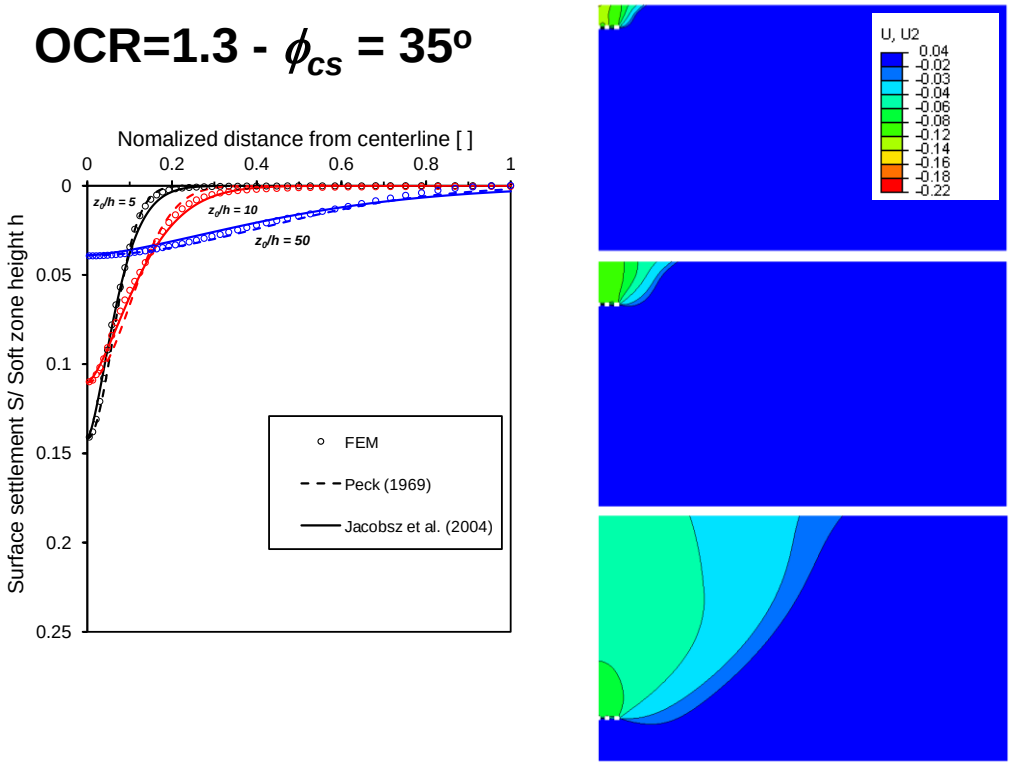

Figure 5.4. Normalized settlements and displacement fields – Quasi NC sediment

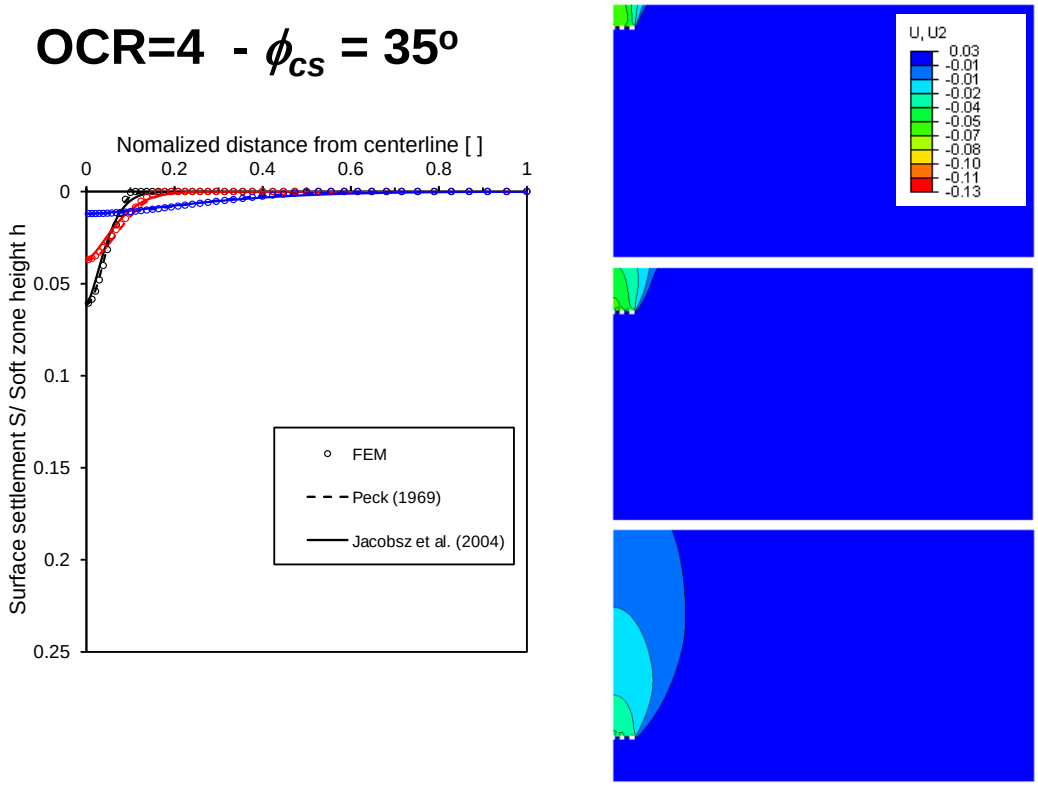

Figure 5.5. Normalized settlements and displacement fields – OC sediment

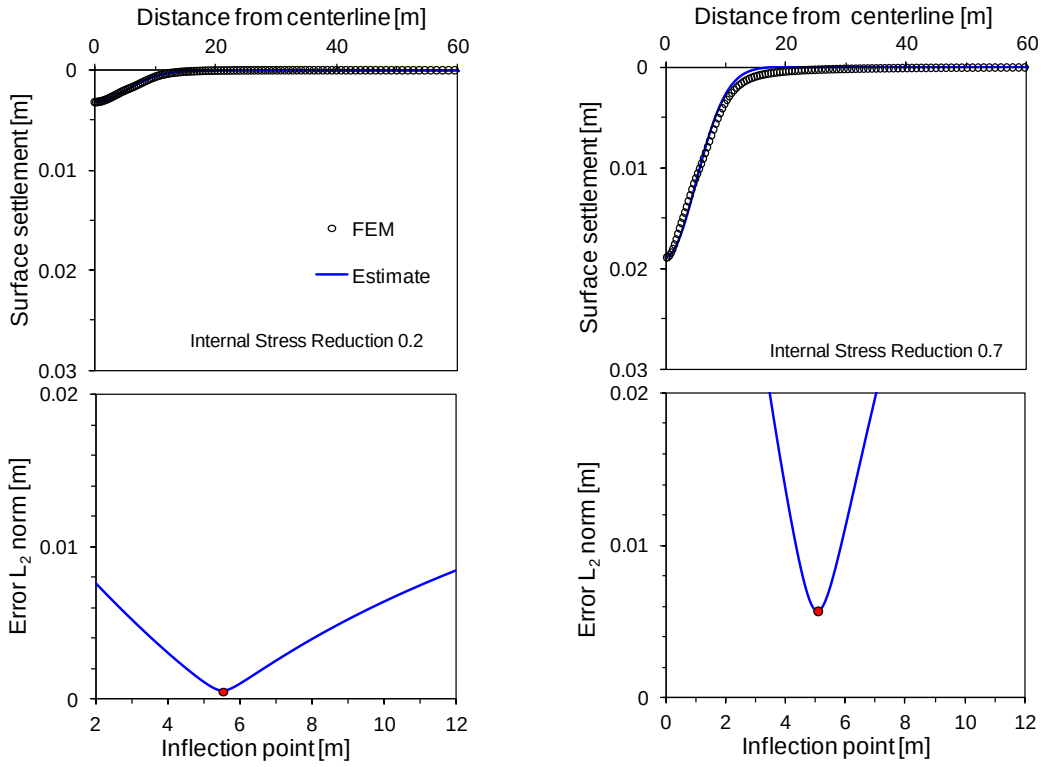

Figure 5.6. Surface settlements - Gaussian function

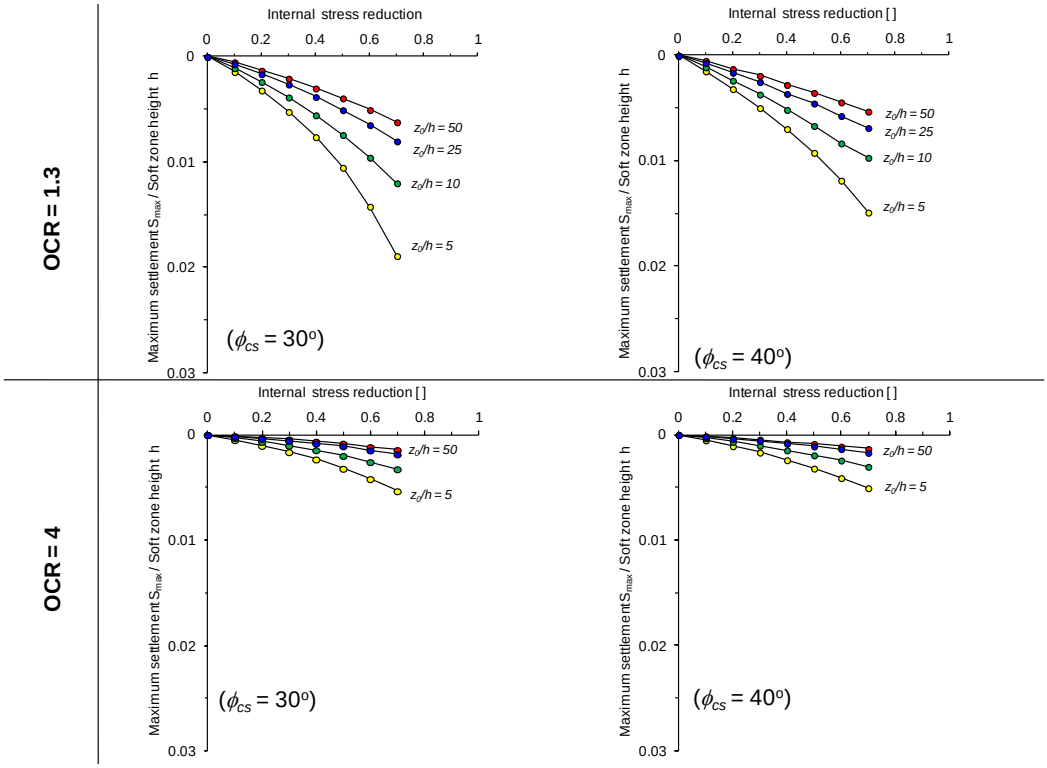

Figure 5.7. MaximumSurface settlement S_{max} (One soft zone)

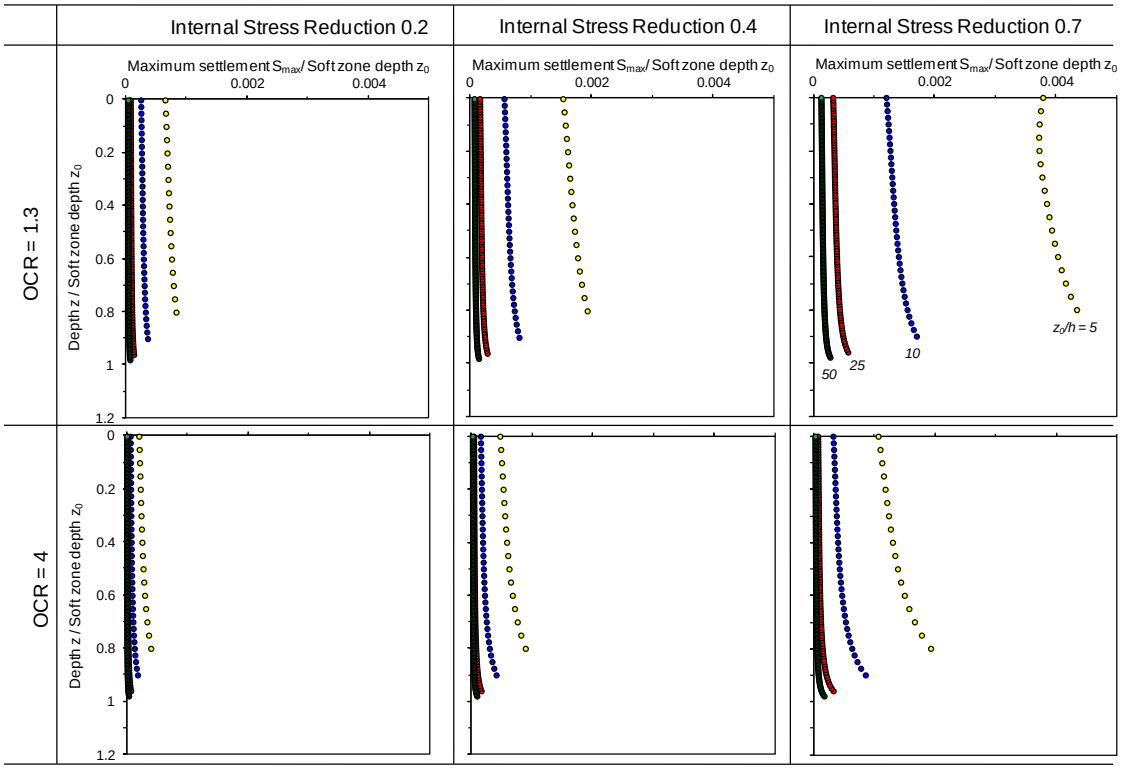

Figure 5.8. Subsurface settlement profiles (One soft zone; $\phi_{cs} = 30^0$)

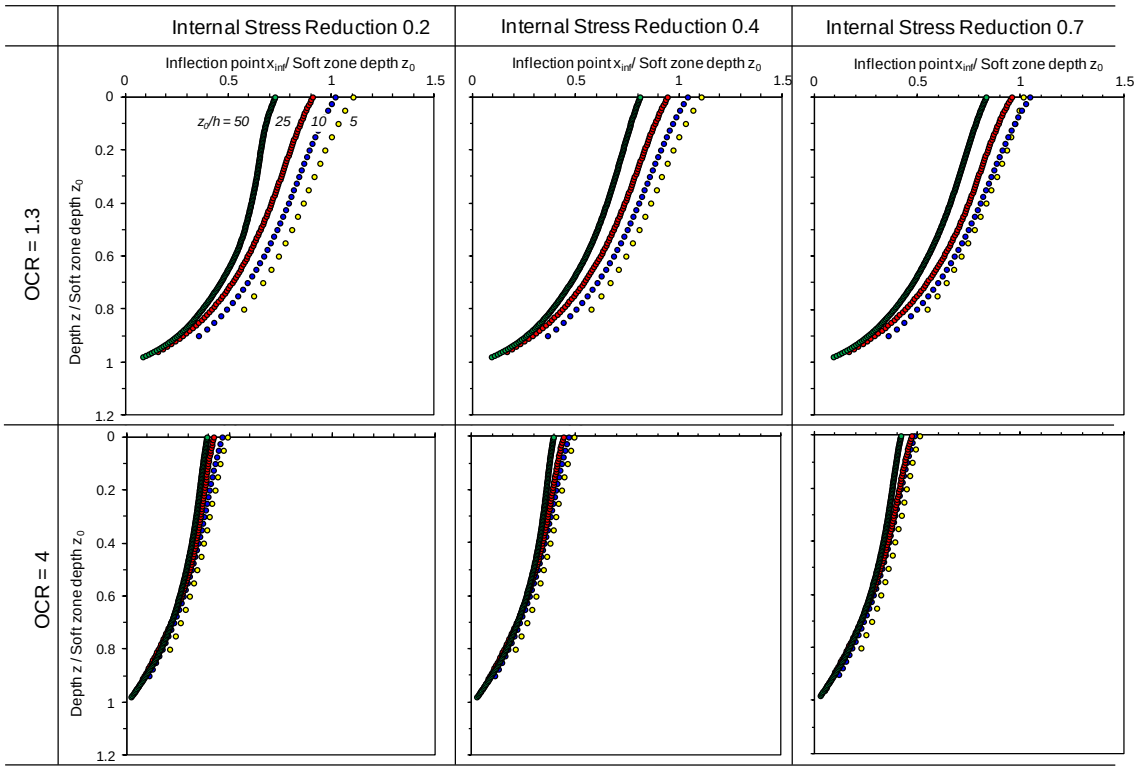

Figure 5.9. Subsurface inflection point (One soft zone; $\phi_{cs} = 30^0$)

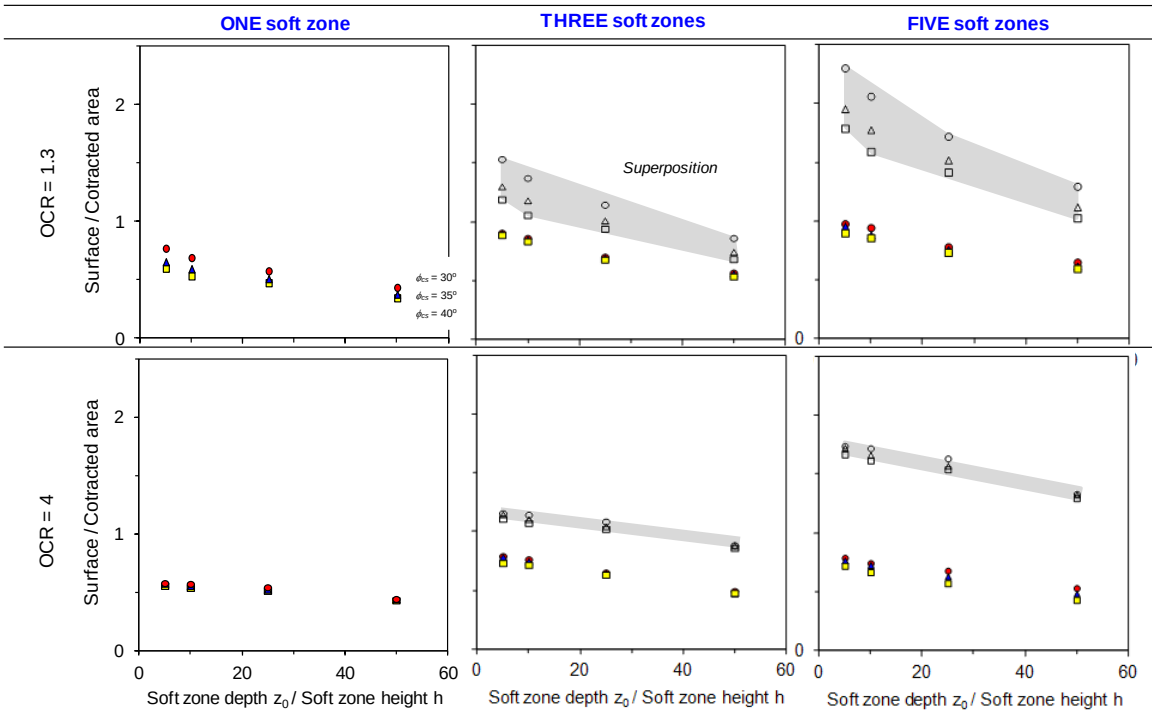

Figure 5.10. Applicability of superposition principle

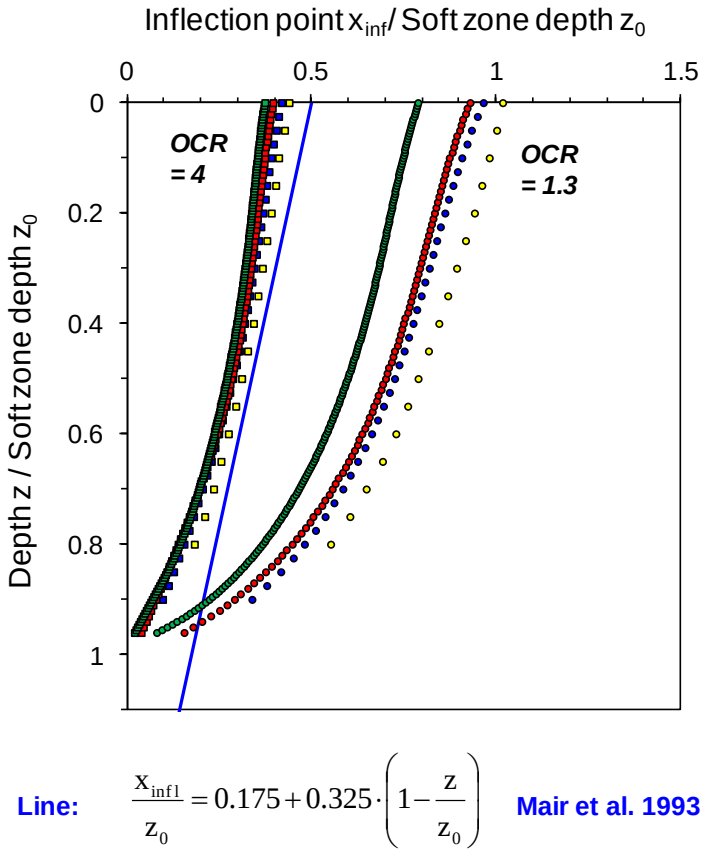

Figure 5.11. Position of inflection point vs. depth (ISR = 0.7; $\phi_{cs} = 30^0$)

CHAPTER 6

EFFECT OF LOCALIZED DISSOLUTION ON SHALLOW FOUNDATIONS

6.1 Introduction

Shallow foundations are typically designed to satisfy bearing capacity and settlement criteria compatible with structural tolerance. Relatively simple computational schemes are available for simple subsurface conditions, such as elastic solutions for settlement and plasticity solutions for bearing capacity. The $N\gamma$ coefficient in bearing capacity equations significantly depends upon geometric assumptions made in kinematically admissible solutions and other effects such as the role of the sediment self-weight effect on shear strength and wedge geometry (e.g., Prandtl log spiral; Terzaghi, 1943; Meyerhof, 1963; Vesic, 1973; Chen, 1975). Numerical simulations underscore the variation in bearing capacity coefficient $N\gamma$ (Griffiths, 1982; Frydman and Burd, 1997; Hjiaj et al., 2005; Loukidis and Salgado, 2009).

The situation is aggravated when shallow foundations rest on sediments that have experienced mineral dissolution before the footing load, or that may experience subsurface dissolution during the life of the structure. Previous studies used analytical, numerical, and experimental methods to evaluate the bearing capacity of a strip footing above a soft zone (Baus and Wang, 1983; Badie and Wang, 1984; Wang and Badie, 1985; Wang and Hsieh, 1987; Azam et al., 1991; Hsieh, 1991; Crapps, 2010). These studies showed that cavities deeper than a critical depth have a negligible effect on bearing capacity, and that the effect of cavities shallower than the critical depth depends on the relative size and depth of the foundation and the soft zone. However, general guidelines are still limited and incomplete.

A numerical study conducted to explore the effect of subsurface volume contraction on shallow foundations is reported herein using material characteristics that are relevant to the Savannah River Site. The parametric study considers footing size B, soft zone location D, dilation angle ψ, and load-dissolution history (stress relaxation-before-footing and footing-before-stress relaxation).

6.2 Preliminary simulations: Mesh design

Mesh Refinement. The numerically computed bearing capacity factor N_γ is significantly affected by mesh size (Griffiths, 1982; Manoharan and Dasgupta, 1995; Woodward and Griffiths, 1998; Day and Potts, 2000). In a preliminary study, we compared numerically computed bearing capacity factors with analytical expressions widely used in design. A parametric study was conducted to address the trade-off between mesh size, computational accuracy, and cost. In particular, high mesh refinement was imposed near footings and cavities.

Footing Model. Different footing widths are simulated by varying the number of nodes subjected to controlled displacement. Smooth and rough, flexible and rigid footings are numerically modeled for this study (details in Table 6.1). The rough and rigid footing is simulated by deformation-controlled vertical node displacement, and facilitates the determination of the bearing capacity. The resistance mobilized at a given vertical displacement is the integral of the average vertical component of stress acting on the first row of Gaussian integration points below the displaced nodes. The mesh geometry is selected so that predicted bearing capacity values are mesh independent (Woodward and Griffiths, 1998).

Numerical Environment. The commercial finite element software ABAQUS is used for these 2D plane-strain simulations. The medium is represented using eight-node biquadratic reduced integration elements (CPE8R). Lateral boundaries are located far from the footing edge so that there are no boundary effects on deformations and bearing resistance; vertical displacement is allowed on side boundaries, the bottom boundary is pinned, and the top surface is free (Figure 6.1). The simulated space is 40 m high and 80 m wide. The soil is homogeneous and it is modeled using an elastic perfectly plastic constitutive model with a Drucker-Prager failure criterion (Drucker and Prager, 1952; material properties are summarized in Table 6.1).

Boundary Effects. Results in Figure 6.2 show that the far-field surface settlement is almost zero, and the horizontal stresses on the vertical lateral boundaries subjected to zero lateral strain conditions are identical before and after stress relaxation, and footing loading. Therefore, the modeled domain avoids boundary effects.

Preliminary Results - Verification. The variation of the numerically computed $N\gamma$ value with friction angle is plotted together with analytically predicted $N\gamma$ values using classical bearing capacity equations in Figure 6.3. The Prandtl solution overestimates $N\gamma$, while the modified Terzaghi's solution leads to conservative estimates where a reduced friction angle $\tan\phi^* = 2/3 \tan\phi$ is used in computations (Note: values for the modified Terzaghi's solution are obtained with a reduced friction angle ϕ^* so that $\tan\phi^* = 2/3 \tan\phi$ - refer to Das, 1999). The value of $N\gamma$ depends on dilation (see also Frydman and Burd, 1997), and the effect of dilation is most pronounced for sediments with higher constant volume friction angles. The Hansen (1970) solution overestimated values but it is close to the computed $N\gamma$ obtained for dilation equal to friction $\psi=\phi$ i.e., associated flow rule (see

also Potts, 2003). Results in Figure 6.3 highlight the sensitivity of bearing capacity to friction angle and the spread between analytical predictions.

6.3 Parametric study and results

Scope. The parametric study explores the effect of footing size B, soft zone depth z0, dilation angle ψ, internal stress reduction ISR, and the soft zone formation vs. loading history, i.e., stress relaxation-before-footing and footing-before-stress relaxation on the foundation bearing capacity. A surcharge load q_0 = 17 kPa is applied on the surface to simulate a nominal burial depth, and the selected soft zone is ~1.0 m high and 2.0 m wide in all cases. Different levels of internal stress reduction ISR capture different degrees of dissolution. The scope of the parametric study is summarized in Table 6.2.

The stress relaxation module based on the internal stress reduction ISR method is employed in these simulations (refer to Chapter 5). The internal stress reduction inside the soft zone is limited by numerical instability and mesh deformation (when the determinant of the Jacobian matrix approaches zero, the stiffness integral cannot be solved). In general, we exceed ISR~0.5 (the deformed configuration around the soft zone is shown in Figure 6.4).

Results. Load-displacement curves are shown in Figure 6.4 and Figure 6.5. The applied load is normalized by the bearing capacity in the absence of cavities. Shallow cavities interact with the footing, the ultimate bearing capacity is significantly decreased proportionally to the internal stress reduction in the soft zone, but dilation diminishes the effect of cavities beneath the footing (z_0/B = 1.7 - Figure 6.4). The foundation response is almost insensitive to the presence of deep cavities (z_0/B = 5.7 - Figure 6.5). The load-displacement shows a more brittle response in dilative sediments (note: elastic properties are kept the same for all simulations).

Computed bearing capacity values are summarized in Figure 6.6 in terms of the bearing capacity in the presence of the soft zone normalized by the footing bearing capacity in the absence of any soft zone. The loss in bearing capacity is worst when the footing size is equal to the soft zone width B = w and $\psi = 0$ (note: in the absence of cavities, the bearing capacity increases with footing width). Deeper cavities have diminishing effects on bearing capacity. For dilation equal to the friction angle $\psi = \phi$ (normality), the reduction in bearing capacity is gradual with ISR and proportional to the footing size, because dilatancy hinders the propagation of plastic deformations underneath the footing from the soft zone to the top. The transition from shallow to deep anomaly depends on z_0/B (about 3 to 4), but this value is affected by anomaly size B/w, dilatancy ψ, and internal stress reduction ISR.

Consider next the settlement experienced by all footings subjected to an initial load equal to 1/3 the bearing capacity in the medium without soft zone (FS = 3). After loading, the soft zone is gradually formed by internal stress reduction from the initial equilibrium condition in the sediment subjected to gravity and footing load (load-before-stress relaxation). The surface settlement that the footing experiences during the soft zone formation process is normalized by the surface settlement produced by the applied load. Results are summarized in Figure 6.7. Shallow cavities increase surface settlement, particularly when the footing width B is equal to the soft zone width w in a medium with dilatancy $\psi = 0$. Dilation markedly reduces surface settlements. Numerically instability occurs as the settlement increases rapidly with the reduction of internal stress in the soft zone. Once again, the transition from deep to shallow behavior varies with anomaly size B/w, dilatancy ψ, and internal stress reduction ISR.

6.4 Discussion

Failure modes. Bearing capacity failure can involve general shear failure, local shear failure, and punching shear failure (Vesic, 1973). In particular, the punching shear failure mode involves primarily vertical displacements, and the soil outside the loaded region remains relatively immobile during the failure. Figure 6.8 and Figure 6.9 show displacement fields beneath footings near failure. The failure mode in the absence of cavities exhibits general shear failure characteristics. The presence of shallow cavities "attracts" the displacement field and the failure mode resembles the punching mode. The displacement field resembles a funnel when the depth-to-width z_0/B is low; however, quasi-vertical or even carrot-shaped displacements can develop in deep cavities and dilatant soils.

Friction angle. Friction angle plays a controlling role in deformations, strength and failure mode for footings placed on sediments with subsurface cavities. Yet, there is large uncertainty on the selection of friction angle (Cho et al., 2006; Santamarina and Shin, 2009; Rouse, 2010); for example: the friction angle in lateral compression can be $\phi_{LC} \approx 1.5\phi_{AC}$ (due to flow conditions during yield), dilatancy is stress dependent, and post-peak strain softening leads to progressive failure (see for example Rowe and Peaker, 1965).

Strain criterion to define bearing capacity. In most cases, the footing response during load tests resembles a hyperbolic trend (Note: the load-displacement curve exhibits a sudden break and even strain softening in sensitive clays or cemented soils). The lack of break in load-displacement trends on sandy soils can be attributed to the evolution of mobilized friction beneath the foundation during loading; the required displacement depends on initial relative density, footing size and the state of stress (Beer, 1970; Coop

et al., 2004). Furthermore, back-calculated bearing capacity factors show significant variation in mobilized friction angle with footing size (Deschamps, 1995).

Several interpretation methods have been suggested to define the failure load in this case (Amar, 1994; Lutenegger and Adams, 1998; Briaud and Gibbens, 1999; Kulhawy, 2004; Elhakim, 2005). The limiting normalized displacement frequently adopted in practice is S/B = 0.02 for clayey soils and S/B = 0.1 for sandy soils (Mayne and Woeller, 2014). In this study, the normalized footing response curves show that the ultimate bearing capacity is reached at relatively low relative settlements (e.g., S/B ≈0.01) because soils beneath the footing are assumed to have an elasto-plastic behavior.

6.5 Conclusions

A comprehensive numerical study was implemented to identify and quantify the effect of cavities on the response of shallow foundations. Results show that:

- Careful mesh refinement is required to avoid numerical effects.
- Shallow cavities interact with the footing, lower the bearing capacity, increase settlements, and promote local-punching failures.
- When the footing size is much wider than the soft zone size B>>w, failure remains global (and embodies the soft zone); global shear failures also develop when B<<w and z_0>w. Hence, the worst condition corresponds to B~w; in this case, the system is prone to punching shear failure.
- The critical depth that separates shallow from deep cavities depends on the ratio of soft zone depth to footing width z_0/B, anomaly size B/w, dilatancy ψ, and the internal stress reduction ISR in the soft zone or cavity. As a guiding rule, the critical depth is about z_0/B~3 to 4 when B/w~1 (the most critical case)
- Dilatancy increases bearing capacity, promotes a more brittle load-settlement response, hinders settlements even in the presence of anomalies, and leads to

narrower subsurface settlement troughs.

Note that the medium was modeled with no cohesion. Yet, open cavities observed at the Vogtle excavation confirm marked cementation in the layer above the crown, otherwise, grains would flow and fill any developing soft zone as dissolution takes place and no explicit soft zone larger than a few grain diameters could form. Increased strength on the layer above the soft zone by the addition of cohesion would lead to open cavities, yet, these cohesive layers would dramatically diminish the impact of soft zone/cavity formation on displacement fields above the soft zone/cavity; indeed, the soft zone/cavity would remain “hidden” by the strong layers.

Table 6.1. Simulations

	Footing type	Conditions
Footing characteristics	Smooth (δ =0)	Nodes are free to move horizontally
	Rough ($\delta \geq \phi$)	Constrained horizontal displacement
	Flexible	Load-control (Uniform load)
	Rigid	Displacement-control (Uniform displacement)

Material Properties Drucker-Prager	
Unit weight γ [kN/m^3]	17
Young's modulus E [MPa]	300
Cohesion c [kPa]	0
Friction ϕ [^{o}]	30
Dilation Ψ [^{o}]	0 and 30
Drained Poisson's ratio υ	0.3

Table 6.2. Parametric study (Surcharge: q_o = 17 kPa; Soft zone: w ≈ 2 m - h ≈ 1 m)

Footing size B [m]	**Zone depth z_0 [m]**	**Dilation Ψ [^{o}]**	**Possible Stress Relaxation Histories**	
			Load After Stress Relaxation	**Load Before Stress Relaxation**
1.2	3.4	0	1) Reduce internal stress 2) Displace over B 3) Determine bearing capacity 4) Repeat for ISR= 0,0.1,0.2,0.4,0.5	1) Load footing to a FS=3 2) Form soft zone by gradual ISR 3) Monitor footing settlement 4) Repeat for all cases
	7.7			
	11.4	ϕ		
2.0	3.4	0		
	7.7			
	11.4	ϕ		
3.8	3.4	0		
	7.7			
	11.4	ϕ		

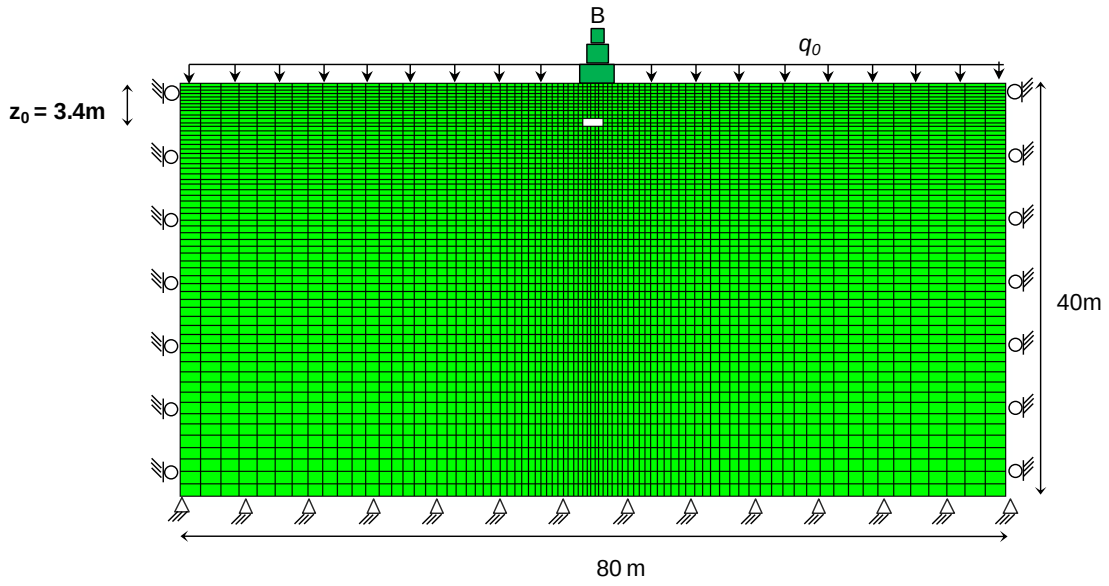

Figure 6.1. Mesh adopted for this analysis; element type - CPE8R (8-node biquadratic plane strain quadrilateral, reduced integration)

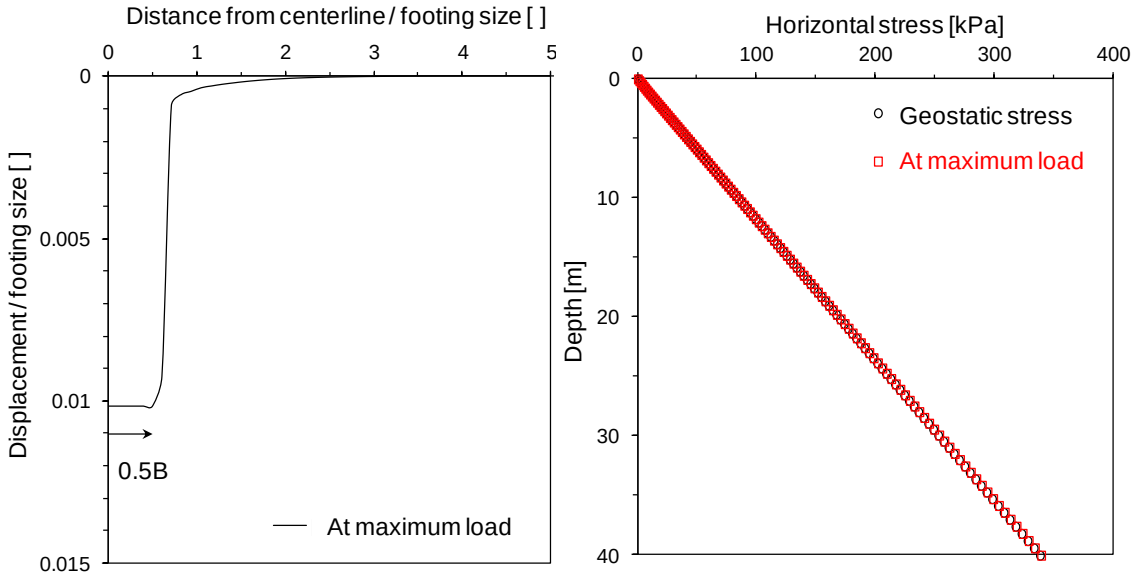

Figure 6.2. Boundary effect; Case: B = 2.0 m; z_0 = 3.4 m; ϕ_{cs} = 30°; ψ = 0; ISR = 0.5

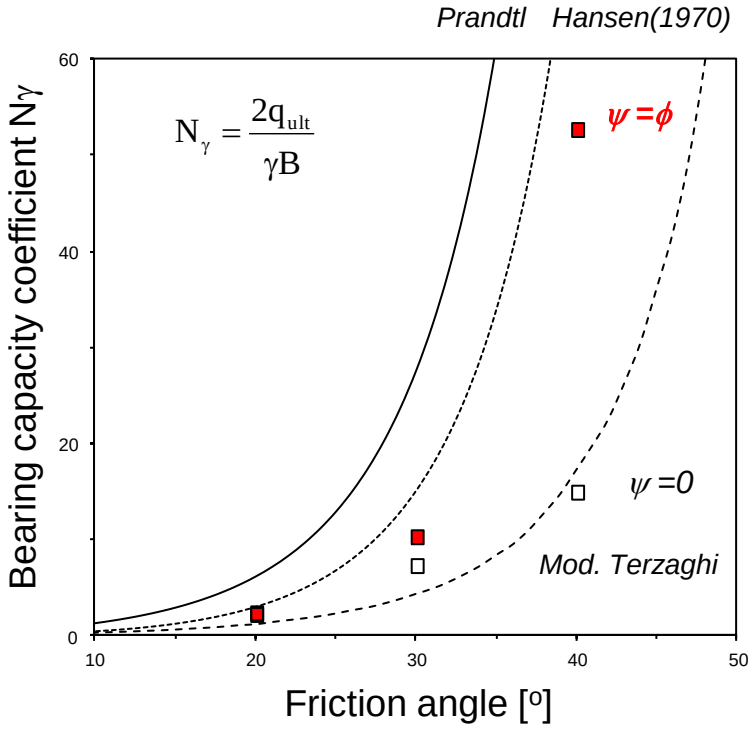

Figure 6.3. Bearing capacity coefficient Nγ (γ ≠ 0, c = 0, and q_o = 0)

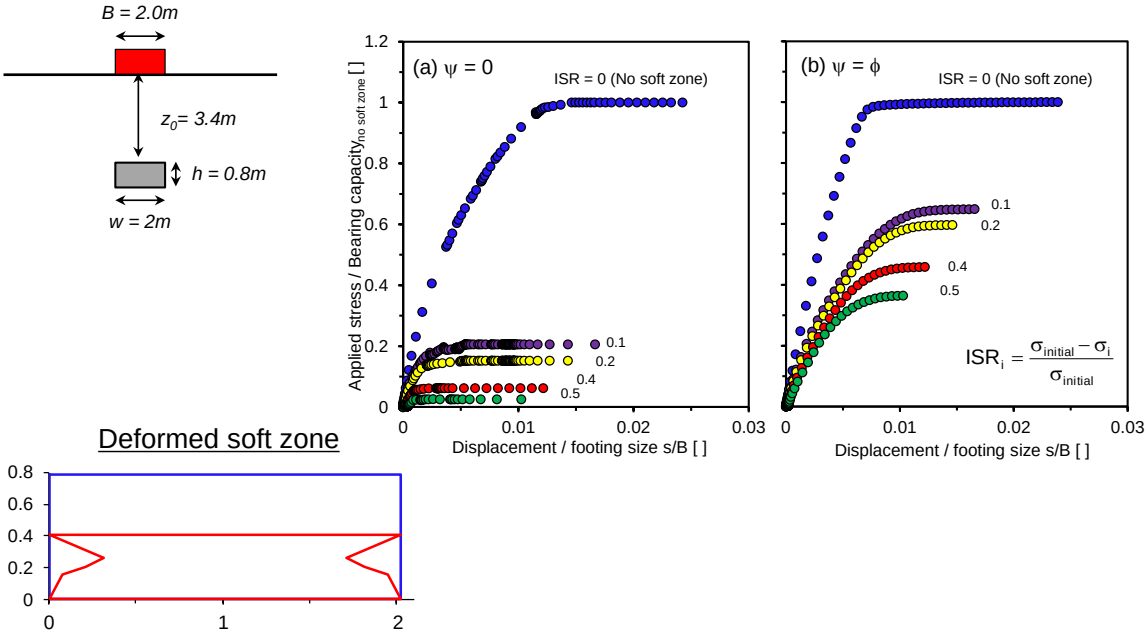

Figure 6.4. Load-displacement - Soft zone formation (z_0/B = 1.7; ψ = 0; ISR = 0.5)

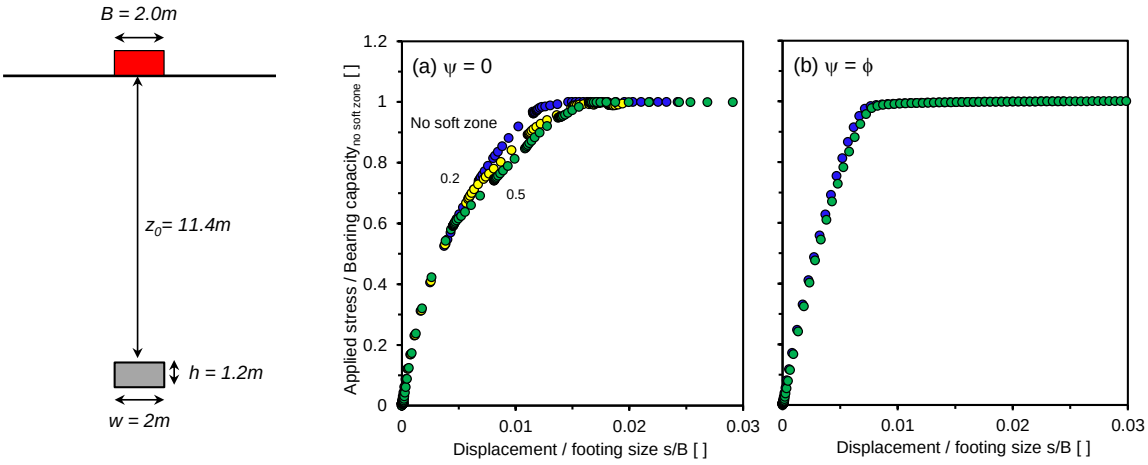

Figure 6.5. Load-displacement - Soft zone formation (z_0/B = 5.7)

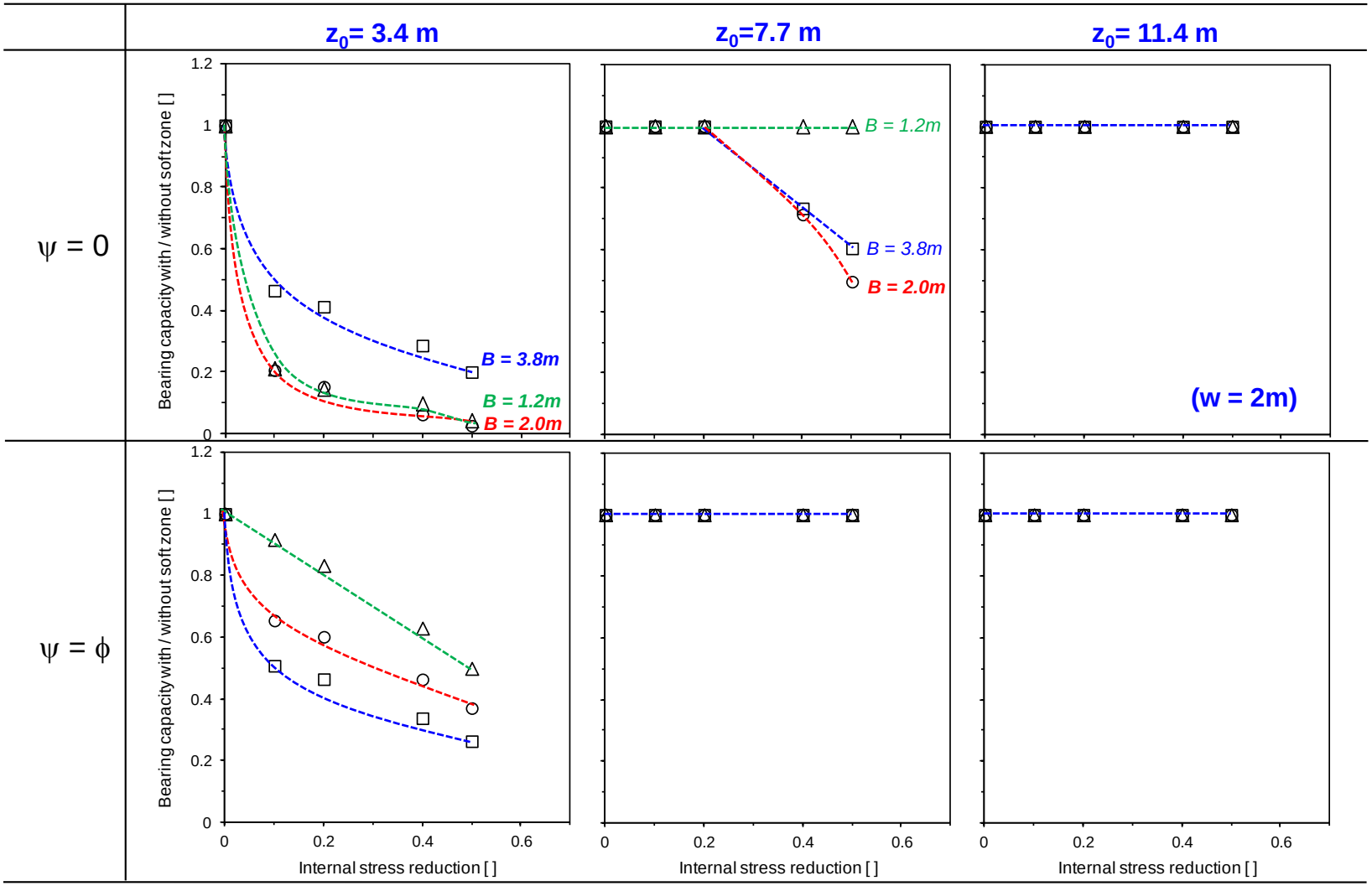

Figure 6.6. Load-after-stress relaxation: bearing capacity (w = 2 m)

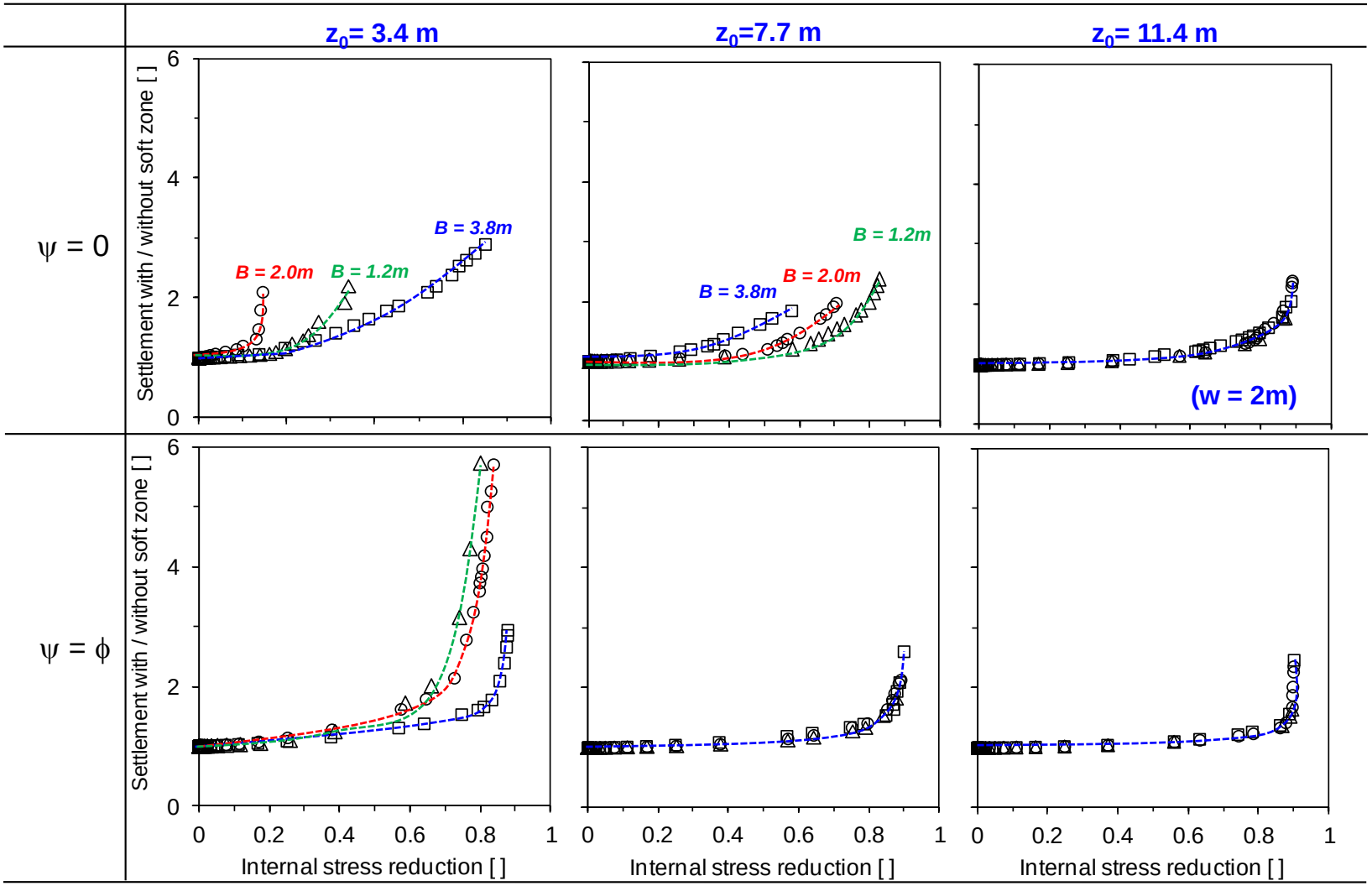

Figure 6.7. Stress relaxation-after-load: settlement @ FS = 3 (w = 2 m)

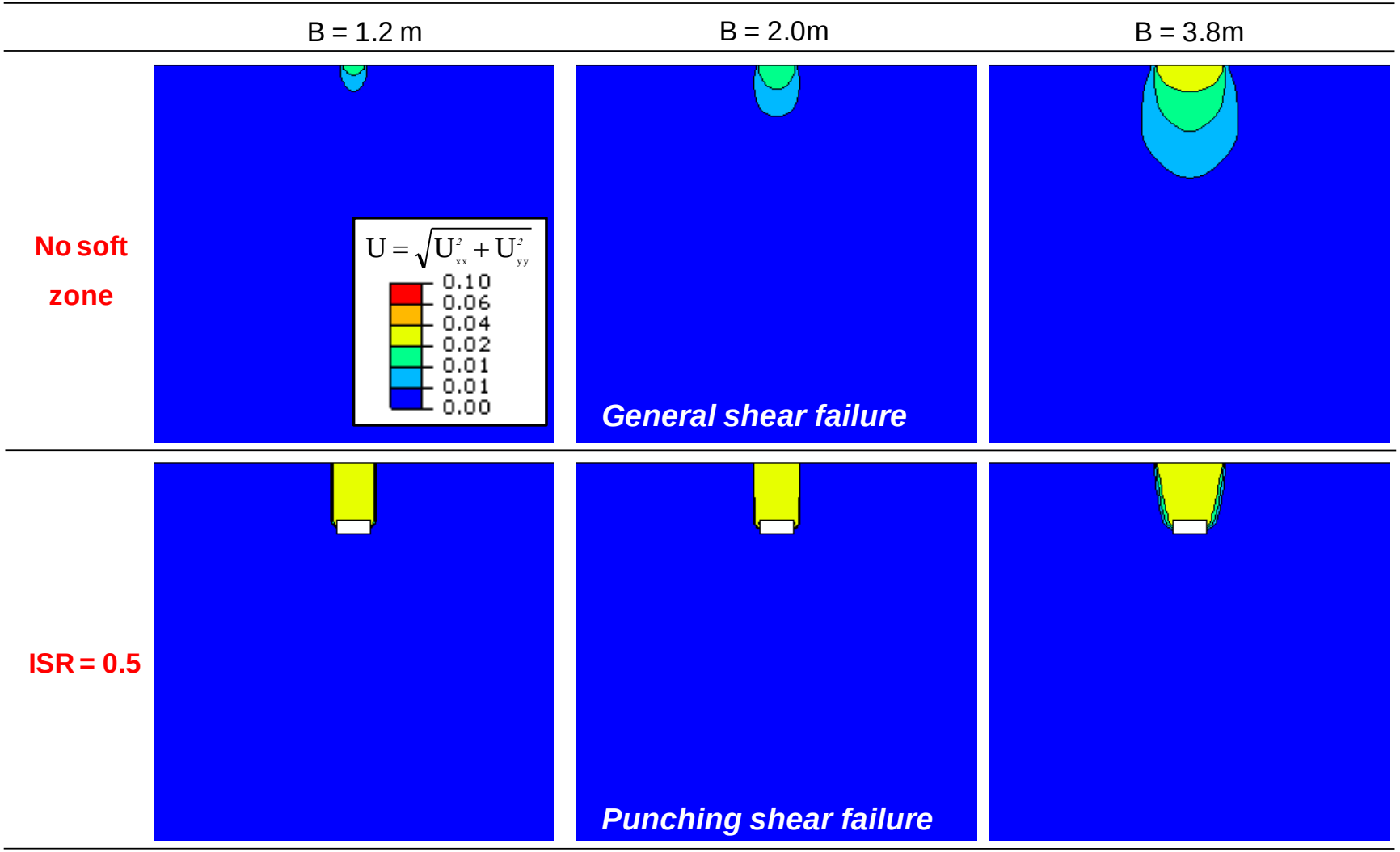

Figure 6.8. Displacement field (ψ = 0; z_0 = 3.4m; w = 2.0m)

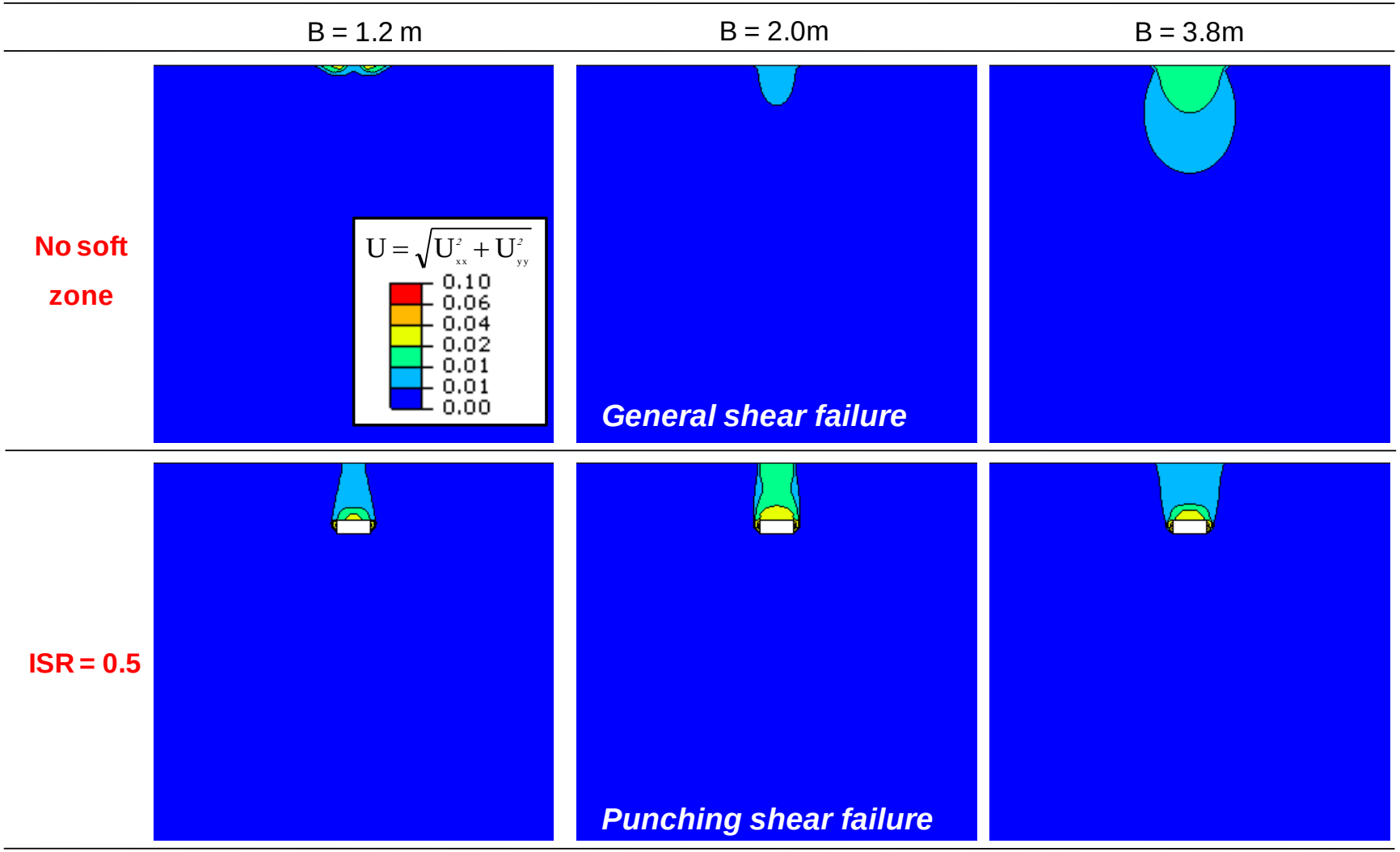

Figure 6.9. Displacement field ($\psi = \phi$; z_0 = 3.4m; w = 2.0m)

CHAPTER 7

SRS CASE HISTORY – BACK ANALYSIS

7.1 Introduction

Numerical methods are increasingly used for design and construction decisions. But predicted and anticipated settlements still show pronounced differences. In most cases, these differences are not due to model choices or boundary conditions but reflect inadequate material parameters, in part due to limited understanding of the geological formation history. The availability of field data gathered for a nearby built structure or during construction provides invaluable information for model calibration/adaptation.

The calibration of constitutive models for soils poses significant challenges due to their inherent nonlinear (Hertzian) and nonelastic behavior (Mindlin) and stress-dependent stiffness, strength and dilatancy. Model calibration can be implemented through a formal inversion analysis that seeks to minimize the difference between field measurements and numerically computed results (Kavanagh, 1973; Gioda, 1980; Gioda and Maier, 1980; Cividini et al., 1981; Sakurai and Takeuchi, 1983; Gioda and Sakurai, 1987; Hollowell et al., 1988; Gioda and Locatelli, 1999; Calvello and Finno, 2004; Finno and Calvello, 2005; Alonso et al., 2010; Hashash et al., 2010). Guidelines and inversion algorithms can be found in Santamarina and Fratta (2005). Typically, such calibration exercises make extensive use of displacement measurements as they are economically and reliably gathered at multiple surface and subsurface locations.

This chapter documents a simple but robust back analysis procedure developed to calibrate our numerical model to the SRS field conditions. We apply the methodology to monitoring data gathered during the construction of the Defense Waste Processing

Facility. The calibrated model is used to estimate additional settlements due to the pre-existing cavities, new cavities, and a seismic event during the design life of the facility.

7.2 SRS case - Selection of material properties

This chapter deals with the specific case of dissolution cavities in the subsurface at the Savannah River Site (SRS) and their potential impact on near surface infrastructure. A comprehensive study of the formation history is documented in (Larrahondo, 2011). The selection of material properties needed for numerical simulations is documented in this section. The selection of material properties benefited from extensive studies conducted at SRS in the past (Burns and Roe Enterprises, 2001; WSRC, 2007), complementary experimental studies conducted in standard and large diameter oedometer tests (within Shelby tubes with shear wave monitoring – reported in progress reports), and extensive compilations of published data in the literature. A summary of selected properties follows.

Unit weight.

Figure 7.1 shows unit weights inferred from SCPT and laboratory-measured unit weights gathered from undisturbed specimens. It is important to highlight that the total weight decreases with depth, contrary to standard trends in sedimentary systems. This reversed trend is consistent with dissolution activity during the formation history of these sediments.

Small strain stiffness and compressibility. The small strain stiffness profile with depth is inferred from shear wave velocity data. Figure 7.2 shows measured shear wave velocity profiles gathered at SRS. Contrary to the stress-dependent stiffness observed in uncemented sediments (Herzian contact behavior), these profiles show an almost constant

stiffness with depth. Stress-dependent velocity in uncemented soils is demonstrated in Figure 7.3; for comparison, stress-independent travel times are observed for lightly cemented soils regardless of the state of stress (Figure 7.4). Light cementation is very sensitive to sampling-induced strains (Figure 7.5). Published data gathered in the field and after sampling are compiled in Figure 7.6.

These results confirm the sensitivity of small strain stiffness to sampling. We can conclude that SRS sediments are lightly cemented and could experience pronounced stiffness reduction upon sampling.

Do oedometer data provide relevant compressibility for SRS samples? Besides the sampling disturbance discussed above, two other effects were explored in this study (see also Santagata and Germaine, 2002; Ladd and DeGroot, 2003; Lunne and Long, 2006):

- extrusion from Shelby tube: it was investigated by testing within the Shelby tube (Figure 7.7)
- cap seating effects: a simple analysis demonstrates that soft boundary layers have a pronounced effect on the compressibility determined for these oedometer specimens, particularly when they are stiff, as in the case of cemented SRS sediments (Figure 7.8).

A preliminary back analysis of measured field settlements at SRS (details in the following section) confirmed the pronounced effects of sampling, extrusion, and seating effects. In fact, the compression ratio that adequately predicted measured settlements is lower than any value measured at the site using "undisturbed specimens". Indeed, Figure 7.9 shows ranges and mean values for C_r / (1+e) and C_c / (1+e) ratios measured for the different layers at the SRS; for comparison, the yellow band shows the range of compression ratios that are back-calculated to match measured settlements.

Strength: Friction angle. As noted earlier, there is pronounced uncertainty in the selection of the friction angle, due to (Figure 7.10 – refer to discussion in Chapter 6 - Cho

et al., 2006; Santamarina and Shin, 2009). Stress path dependent friction angle (intermediate stress and b-value): Figure 7.10 shows differences in friction angle ϕ when the flow at yield is 1D→2D as in the external angle of repose in a cone, which is similar to AC-loading ($\phi_{AC} = \phi_{EXT}$), and when flow is 2D→1D as in the internal angle of repose in a conical void, which is similar to LC-loading ($\phi_{AE} = \phi_{INT}$). Also, the friction anisotropy is observed in triaxial axial extension AE and compression cases AC for both sands and clays (Mayne and Holtz, 1985):

- Different points beneath a footing experience different flow conditions (b-value).
- Confinement-dependent dilation.
- Post-peak strain softening leads to progressive failure (see for example Rowe and Peaker, 1965) and the effective friction angle decreases as failure progresses.

Implications on bearing capacity can be striking, as can be inferred by comparing bearing capacity coefficients for ϕ_{AC} and for $\phi_{AE} \approx 1.5\phi_{AC}$, say 30° and 45° respectively (Figure 7.10).

Initial k_o condition. The value of k0 plays a secondary role in the estimation of footing settlements, but it does affect displacement fields induced by soft zone formation. The initial value of k_o is unknown. If the sediment is overconsolidated by preloading then k_o = 1.0 is an adequate first estimate for this formation (say, OCR~4 - Mayne and Kulhawy, 1982). If the formation is lightly cemented, k_o could vary in a wide range depending on the stress-cementation history. Finally, the value of k_o in layers that have experienced dissolution could have decreased to the minimum value of $k_o = k_a$ at some point in the formation history (Shin and Santamarina, 2009). A value of $k_o = 1.0$ is adopted for the simulation.

Design parameters – Preliminary values. Material properties for elasto-plastic and Modified Cam Clay models were selected following guidelines identified above and the

selected parameters are summarized in Table 7.1. The maximum soil stiffness E_{max} is determined from small-strain geophysical field data.

The stiffening effect of cementation is inherently taken into consideration when stiffness is computed from shear wave velocity. However, no cohesion or dilation is considered for the strength of any of the layers: this is the "worst-case condition" (from a material parameters point of view) as very advanced softening of soft zones can be modeled without forming cavities underneath cemented layers. The presence of cemented layers would "hide" cavities and soft zones from the shallower layers.

7.3 Case history

Defense Waste Processing Facility. This structure was constructed on the S-Area of the SRS Site (SRNS, 2011). The building was supported on a mat foundation (~110 m long, ~38 m wide, and ~1.5 m thick). The average distributed design load is 220 kPa. A settlement monitoring program was implemented from the beginning of the excavation of the building site. It was divided into four stages:

- Stage A: excavation
- Stage B: construction of the mat foundation
- Stage C: structural and other loads
- Stage D: post-completion

Figure 7.11 shows the major defense waste processing facility buildings on the left. The figure on the right shows the geometry of the mat foundation and the location of monitoring monuments for building 221-S; the loading history is shown in Figure 7.12. Figure 7.13 shows settlement-vs-time data gathered midway along the footing. The loading and settlement histories are combined into settlement-load plots in Figure 7.14: results show a relatively linear trend. This suggests the possible estimation of an equivalent global stiffness using the elastic solution: indeed, data replotted in Figure 7.15

suggest a first order estimate of the global stiffness is about E = 150 MPa for settlements greater than about 0.025 m.

Preliminary analysis. A 2D analysis conducted using Modified Cam Clay and verified with standard 1D consolidation using the same parameters show that (Figure 7.16):

- the 2D and 1D analyses conducted assuming OC conditions provide almost identical results
- in order to match the measured surface settlements, the selected consolidation parameters are in the lower end of values reported from laboratory studies (as noted in reference to Figure 7.9).
- for the given geometry (B=34 m, layered stratigraphy, most compressible layers in upper <50 m), the 1D analysis provides an excellent approximation to the 2D results.
- as a corollary, parameter selection is much more important than the decision to capture this case history using a 1D or 2D representation.

The 6cm mean settlement implies an "average strain" lower than $< 10^{-3}$ within the depth of influence of the mat foundation. This relatively small strain requires high quality specimens and detailed test procedures to minimize the impact of core-chamber gap and seating effects on thin oedometer specimens. An alternative approach based on field data is explored next.

Numerical simulation. The commercial software ABAQUS is used for the simulations. The medium is discretized into plane-strain, eight-node biquadratic reduced integration elements. The lower boundary and lateral boundaries are located far from the footing to minimize boundary effects (model: 200 m high and 300 m wide - due to symmetry, the effective width is 600 m). Vertical displacement is allowed on side boundaries, the bottom boundary is pinned, and the top surface is free (Figure 7.17). Five distinct strata

are modeled. A surcharge load of q_0 = 10kPa is applied everywhere to reflect a nominal burial depth in standard construction practice.

Lateral boundary effects were assessed for the selected domain using cases that include various soft zone-loading histories. Results in Figure 7.18 confirm that there are no boundary effects in these simulations: the far-field surface settlement is almost null in all cases and the geostatic horizontal stresses against far field zero-lateral strain boundaries remain constant through loading-dissolution histories.

7.4 Model calibration by back analysis

The alternative approach selected for back analysis is based on a secant formulation using the elastic-perfectly plastic Drucker-Prager material model to represent all strata. This is a simple and robust approach, in line with Ockham's criterion.

Load-settlement results are shown in Figure 7.19. The predicted failure load is about 10 times higher than the applied load (in agreement with the small strains anticipated above).

Stiffness reduction. The basic hyperbolic model (Kondner, 1963; Duncan and Chang, 1970) is adopted to evaluate the reduction of stiffness with strain in a robust manner (Figure 7.20). The secant stiffness E_{sec} that corresponds to strain ε is related to the maximum stiffness E_{max} estimated from in situ measurements of wave propagation,

$$\Pi = \frac{E_{sec}}{E_{max}} = \frac{1}{1 + \frac{\varepsilon}{\varepsilon_{ref}}} \qquad \textit{Modulus reduction factor} \qquad (7.1)$$

where the reference strain $\varepsilon_{ref} = \sigma_{ult} / E_{max}$ is computed using the Coulomb frictional strength at the corresponding state of stress σ_{ult} and the value of E_{max}.

Model calibration. The algorithm implements successive forward simulations where the modulus of each layer is reduced as a function of the strain mobilized in the layer, until

the computed settlement matches the measured settlement. The procedure is as follows (Figure 7.21):

1. Model all layers using the elastic-perfectly plastic Drucker-Prager model in a secant formulation.
2. Determine the E_{max} for each layer from small-strain geophysical field data.
3. Run the FEM and estimate strains in each element ε_{est}.
4. Reduce the stiffness in each element according to the strain level using the hyperbolic formulation.
5. Repeat steps 3 and 4 until subsurface strains convergence in subsequent iterations (example shown in Figure 7.22).
6. Compare the predicted settlement to measured surface settlements – If needed, adjust initial soil parameters as needed, but within the range of parameter uncertainty.
7. Repeat steps 3-to-6.

Final modulus reduction values computed for the SRS case history range from a factor of $\Pi = 7$ in the shallowest layers (highest strains) to almost no reduction at depths $z \sim B >$ 35 m. The reduced modulus compares well with the back-calculated global modulus (Figure 7.15 and Table 7.2).

Foundation stiffness. The mat foundation and the superstructure could be modeled in finite elements as well. To explore the effect of the mat-and-structure stiffness, we simulated and compared the two end-members: perfectly flexible (i.e., stress-controlled) and perfectly rigid (i.e., displacement controlled). Results in Figure 7.23 show limited effect of structural stiffness, with slight preference to rigid mat response (Stage C: structural and other loading; Stage D: post-completion). Displacement fields in Figure 7.24 and Figure 7.25 show the controlling effect of the shallower layers on surface settlement.

7.5 Possible settlements due to cavities and seismic action

The calibrated subsurface model, including selected material parameters coupled with strain-dependent stiffness reduction, is taken as the initial condition (in-situ stresses and secant modulus of soil layers) to compute additional settlements due to the presence/formation of cavities and for seismic loading.

Parametric studies. The carbonate rich sediments found in the lower Dry Branch and the Santee formation strata may experience dissolution. Three sets of hypothetical cavities are simulated to quantify the impact of dissolution features on the shallow mat foundation (Figure 7.26 - These cases are inspired by similar conditions encountered at the Vogtle excavation nearby – At the SRS, soft zones are mainly encountered in the Santee formation at a depth ≈ 40~48 m). Two possible formation histories are considered: stress relaxation-before-structure and structure-before- stress relaxation.

Seismic action is added after soft zone formation in all cases. At the SRS, the horizontal component of the peak ground acceleration a_{max} on rock is between 0.06-0.09g (7%-75 year) and 0.09-0.12g (2%-50yr - See http://earthquake.usgs.gov/hazards/). Quasi-static analysis is adequate for these a_{max} values. Seismic wave propagation will induce a strain level that can be estimated as $\gamma = a_{max} / 2\pi \cdot Vs \cdot f$. For example, $\gamma \approx 5x10^{-4}$ for a_{max} = 0.1g, Vs = 300 m/s and f = 1Hz. Strain levels are approximately linearly proportional to a_{max} within this range. These strain range is similar to the expected threshold strain for cementation breakage in this material. However, cementation breakage leads to a very dilative blocky structure, where blocks are composed of cemented grains. Therefore, higher accelerations do not necessarily imply risk of excess pore pressure generation. In summary, seismic action is modeled as a quasi-static horizontal load applied onto the mat foundation. The selected horizontal load is 10% of the vertical load.

The numerical methodology is summarized in Table 7.3. Soft zone formation is simulated with different levels of internal stress reduction in order to capture different degrees of dissolution.

Results. Computed settlements for complete histories are shown in Figure 7.27. The main observations follow:

- The structure-induced settlement is the largest component [OB or AC paths]; the formation of cavities or soft zones may increase settlements by less than 10-20% [OA or BC paths]. The validity of this observation is limited to hypothetical geometries.
- Soft zone formation before the structure [OACD paths] produces slightly larger settlements than soft zone formation after the structural load [OBCD paths]. Thus, differences in formation history can be disregarded for all practical purposes at the SRS.
- Seismic loading the structure (ah = 0.1g) sitting on top of the sediment with cavities will cause negligible additional settlement (less than 5% of the total settlement due to the static load in all 24 cases).
- On the bases of these results, more complex seismic models that take into consideration inertial effects are not necessary at this point and for the purposes of this analysis. Furthermore, other consequences of seismic action such as liquefaction are unlikely given the measured penetration resistance and shear wave velocity profiles everywhere in the sediment except in the localized soft zones.

7.6 Conclusions

Back analysis faces inherent difficulties with convergence and non-uniqueness of the solution. These are exacerbated by the stress-dependent, nonlinear soil behavior,

spatial variability, and typically limited information available in most field cases. The approach developed and implemented in this study was guided by Ockham's criterion, involved a simple secant formulation using a robust elasto-plastic numerical model and was anchored on credible field measured parameters.

The "SRS subsurface model" was calibrated through the back-analysis of settlement data gathered during the construction of the Defense Waste Processing Facility at SRS. Emphasis was placed on small-strain geophysical field measurements.

Results for this facility at SRS show that structure-induced settlements overwhelm all other effects. The formation of cavities or soft zones either before or after the building load may cause an increase in settlement less than 10-20% (for the simulated conditions). Seismic loading the structure (a_h = 0.1g) after soft zone formation adds an additional settlement smaller than 5% of the settlement induced by the static load (for the simulated conditions).

Preliminary analyses conducted with compressibility parameters gathered in consolidation tests overpredicted settlements possibly due to sampling effects and procedural difficulties (e.g., core-ring gap, cap seating effects magnified by thin specimens).

For the given geometry (B = 34 m, layered stratigraphy, most compressible layers in upper < 50 m), the 1D analysis provides an excellent first order estimate. Furthermore, parameter selection is much more important than the choice to capture this case history using a 1D or 2D representation.

It highlights that no cohesion was considered in any of the layers. However, open pipes and tensile fractures observed at the Vogtle excavation suggest cementation in the host layer and/or the layer above. The addition of cementation to the frictional strength of overlying layers should dramatically diminish the impact of soft zones on shallow foundations.

Table 7.1. Selected material properties

Parameter	**Source**	**Upland Unit**	**Tobacco Road**	**Dry Branch**	**Santee**	**Warley Hill**
Depth [m]	*Shannon and Wilson (2007)*	0 - 8	8 -13	13-40	40-48	48-200
Effective unit weight γ [kN/m^3]		20	10	10	10	10
Isotropic compression index λ	*min < back-calculated < max*	0.01	0.02	0.03	0.04	0.005
Void ratio at 1kPa e_{1kPa}	*e1kPa = 7.83λ + 0.48 (Chapter 2)*	0.56	0.63	0.71	0.78	0.52
Isotropic recompression index κ	*Assumed (λ/10)*	0.001	0.002	0.003	0.004	0.0005
OCR	*Assumed*	4	4	4	4	4
Shear velocity V_s [m/s]	*Shannon and Wilson (2007)*	350	300	300	250	500
Small-strain Poisson's ratio υ	*Assumed*	0.15	0.15	0.15	0.15	0.15
Young's modulus E_{max} [MPa]	*from Vs*	*574*	*422*	*422*	*293*	*1173*
Drained Poisson's ratio υ	*Assumed*	0.2	0.2	0.2	0.2	0.2
Friction ϕ [^{o}]	*Shannon and Wilson (2007)*	37	35	34	24	43
MCC strength M (for AC)	*from ϕ*	1.51	1.42	1.38	0.94	1.77
Cohesion MC	*Assumed*	0	0	0	0	0
Dilation Ψ [^{o}]	*Assumed*	0	0	0	0	0
Earth pressure k_0	*Assumed*	1.0	1.0	1.0	1.0	1.0

Table 7.2. Selected material properties

Parameter	**Source**	**Upland Unit**	**Tobacco Road**	**Dry Branch**	**Santee**	**Warley Hill**
Depth [m]		0 - 8	8 -13	13-40	40-48	48-200
Effective unit weight γ [kN/m^3]		20	10	10	10	10
Isotropic compression index λ	min < back-calculated < max	0.01	0.02	0.03	0.04	0.005
Void ratio at 1kPa e_{1kPa}	$e_{1kPa} = 7.83\,\lambda + 0.48$	0.56	0.63	0.71	0.78	0.52
Isotropic recompression index κ	Assumed (λ/10)	0.001	0.002	0.003	0.004	0.0005
OCR	Assumed	4	4	4	4	4
Shear velocity V_s [m/s]	Shannon and Wilson (2007)	350	300	300	250	500
Small-strain Poisson's ratio υ	Assumed	0.15	0.15	0.15	0.15	0.15
Young's modulus E_{max} [MPa]	from Vs	*574*	*422*	*422*	*293*	*1173*
Modulus reduction factor II	back-calculated	*6.7*	*2.4*	*2.0*	*1.4*	*1.0*
Effective modulus E [MPa]	from back-analysis	*85*	*178*	*213*	*206*	*1142*
Drained Poisson's ratio υ	Assumed	0.2	0.2	0.2	0.2	0.2
Friction ϕ [^{o}]	Shannon and Wilson (2007)	37	35	34	24	43
MCC strength M (for AC)	from ϕ	1.51	1.42	1.38	0.94	1.77
Cohesion MC	Assumed	0	0	0	0	0
Dilation Ψ [^{o}]	Assumed	0	0	0	0	0
Earth pressure k_0	Assumed	1.0	1.0	1.0	1.0	1.0

Table 7.3. Soft zone formation histories (Cases 1, 2, and 3 refer to soft zone size and number sketched in Figure 7.26)

	Stress Relaxation Before Load	**Stress Relaxation After Load**
Case 1	1) Form soft zone until specified ISR 2) Load footing to q_0 and q_1 3) Apply QS load over the footing 4) Repeat for ISR = 10,30,60,90	1) Load footing to q_0 and q_1 2) Form soft zone 3) Reduce the internal stress until specified ISR 4) Apply QS load over the footing 5) Repeat for ISR = 10,30,60,90
Case 2		
Case 3		

Surcharge: q_0 = 10 kPa

Building load: q = 220 kPa

QS horizontal load: QS = 22 kPa

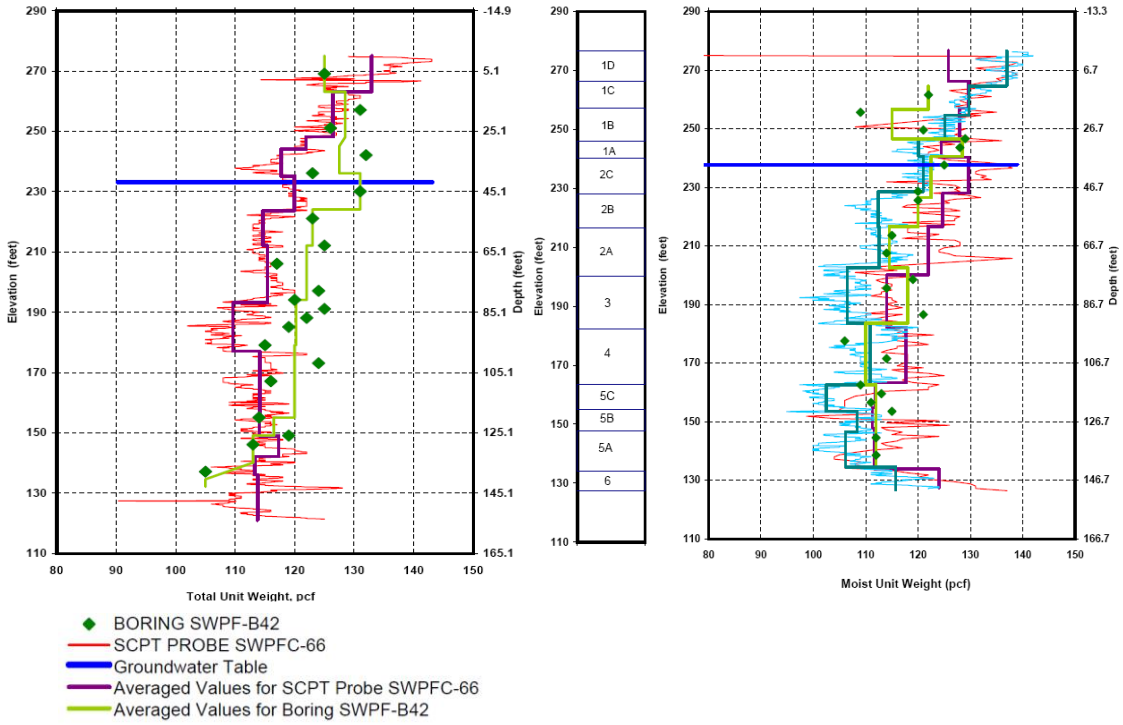

Figure 7.1. Unit weight (Shannon and Wilson, 2007)

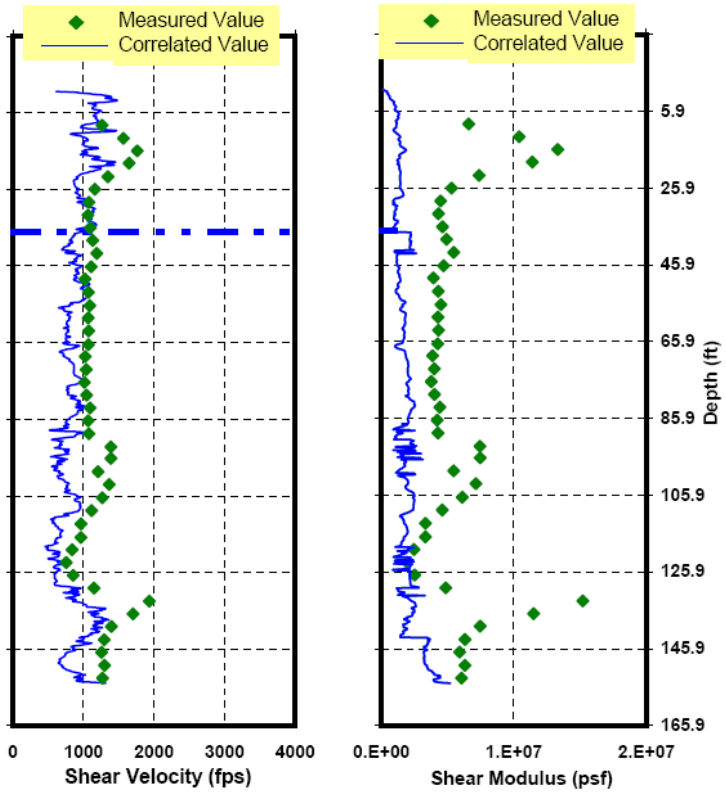

Figure 7.2. Stiffness-stress in situ (Shannon and Wilson, 2007)

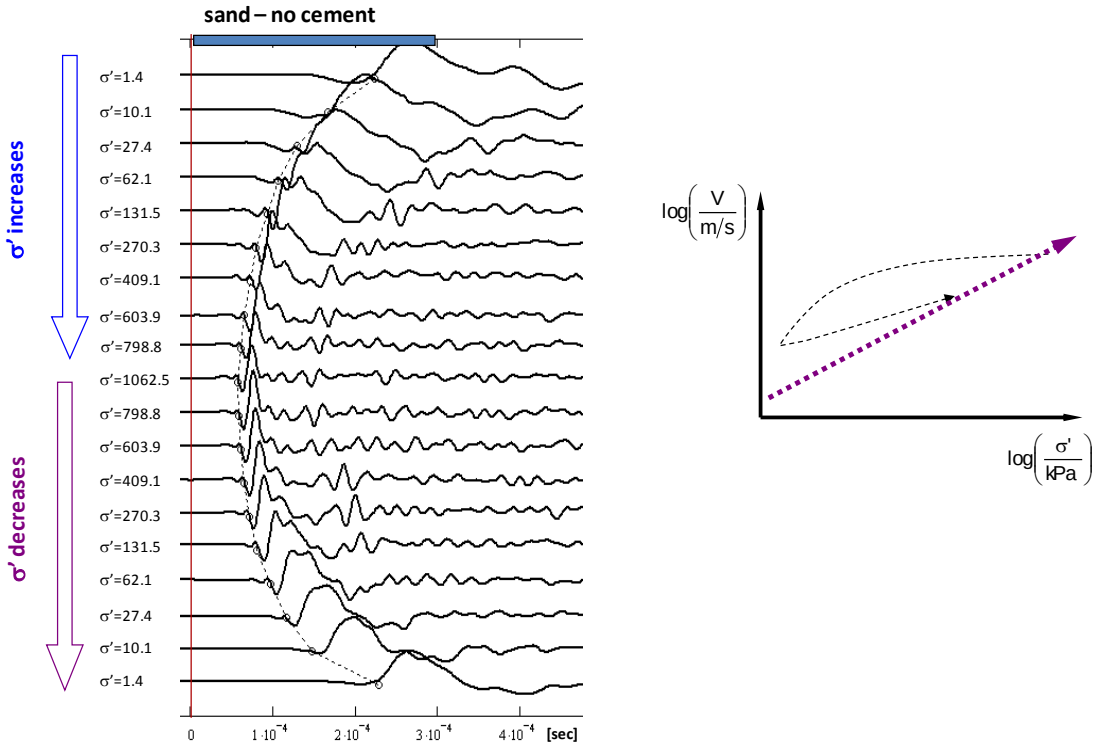

Figure 7.3. Stiffness-stress: uncemented soil (Yun and Santamarina, 2005)

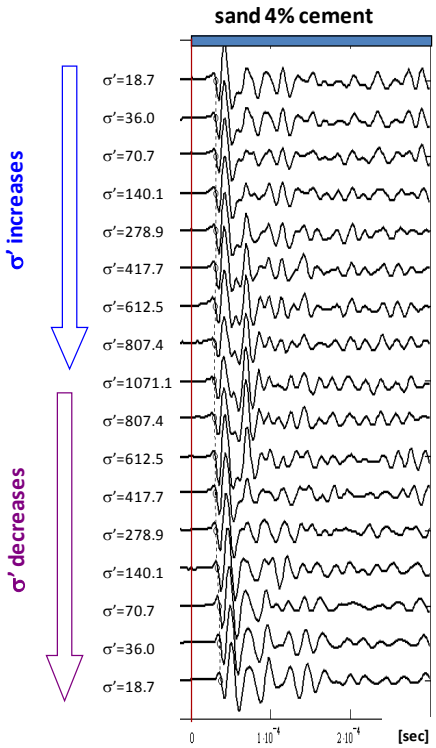

Figure 7.4. Stiffness-stress: cemented soil (Yun and Santamarina, 2005)

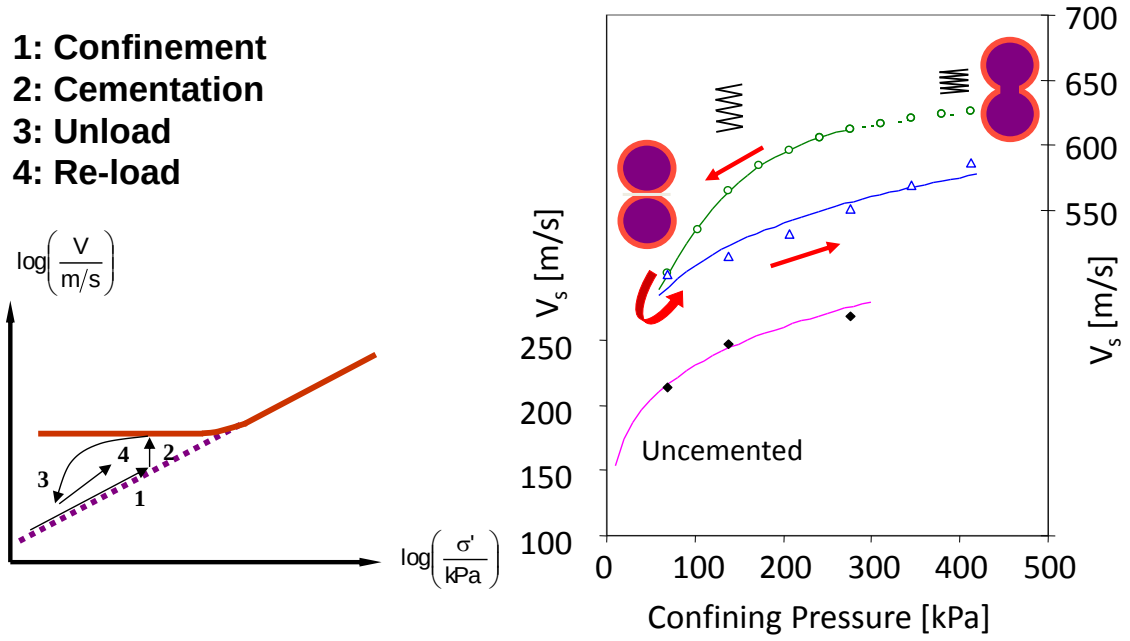

Figure 7.5. Sampling effect: cemented sandy soils (Fernandez and Santamarina, 2001)

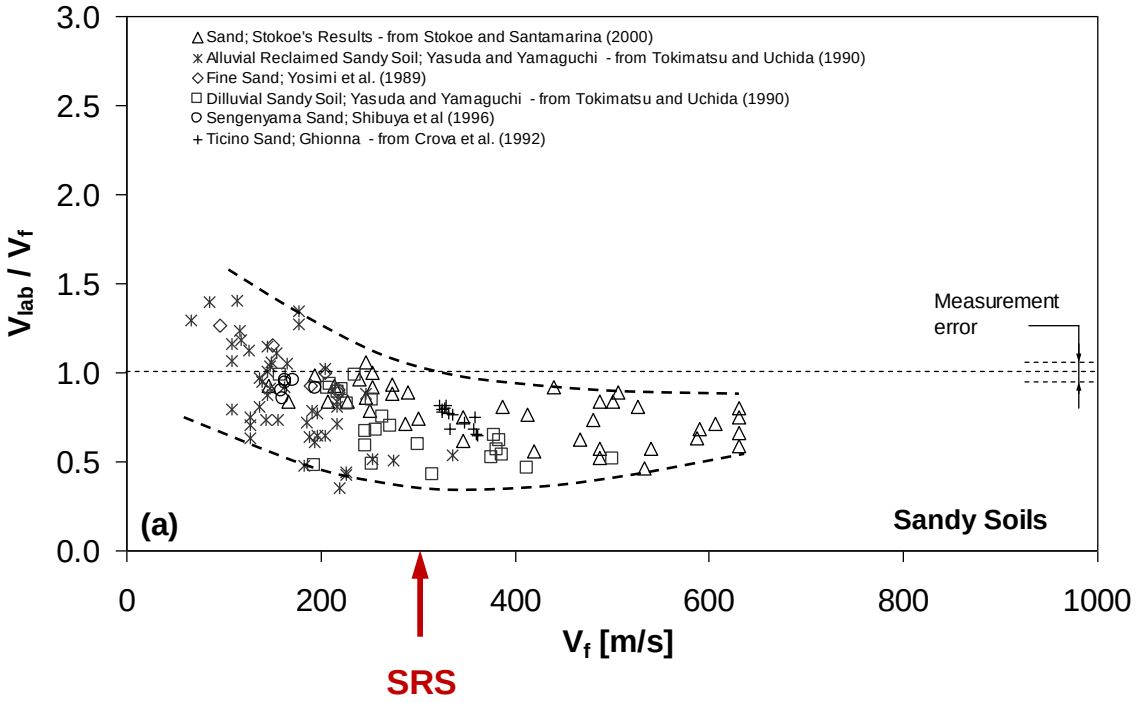

Figure 7.6. Sampling effect: sandy soils (Rinaldi and Santamarina, 2008)

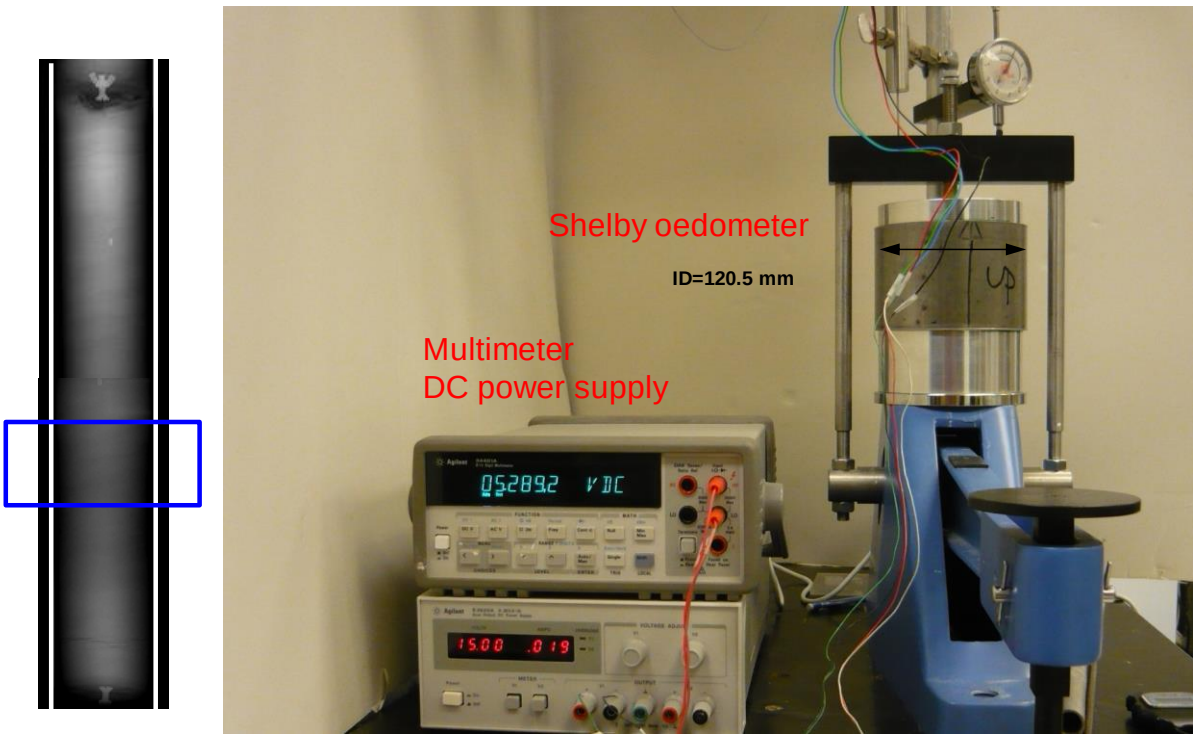

Figure 7.7. "In-Shelby" consolidation test

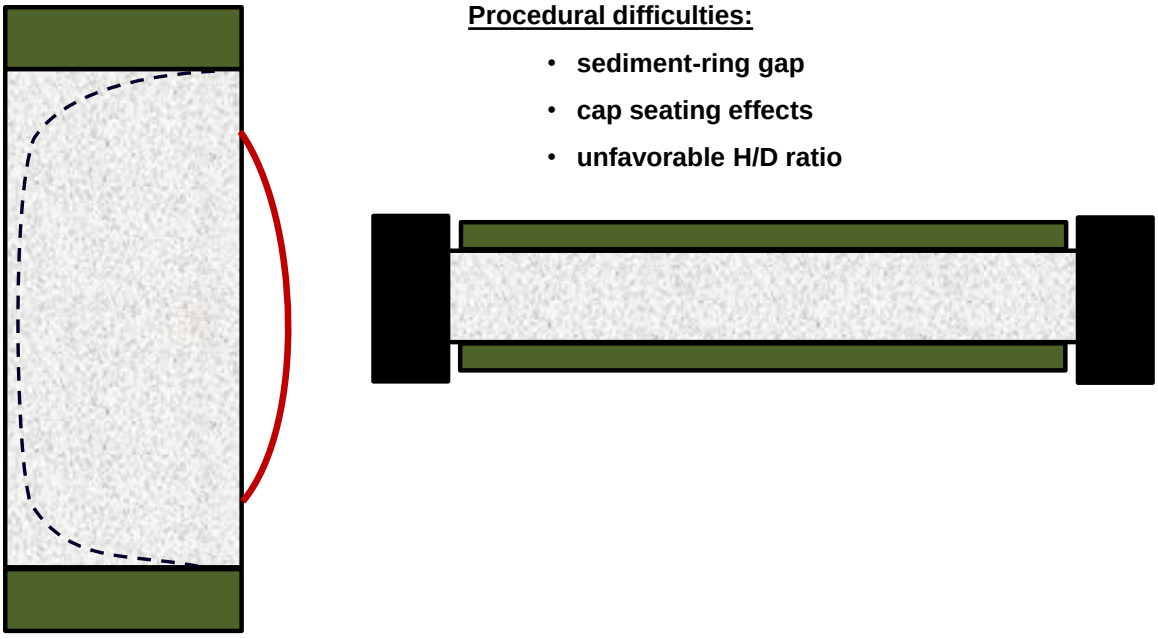

Figure 7.8. Cap seating effects

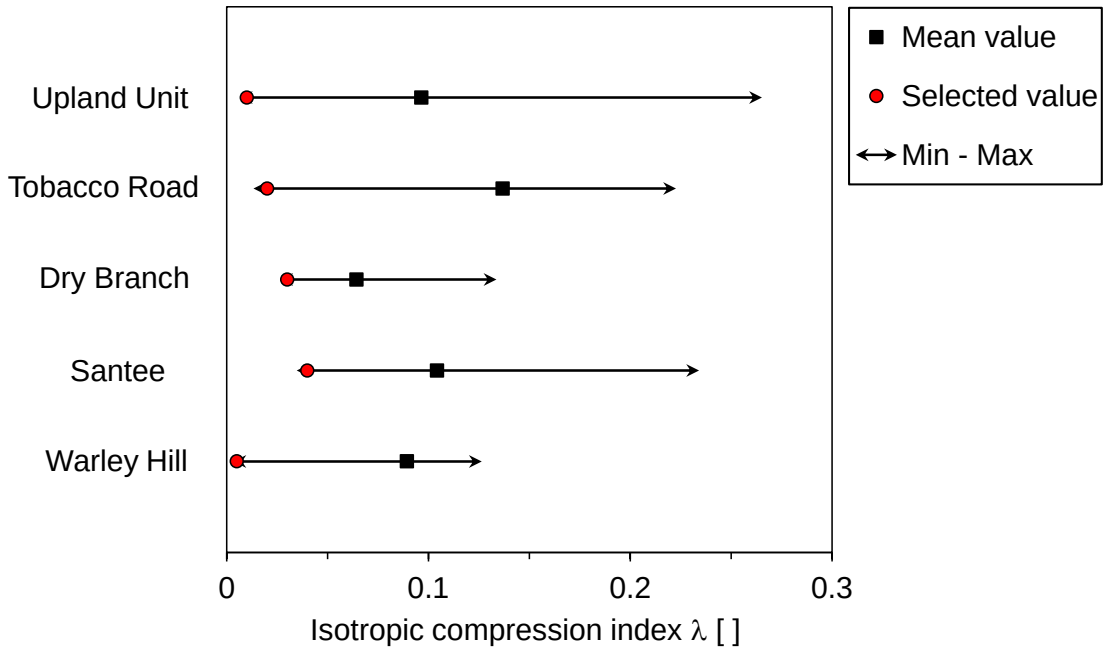

Figure 7.9. Ranges and mean values for isotropic compression index (red points selected for preliminary back analysis in Figure 7.16. Data: Burns and Roe Enterprises, 2001; Shannon and Wilson, 2007).

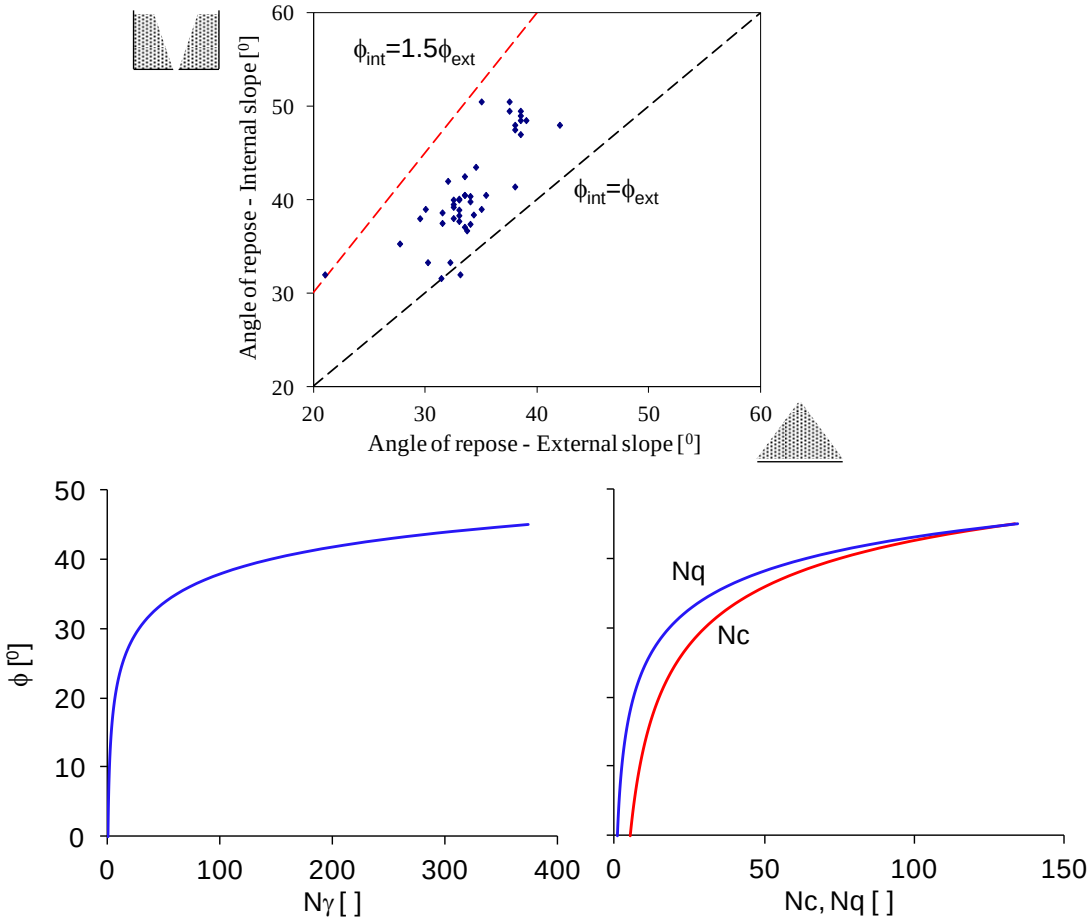

Figure 7.10. Uncertainty of the soil friction and its implication on bearing capacity

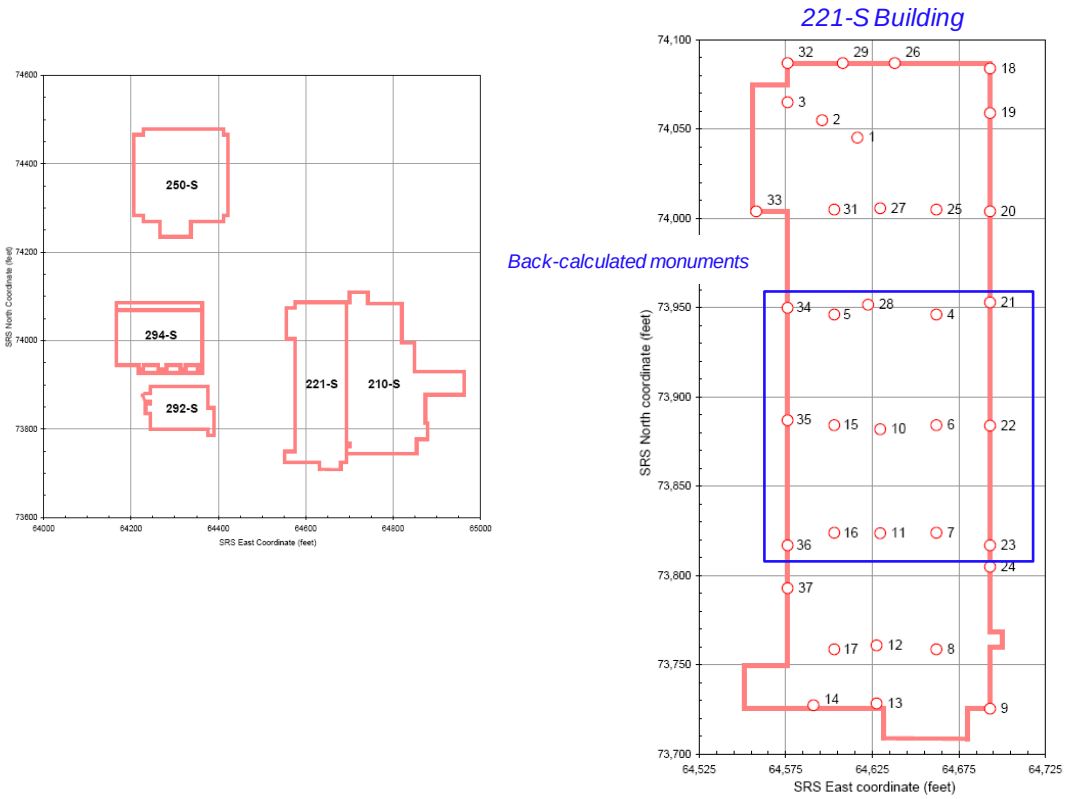

Figure 7.11. Mat foundation - Monitoring stations (SRNS, 2011)

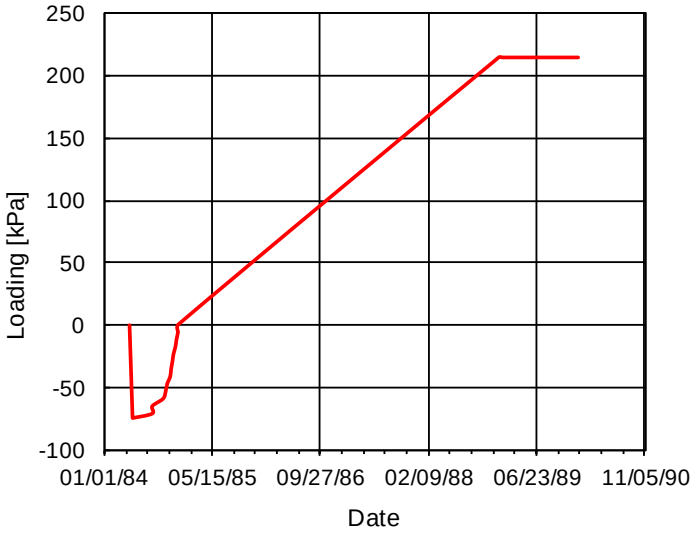

Figure 7.12. Loading history (SRNS, 2011)

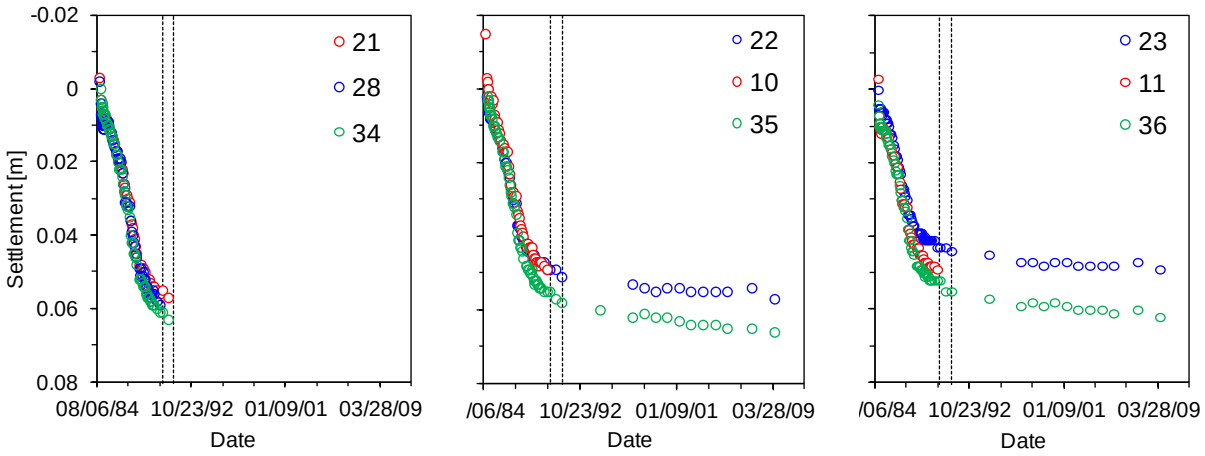

Figure 7.13. Settlement-vs-time (SRNS, 2011)

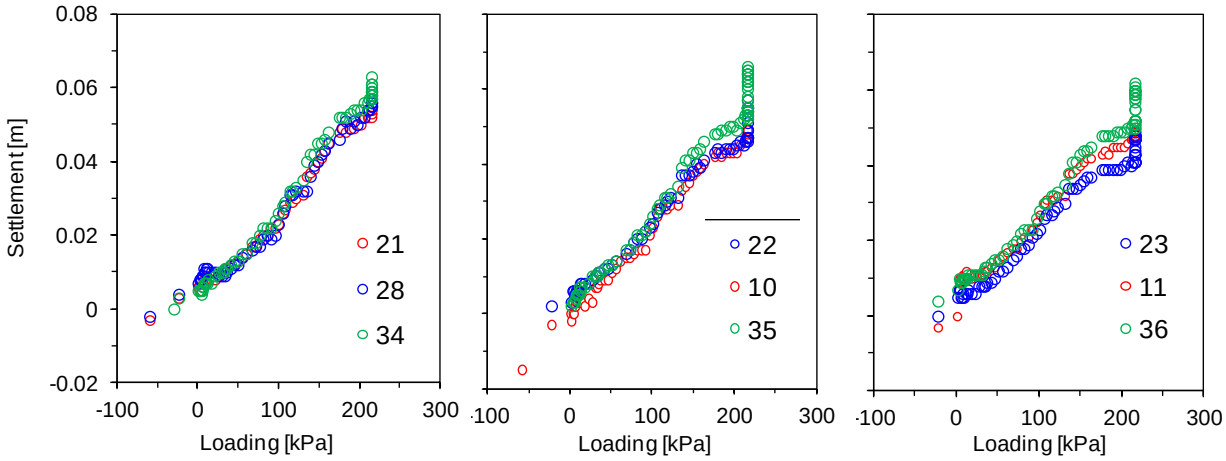

Figure 7.14. Settlement-vs-load (SRNS, 2011)

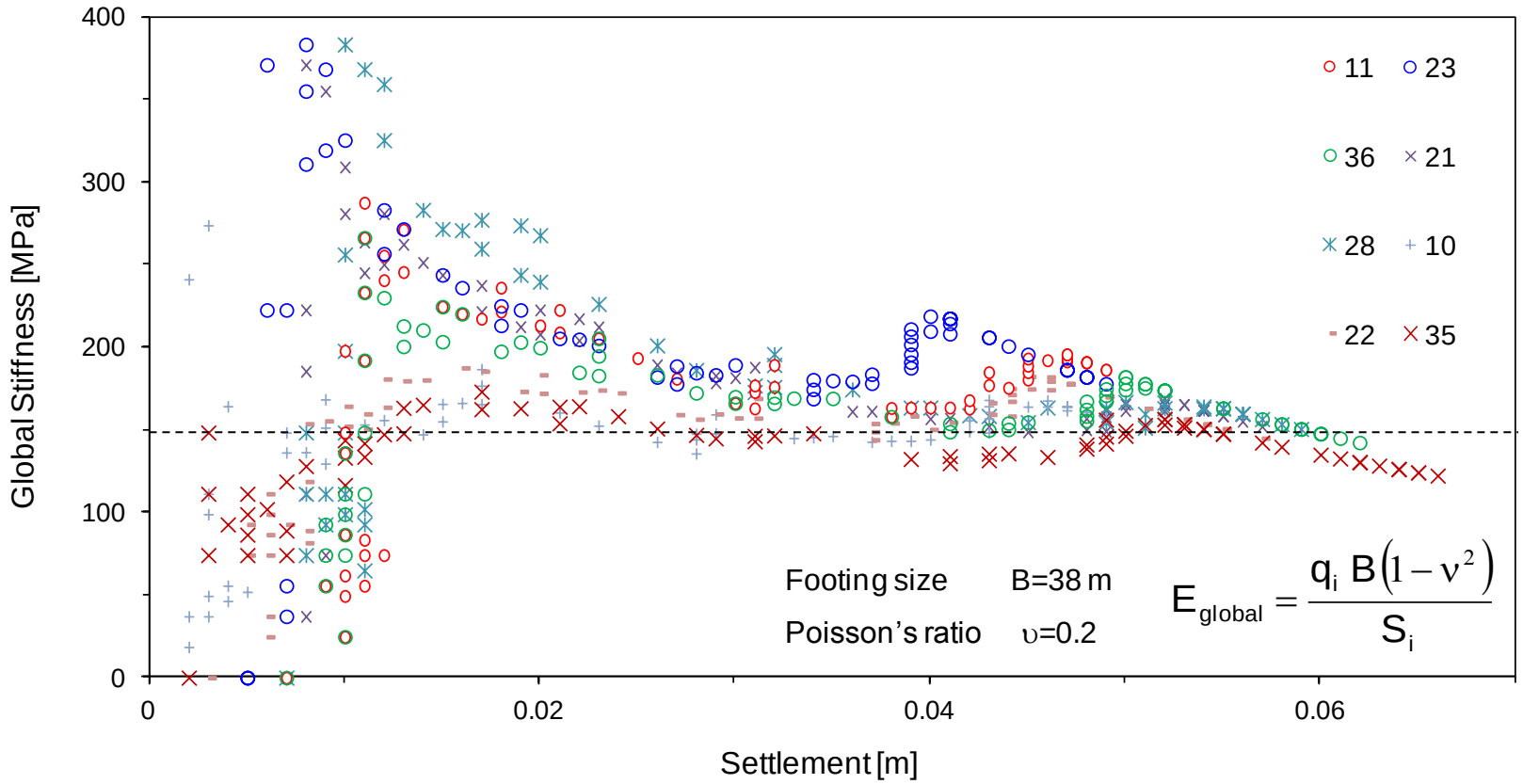

Figure 7.15. Back-calculated global modulus (Dotted line indicates the first order estimate of the global stiffness for settlements greater than about 0.025 m).

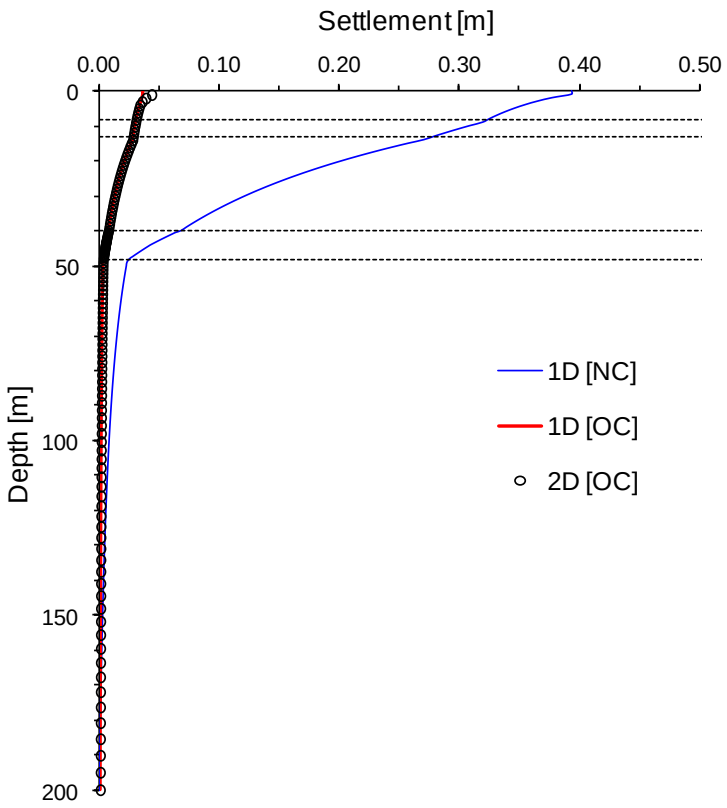

Figure 7.16. Settlement calculation - Oedometer data

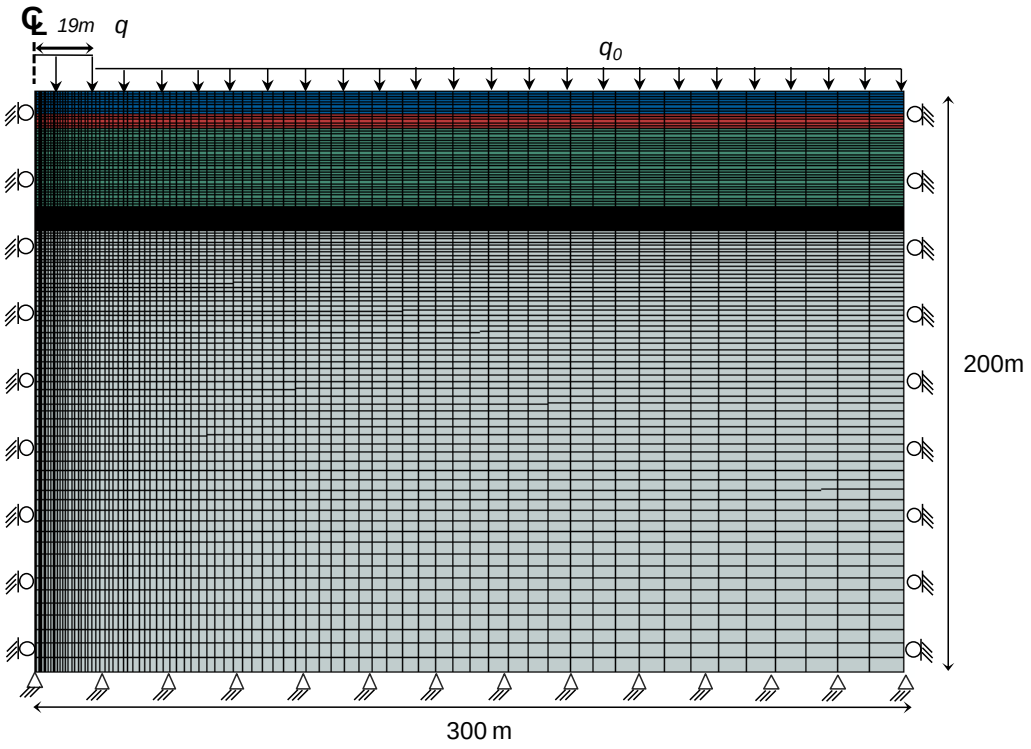

Surcharge: q_0=10 kPa

Building load: q=220 kPa

Number of elements: 10000

Type: 8-node biquadratic elements

Condition: plane strain quadrilateral

Figure 7.17. Geometry - Boundary conditions

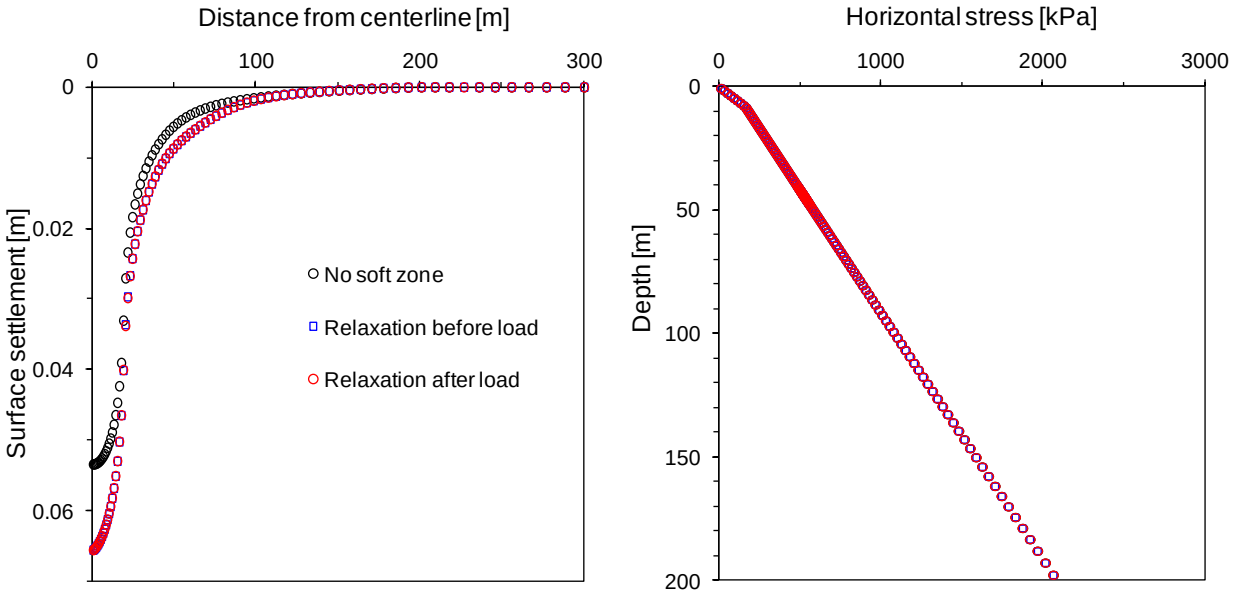

Figure 7.18. Boundary effect (Case 3; ISR ≈ 0.95)

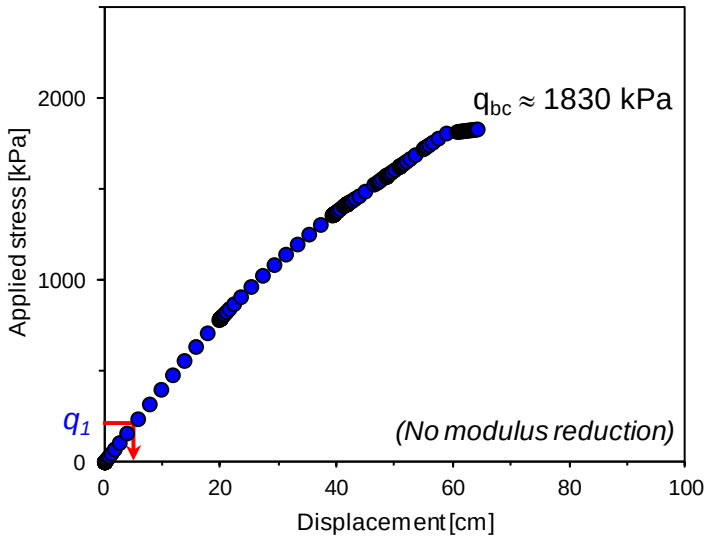

Figure 7.19. Load-displacement (No soft zone)

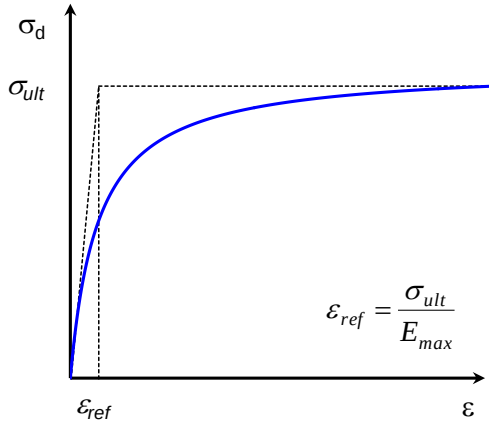

$$\sigma_d = \frac{\varepsilon}{a + b\varepsilon} = \frac{\varepsilon}{\frac{1}{E_{max}} + \frac{\varepsilon}{\sigma_{ult}}} = \frac{E_{max}\varepsilon}{1 + \frac{\varepsilon}{\varepsilon_{ref}}}$$

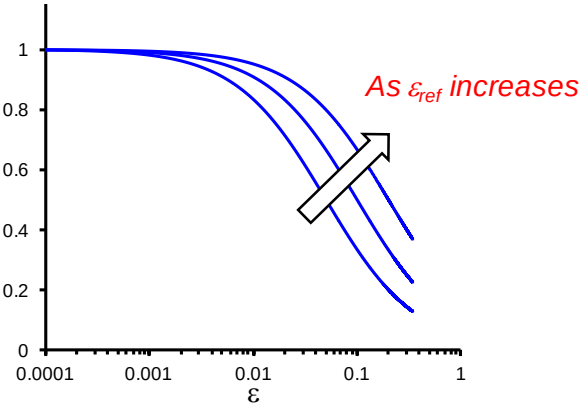

Secant stiffness:

$$\Pi = \frac{E_{sec}}{E_{max}} = \frac{1}{1 + \frac{\varepsilon}{\varepsilon_{ref}}}$$

Figure 7.20. Modulus reduction - Hyperbolic model

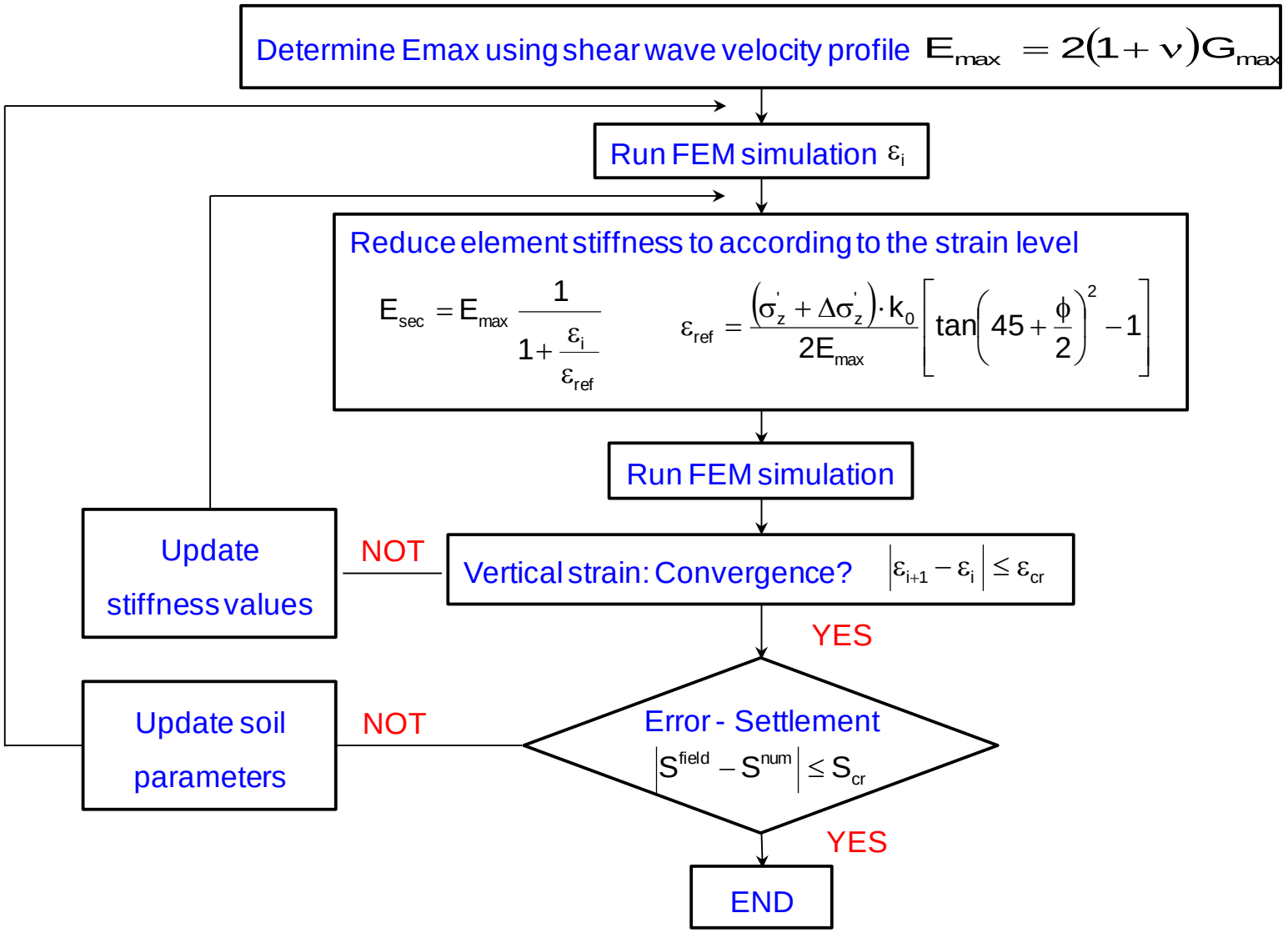

Figure 7.21. Back analysis and model calibration

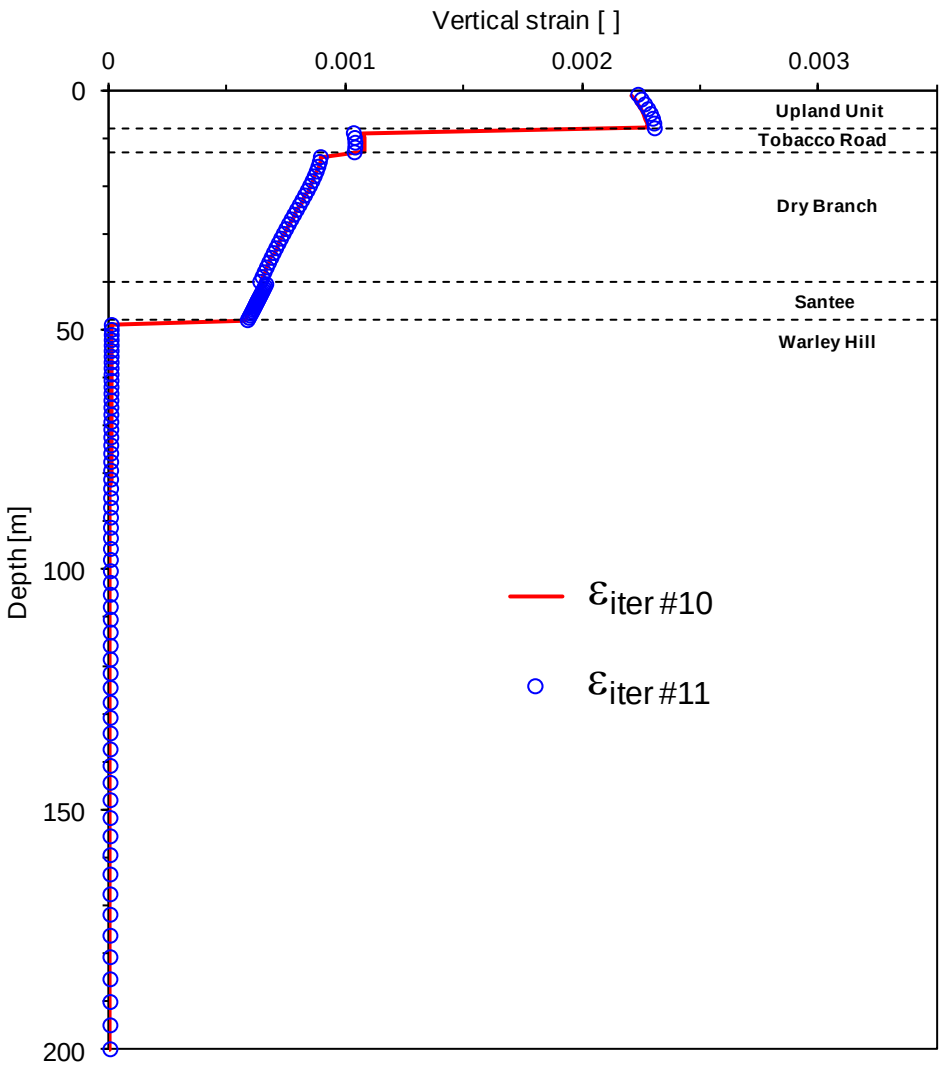

Figure 7.22. Convergence: $\varepsilon_{iter\ i}$ vs. $\varepsilon_{iter\ i+1}$

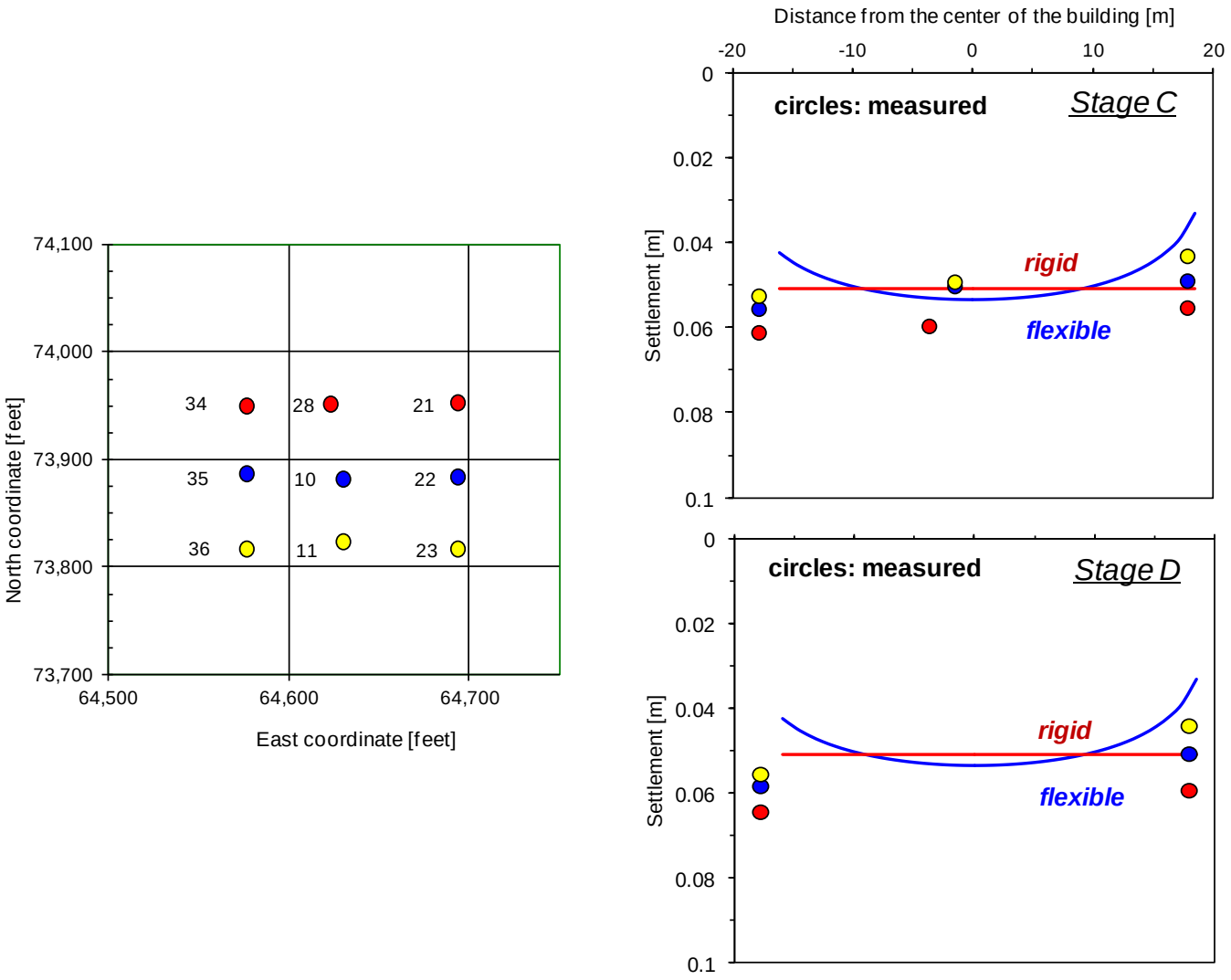

Figure 7.23. Measured vs. predicted settlements

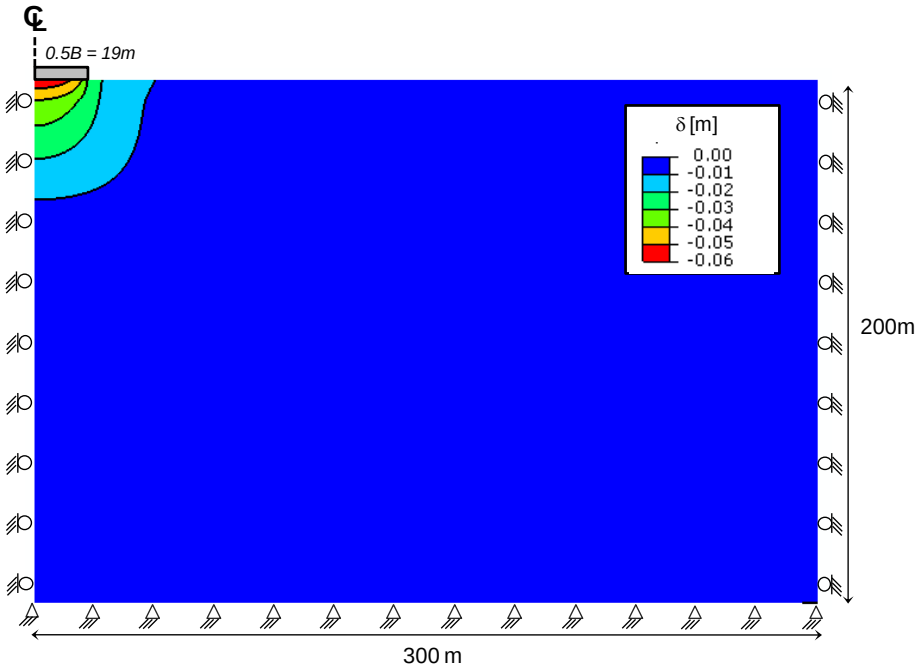

Figure 7.24. Displacement field - Building load (no soft zone); load applied in load-controlled mode (flexible footing)

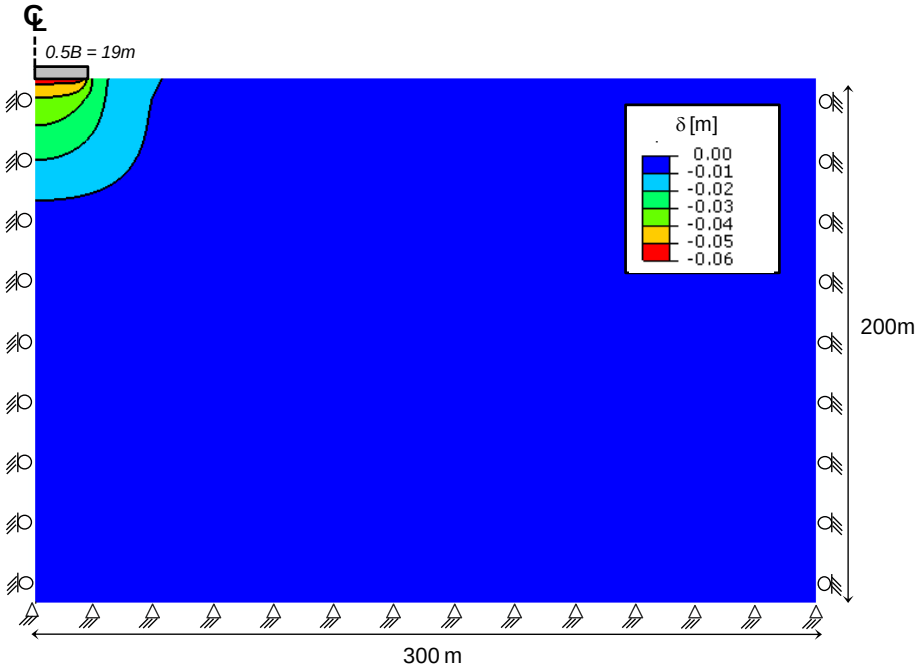

Figure 7.25. Displacement field - Building load (no soft zone); load applied in deformation-controlled mode (rigid footing).

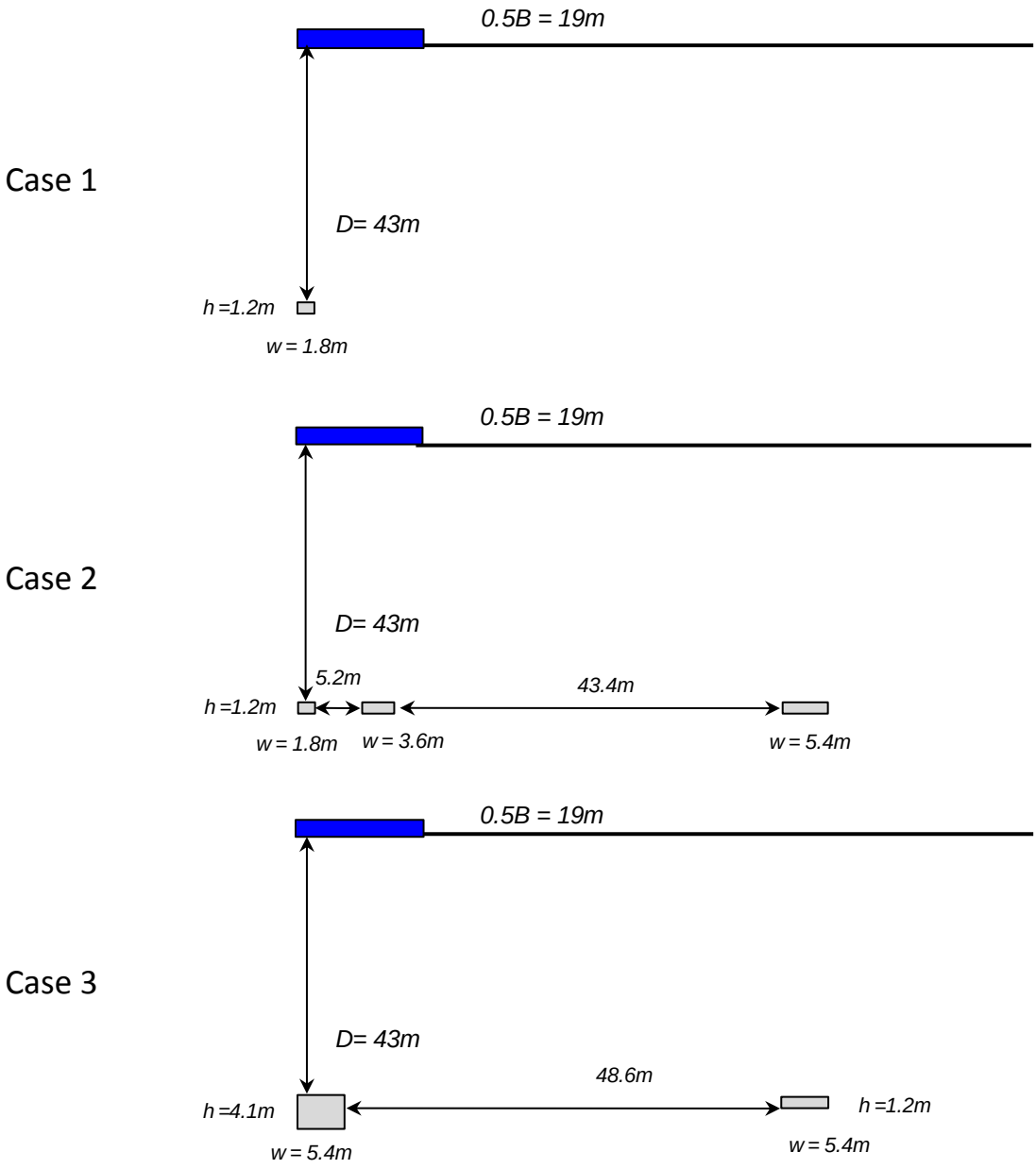

Figure 7.26. Hypothetical soft zones

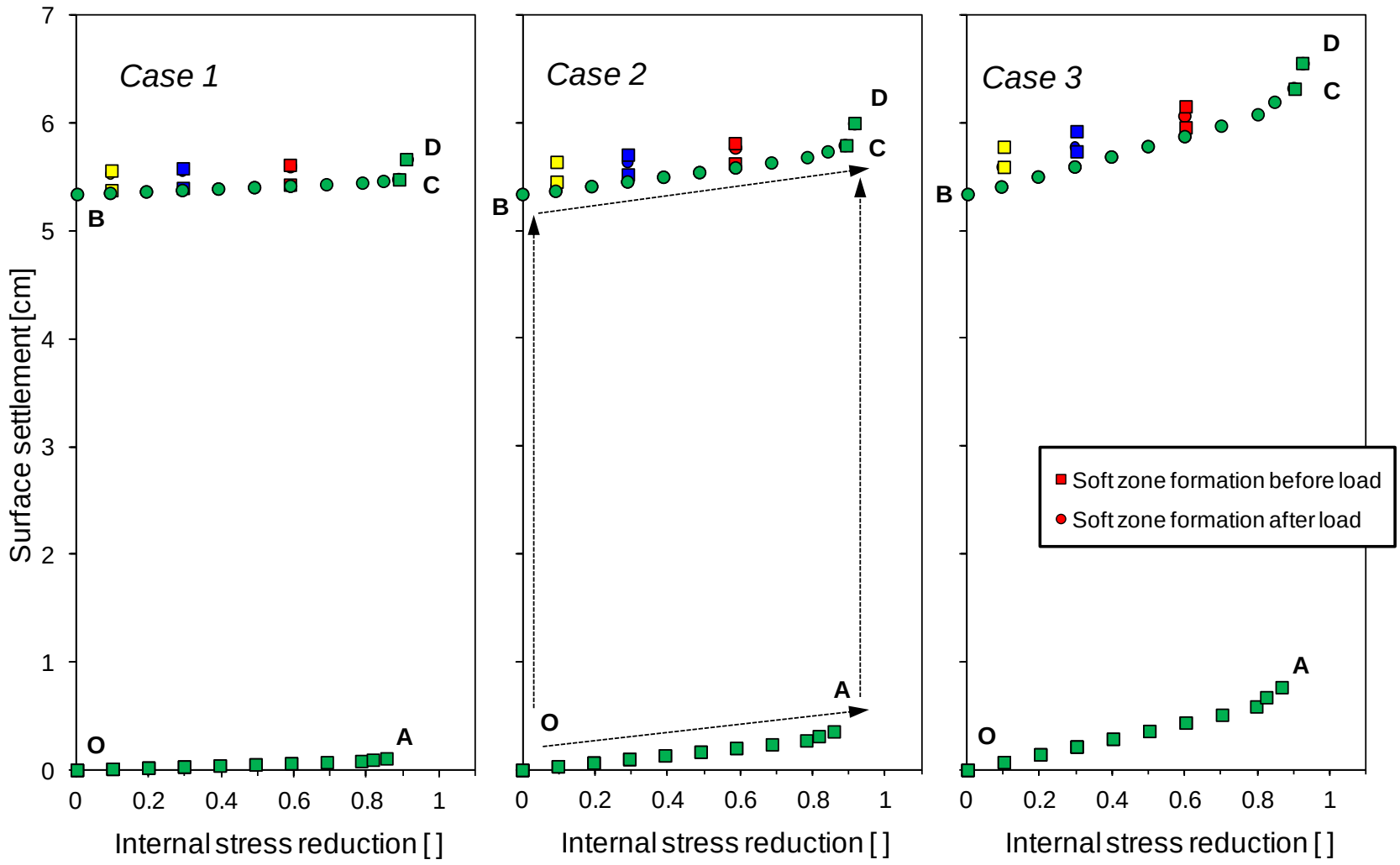

Figure 7.27. Settlement: Footing load, soft zone formation, and seismic load (z_0 = 43 m)

CHAPTER 8

HYPOTHETICAL CASES

8.1 Introduction – Field case and model

In this section, we utilize the soft zone formation module (developed and tested in Chapter 5) to conduct a comprehensive study of a hypothetical shallow foundation system suggested by the project leadership at SRS, using the calibrated SRS subsurface model (Chapter 7). Several soft zone topologies and formation histories are simulated to explore the impact of dissolution features on bearing capacity and settlement.

The plane-strain numerical simulation is performed using plane-strain, eight-node biquadratic reduced integration elements. The model geometry is: 200 m high and 300 m wide (i.e., due to symmetry, the effective width is 600 m). The subsurface consists of five distinct strata. All strata are modeled using the elastic perfectly plastic Drucker-Prager model. Material properties are tabulated in Table 8.1. No cohesion and zero dilation are assumed for all layers to define a conservative condition for the subsurface.

The very long structure is 120 m wide (plane strain condition - due to symmetry, a 60m wide footing is shown on Figure 8.1 – Figure 8.3, and will apply a load q = 380 kPa. A surcharge load q_0=20kPa is added everywhere on the free surface to reflect a nominal burial depth. The mat and structural stiffness have a secondary effect (refer to results in Chapter 7); hence, the mat is not explicitly modeled as a structural element, but as a rough and perfectly rigid footing. The numerical methodology is the same as the one summarized in the previous section.

8.2 Parametric studies – Results

Model calibration. The calibration procedure is revisited to reduce the modulus of each layer as a function of the strain mobilized in the layer (Figure 7.20 and Figure 7.21). The subsurface strains converge with subsequent iterations (Figure 8.4). Final modulus reduction values computed from the hypothetical cases show the range from a factor of $\Pi = 7$ in the shallowest layers (highest strains) to almost no reduction at depths $z > 48$ m. The vertical displacement is plotted in Figure 8.5.

Load at yield. Three sets of subsurface cavities are modeled; these cases are inspired on similar conditions encountered at the Vogtle excavation nearby (Figure 8.6). Different levels of internal stress reduction ISR capture different degrees of dissolution. Following simulations in previous Sections, the two formation histories considered in these simulations include cavities-before-loading and loading-before-stress relaxation.

Results in Figure 8.6 show yield, i.e., a break in the load-deformation curve during loading. The yield load decreases as the internal stress in cavities is reduced to emulate dissolution and soft zone formation. The yield load does not necessarily mean global bearing capacity failure in these hypothetical cases (the mat foundation is very large compared to the size of soft zone - $B/w < 120 / 5.4$). The structural load $q = 380$ kPa -shown on the figure- is relatively small in all cases. The yield load is normalized by the bearing capacity in the medium without cavities and plotted in Figure 8.7; the severity of Case 3 is readily seen.

Settlements. The stiffness reduction technique developed in Chapter 5 is applied to estimate settlements for these hypothetical cases, and to estimate additional settlements due to soft zone formation and seismic action. Simulations are run for stress relaxation-before-footing and footing-before-stress relaxation. Furthermore, footing load is imposed

at different degrees of internal stress reduction to reflect different degrees of dissolution. A total of 24 cases are summarized in Figure 8.8. All cases include a final stage when quasi-static horizontal load is added to simulate seismic action (a_h = 0.1g – refer to discussion and justification in previous section). Results resemble those obtained in the previous section for the case history. Larger settlements reflect the larger foundation size and higher load (Figure 8.8.). It can be observed that:

- The structure-induced settlement is the largest component [OB or AC paths]. In the absence of cavities, the structural load produces a settlement of about 12 cm (B points).
- The formation of cavities or soft zones may increase settlements by as much as 20% in the very severe Case 3 [OA or BC paths]. The validity of this observation is limited to hypothetical geometries.
- Soft zone formation before the structure [OACD paths] produces slightly larger settlements than soft zone formation after the structural load [OBCD paths], in agreement with conclusions in previous sections. However, the differences in formation history can be disregarded for all practical purposes at the hypothetical cases.
- Seismic loading of the structure (a_h = 0.1g) sitting on top of the sediment with cavities (in both formation history cases) will cause negligible additional settlement (<5% of settlement caused by the static load) and a minor reduction of stiffness. Furthermore, for a seismic induced settlement of 1cm, the average subsurface strain underneath such a large mat would be lower than 10^{-4}, and no major reduction of stiffness or strength properties would be expected.

8.3 Conclusions

A very large structure and soft zones/cavities of several size and numbers were simulated in this section. The presence of cavities lowers the yield load (yet not necessarily the global bearing capacity for this geometry). The yield load is sensitive to the cavities/soft zones, yet it is significantly higher than the target structural load in most cases.

No cohesion was added to any of the layers. However, open pipes and tensile fractures observed at the Vogtle excavation suggest cementation in the host layer and/or the layer above. Adding cohesion to the overlying layer will dramatically diminish the impact of soft zones on shallow foundations.

Once again, these results suggest that differences in formation history can be disregarded for all practical purposes in the hypothetical cases, and that more complex dynamic analyses that take into consideration inertial effects may not be necessary from a foundation response point of view.

Table 8.1. Selected material properties

Parameter	**Source**	**Upland Unit**	**Tobacco Road**	**Dry Branch**	**Santee**	**Warley Hill**
Depth [m]		0 - 8	8 - 13	13 - 40	40 - 48	48 - 200
Effective unit weight γ [kN/m^3]		20	10	10	10	10
Shear velocity V_s [m/s]	Shannon and Wilson (2007)	350	300	300	250	500
Small-strain Poisson's ratio υ	Assumed	0.15	0.15	0.15	0.15	0.15
Young's modulus E_{max} [MPa]	from Vs	*574*	*422*	*422*	*293*	*1173*
Modulus reduction factor II	back-calculated	*6.9*	*2.7*	*2.5*	*2.2*	*1.0*
Effective modulus E [MPa]	from back-analysis	*85*	*156*	*170*	*130*	*1165*
Drained Poisson's ratio υ	Assumed	0.2	0.2	0.2	0.2	0.2
Friction ϕ [^{o}]	Shannon and Wilson (2007)	37	35	34	24	43
MCC strength M (for AC)	from ϕ	1.51	1.42	1.38	0.94	1.77
Cohesion MC	Assumed	0	0	0	0	0
Dilation Ψ [^{o}]	Assumed	0	0	0	0	0
Earth pressure k_0	Assumed	1.0	1.0	1.0	1.0	1.0

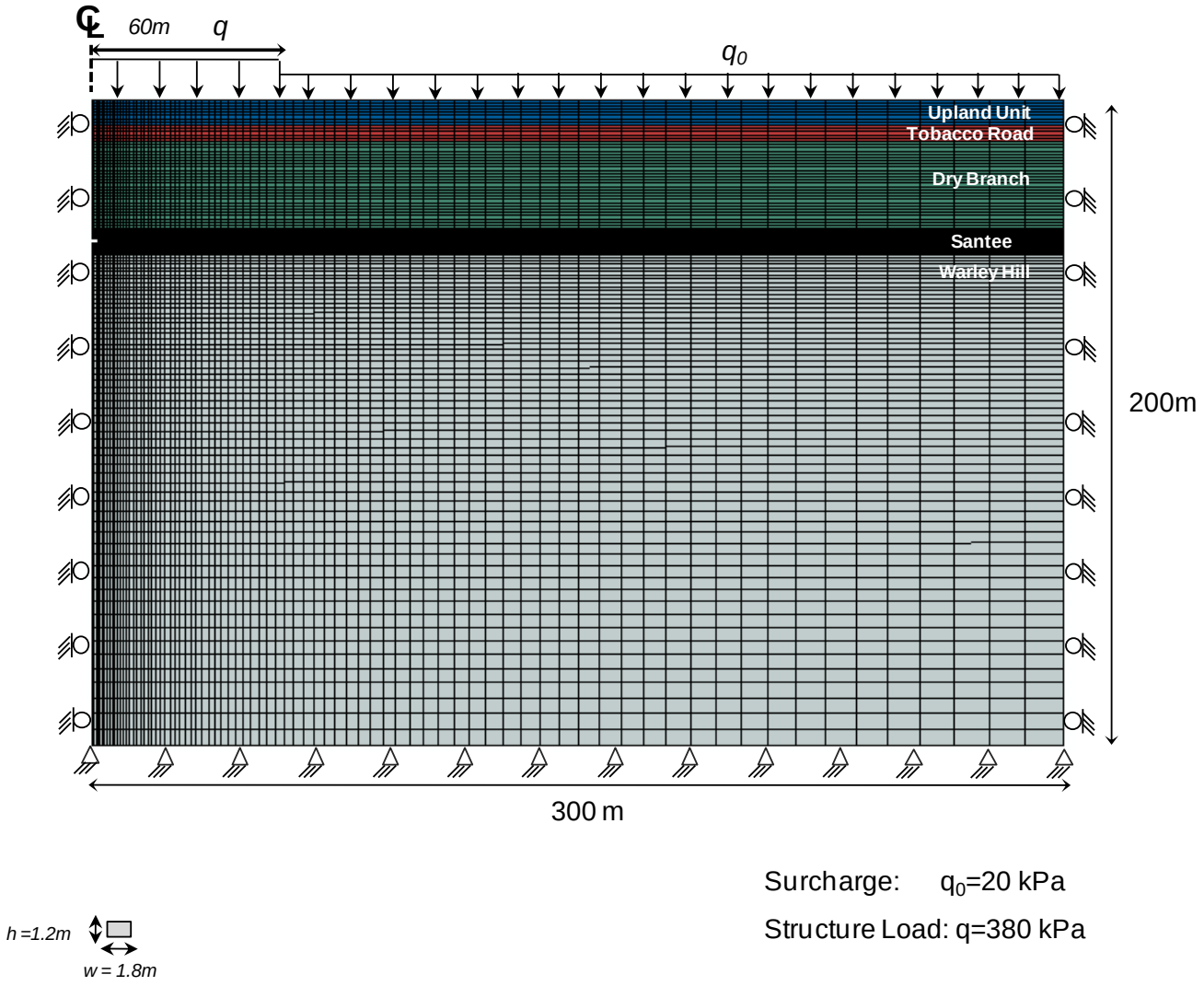

Figure 8.1. Geometry - Boundary conditions (Case 1)

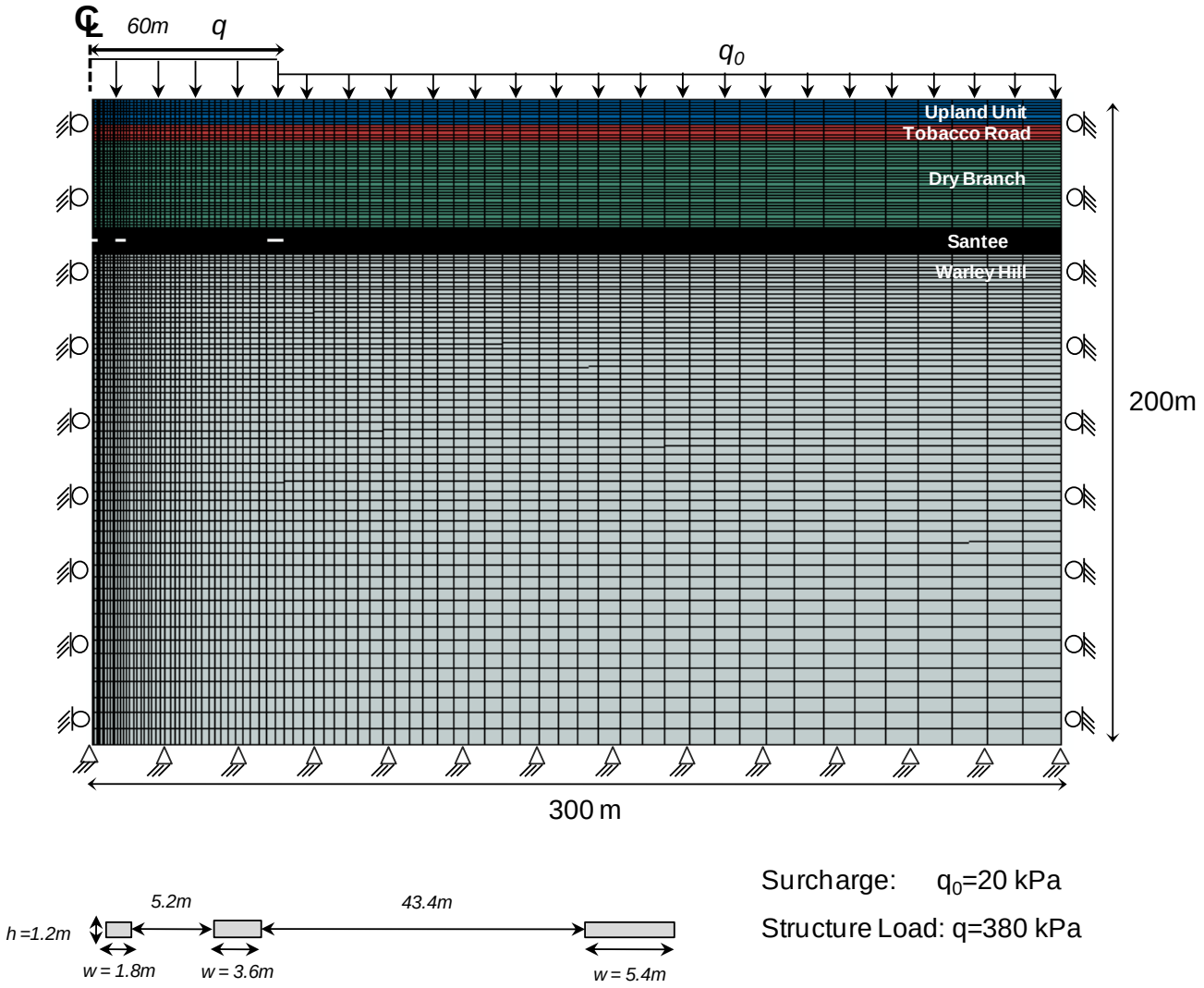

Figure 8.2. Geometry - Boundary conditions (Case 2)

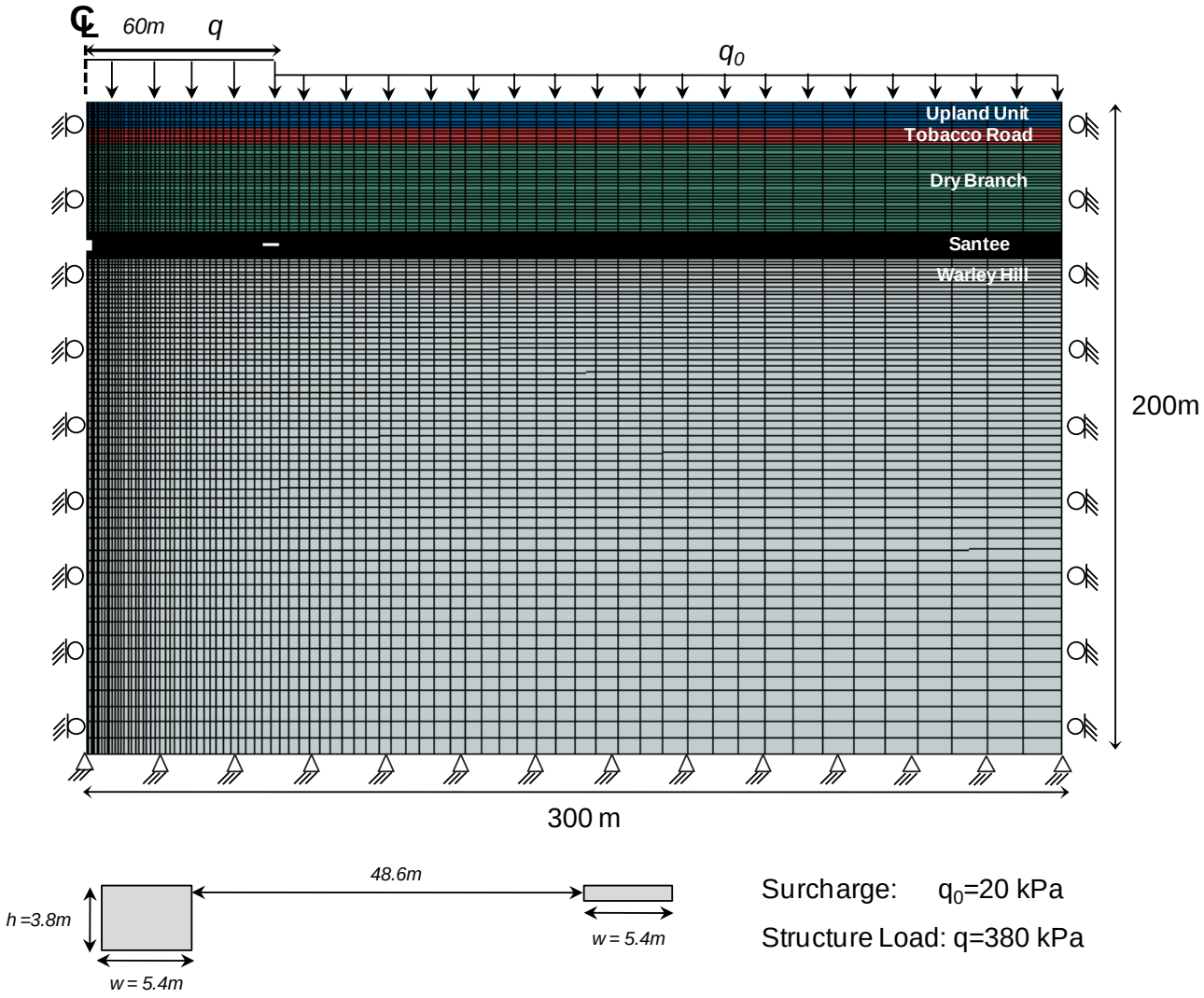

Figure 8.3. Geometry - Boundary conditions (Case 3)

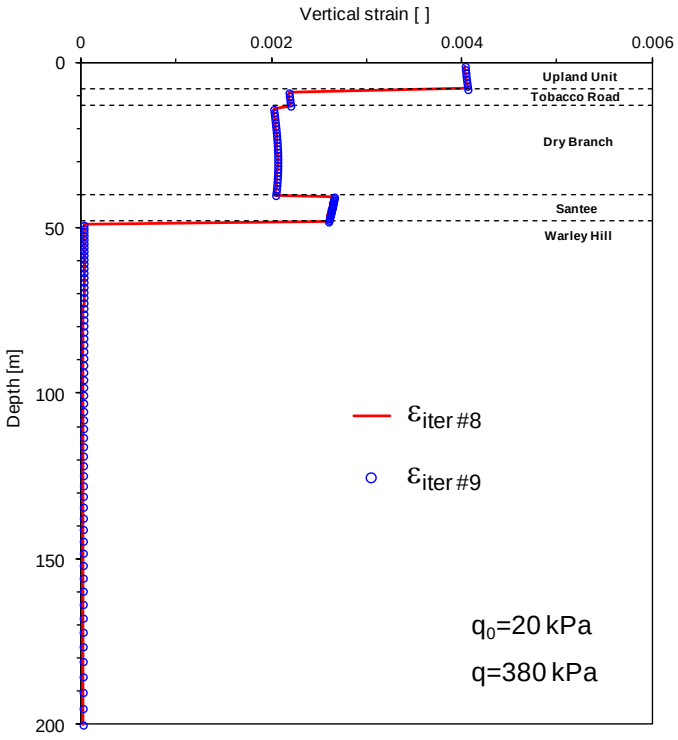

Figure 8.4. Convergence: $\varepsilon_{iter\ i}$ vs. $\varepsilon_{iter\ i+1}$ (No Soft zone)

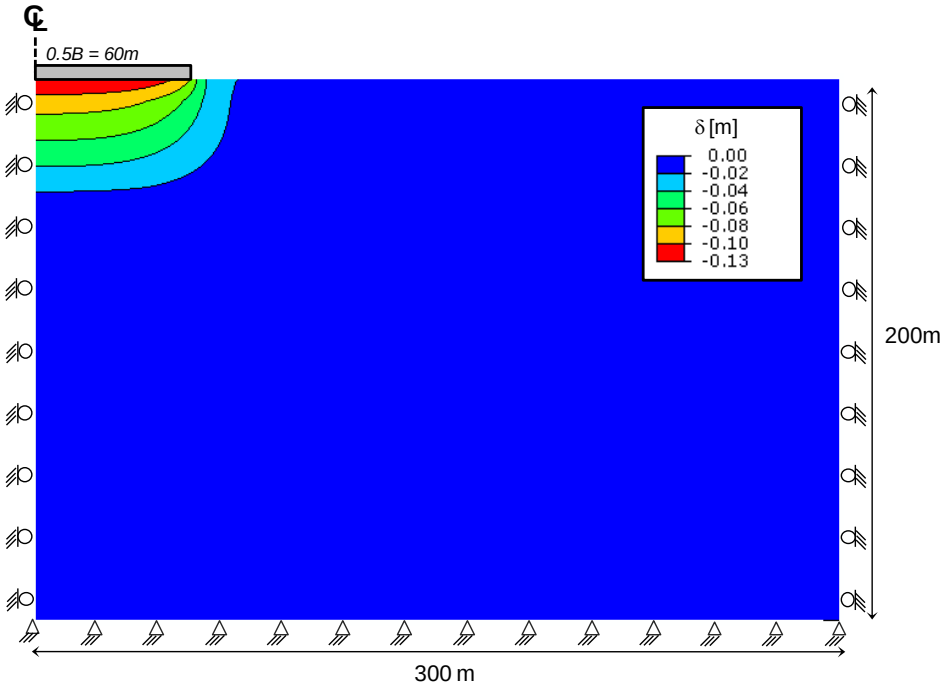

Figure 8.5. Displacement field - Building load (No soft zone) applied in load-controlled mode (flexible footing)

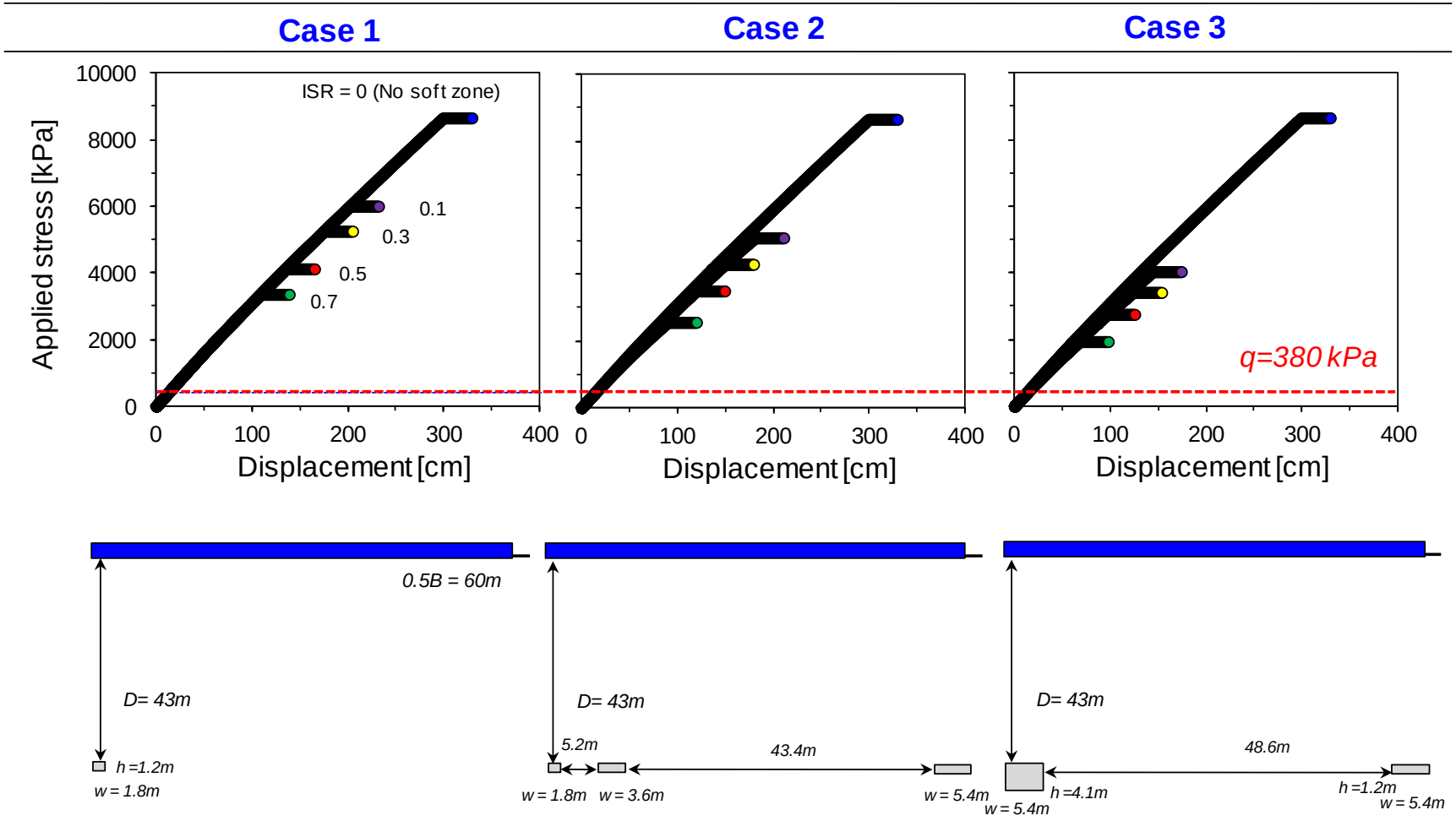

Figure 8.6. Load – Displacement

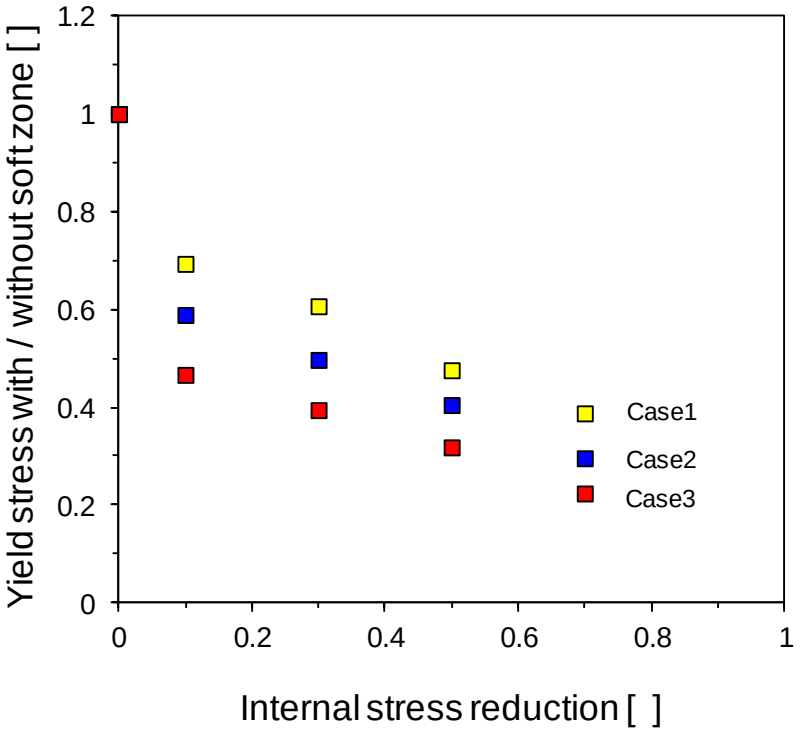

Figure 8.7. Soft zones: Normalized yield stress

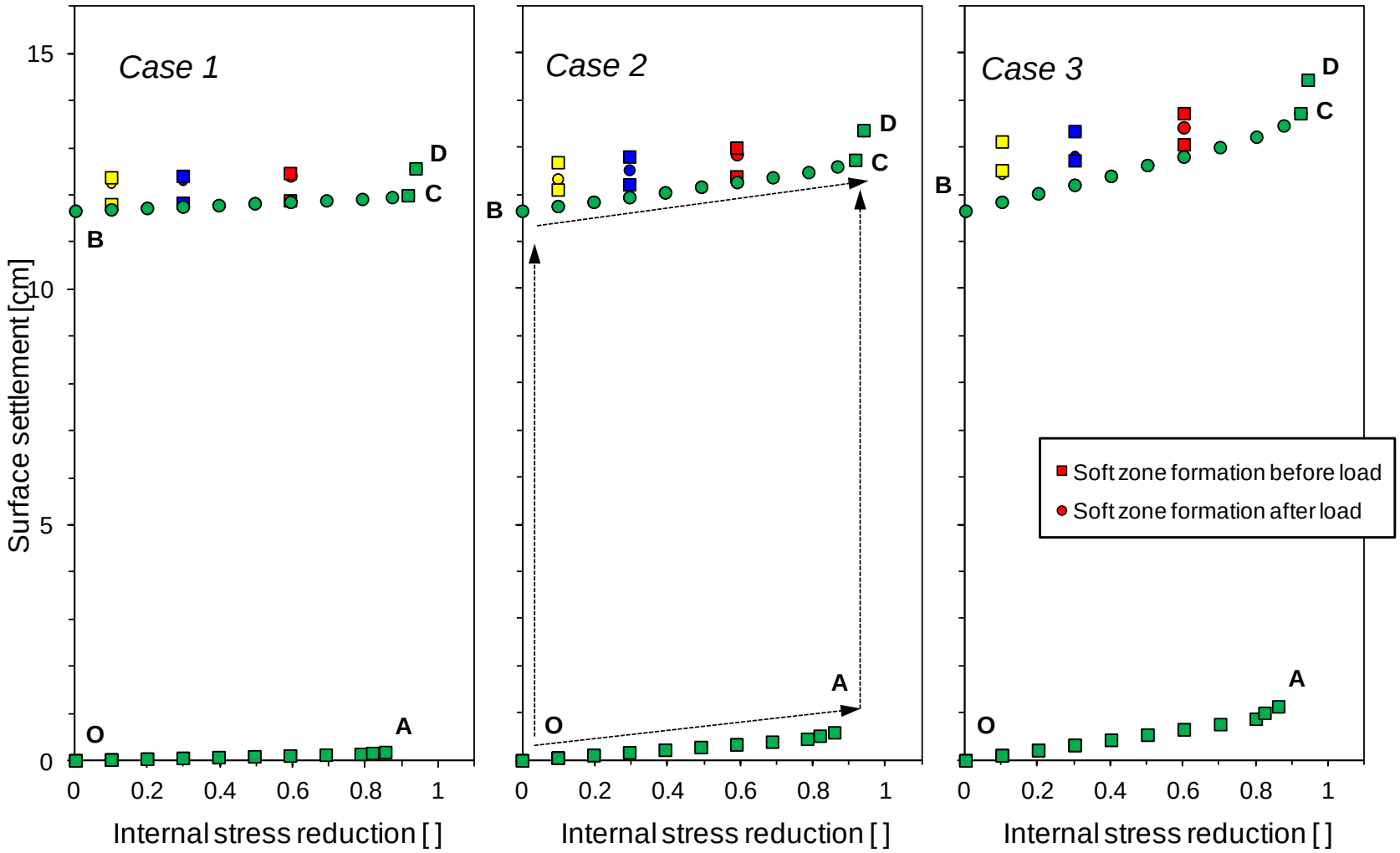

Figure 8.8. Settlement: Footing load, soft zone formation, and seismic load (z_0 = 43 m)

CHAPTER 9

CONCLUSIONS

Dissolution cavities and soft zones in the subsurface at the Savannah River Site (SRS) raise concerns about their potential impact on near-surface structures. This research investigated the effect of subsurface mass loss on the response of shallow foundations. This is a deformation-centered analysis. Therefore, this thesis focuses on soil compressibility and macroscale deformation analyses within the framework of finite element simulations. The salient conclusions from this study follow.

I. Physical properties: Stiffness

Soil compressibility: Physics informed model

- The modified version of Terzaghi's equation is proposed to accommodate two asymptotic conditions at low and high stress with a small number of physically meaningful parameters.
- The high correlation between C_c and e_{ref} suggest a lower level of model complexity. The remolded clays and natural sedimentary clays are related to $C_{c\text{-}natural} \approx 1.1 C_{c\text{-}remolded}$.
- The proposed model explicitly includes preloading effects without the need for graphical interpretation of data to determine the preconsolidation stress.

Small and large strain stiffness

- The small strain stiffness is a constant-fabric perturbation measurement. The tangent stiffness to large strain response is the local rate of fabric change with strain. The measured small strain stiffness and the computed tangent stiffness

increase with the effective stress under isotropic and ko loading conditions. Significant differences in the magnitude of stiffness measured in oedometer are attributed to seating effects, which remain unresolved in oedometer tests. Small strain and tangent stiffness evolve very differently in deviatoric loading.

- A preliminary analysis of simple and robust constitutive models frequently used in practice shows that these models fail to capture differences among small and large strain stiffness. This observation extends to elasto-plastic Drucker-Prager, hyperbolic, and Cam Clay-type models.

Terminal densities for repetitive k_o-loads

- Most of the volumetric change occurs during the early cycles. Change in void ratio per cycle is nonlinear, and it gradually decreases with the number of loading cycles. Void ratio changes are more pronounced in loose sands and at low static load.
- The initial packing density characterizes the compression line obtained from monotonic load tests. Upon subsequent monotonic loading after cyclic loading, the pre-accumulated strain effect is erased, and void ratio trends converge at higher stress level.
- A simple mathematical model is proposed to predict the void ratio e_i after the ith cycle from the void ratio e_1 at the first cycle. Empirical correlations are established in terms of change in relative density to the terminal void ratio $\Delta D_T = (e_1 - e_T) / (e_{max} - e_{min})$ and the initial relative density $D_{i=1} = (e_{max} - e_1) / (e_{max} - e_{min})$.
- The soil accumulates plastic volumetric strain when the corresponding strain level is above the elastic threshold strain. Soils with a higher static load and a denser initial state quickly settle into plastic shakedown state and experience smaller volumetric strains. As the process approaches plastic shakedown, the net volume change per cycle becomes zero, and the sediment reaches terminal density.

II. Subsurface volume contraction – Preliminary studies

Constitutive model - Simulation

- Given the complexity of the load-dissolution histories, simple models are preferred to investigate a wide range of possible conditions.
- Selected models require a small number of physically meaningful parameters that can be reliably estimated from characterization studies.
- Subsurface volume loss and soft zone formation can be numerically simulated by gradually reducing the in situ state of stress in the predefined soft zone. The module developed for these simulations is validated with analytical solutions. Careful mesh refinement is required to avoid numerical effects.

Soft zone-footing interaction – Settlements and bearing capacity

- Smaller and deeper cavities, higher friction angles, and a higher preconsolidation ratio lead to lower settlements at all depths.
- Surface and subsurface settlements are quite regular and can be adequately fitted with a two parameter Gaussian function in the absence of pronounced shear distortions and localizations.
- The linear superposition method of surface settlements caused by neighboring cavities overestimates deformations.
- Shallow cavities interact with the footing, lower the bearing capacity, increase settlements, and promote local-punching failures. When the footing size is much wider than the soft zone size $B >> w$, failure remains global (and embodies the soft zone); global shear failures also develop when $B << w$ and $z_0 > w$. Hence, the worst condition corresponds to $B \sim w$ when punching shear failures prevail.
- The critical depth that separates shallow cavities from deep cavities depends on ratio of soft zone depth to footing width z_0/B, anomaly size B/w, dilatancy ψ, and

the internal stress reduction ISR in the soft zone. As a guiding rule, cavities deeper than z_0~3B-to-4B would be deep soft zones when B/w ~ 1 (the most critical case).

III. SRS Project

Material Parameters

- Preliminary analyses conducted with compressibility parameters gathered in consolidation tests overpredict settlements, possibly due to sampling effects and procedural difficulties (e.g., core-ring gap, cap seating effects magnified by thin specimens). Thus, the selection of stiffness and compressibility at the SRS site must be based on field stiffness measurements. Laboratory-based parameters may overestimate settlements by a factor of 10 or higher.
- The back analysis of measured settlement for the estimation of material parameters faces inherent difficulties with convergence and non-uniqueness of the solution. These are exacerbated by the stress-dependency, nonlinear soil behavior, spatial and temporal variability, and typically limited information available in most field cases.
- The approach developed and implemented in this study involves a simple secant formulation using a robust elasto-plastic numerical model and is anchored on credible field-measured parameters.

Predictions specific to SRS

- The SRS subsurface model is calibrated through back analysis of settlement data gathered during the construction of the Defense Waste Processing Facility at SRS. The initial stiffness adopted for each layer is based on small strain geophysical field measurements.
- Results for this facility at SRS show that load-induced settlements overwhelm

settlements induced by soft zone formation (before or after) and seismic events.

- The formation of cavities or soft zones either before or after the application of the building load may cause an increase in settlement of less than 10-20% (for the simulated conditions, which disregard cementation and dilation). Thus, the differences in formation history can be disregarded for all practical purposes, within the limitations of the hypothetical cases analyzed in this study.
- Seismic loading of the structure (a_h = 0.1g) sitting on top of the sediment with cavities (in both formation history causes) will cause negligible additional settlement (<5 % of settlement caused by the static load). Furthermore, anticipated seismic induced strains are low and no major reduction of stiffness or strength properties would be expected. On the bases of these results, more complex seismic models that take into consideration inertial effects are not necessary at this point and for the purposes of this analysis.
- No cohesion is considered in any of the layers throughout this study. Stable open cavities and tensile fractures observed at the Vogtle excavation suggest cementation. Adding cohesion to overlying layers would dramatically diminish the impact of soft zones on shallow foundations.

APPENDIX A

PRELIMINARY OBERVATIONS ON THE CHOICE OF CONSTITUTIVE MODEL

The selection of constitutive models has been a recursive process in this research. Our criteria for model selection have been driven by the need for:

- a simple model capable of capturing a wide range of stress paths
- a small number of physically meaningful parameters
- model parameters which must be able to be reliably estimated from characterization studies

Elastic, elasto-plastic with Drucker-Prager yield criterion (the conical yield surface provides more stable numerical simulations in complex stress paths than the hexagonal yield surface that characterizes the Mohr-Coulomb criterion), and Modified Cam Clay models were used throughout this study. The constitutive models are described in Table A1. Predicted stress-strain responses in each case are shown in Figure A1, Figure A2, and Figure A3. Most simulations were repeated with both plastic models. Selected runs most relevant to this study are presented in each case.

The selection of a constitutive model and modeling strategy is intimately related to the nature of the problem and it is constrained by available information. In particular, our modeling approach recognizes:

- The stress field is very sensitive to model and model parameters in kinematically coupled conditions (Figure A4); this is not necessarily the case in large shallow foundation problems.
- Algorithms must be verifiable at all stages against closed-form solutions for similar conditions (Figure A5).
- Complex models imply a large number of parameters; this favors the ability of

predicting past data, but hinders the robust predictability of future performance (Figure A6). We will place preference for simple, robust models that can be calibrated with available data.

- Field performance data is typically smooth, hence, information-limited. For example, settlement results shown in Figure A7 can be closely fitted with a 3rd order polynomial; this means that regardless of the number of measurement points gathered throughout the foundation and the construction history, these settlement data provides 4 “pieces of information” only (for comparison, x-y data fitted with a straight line y=a+bx provides only 2 pieces of information: a and b). We are guided by Ockham’s criterion throughout this research.

Table A1. Constitutive models used in this study

Drucker-Prager model (Drucker and Prager, 1952)

The failure surface f defines the boundary between elastic and perfectly plastic deformations. The onset of plastic deformation or failure surface is defined by f = 0. The material remains in the elastic regime as long as f < 0 and deforms plastically for f = 0. Thus, the state of stresses at failure is given by:

$$f = q - (\xi p + \chi) = 0 \quad \text{where} \quad \xi = \frac{6\sin\phi}{3-\sin\phi} \quad \text{and} \quad \chi = \frac{6\cos\phi}{3-\sin\phi} c$$

The plastic deformation on the failure surface is determined by the plastic potential function. If the plastic potential function is equal to the failure function, the material is said to follow an associated flow rule, otherwise the material follows a non-associated flow rule.

Modified Cam-Clay model (Schofield and Wroth, 1968; Muir Wood, 1990)

The yield surface is an ellipse in the p-q plane. It is closed in all directions for stress paths that are generated in isotropic or ko-compression, direct shear or triaxial laboratory tests. Thus, it can easily reproduce most of experimental tests, confinement-dependent and nonlinear soil behavior but with limitation to monotonic loads. The size of the yield surface is characterized by preconsolidation pressure p'_c. The MCC model follows an associative flow rule: the plastic strain increment vector for the largest value of the mean effective stress p is horizontal and therefore no incremental deviatoric plastic strain take place for a change in mean effective stress. The yield surface is defined as follows:

$$f = \left[\frac{q}{M}\right]^2 + p(p - p_c) = 0$$

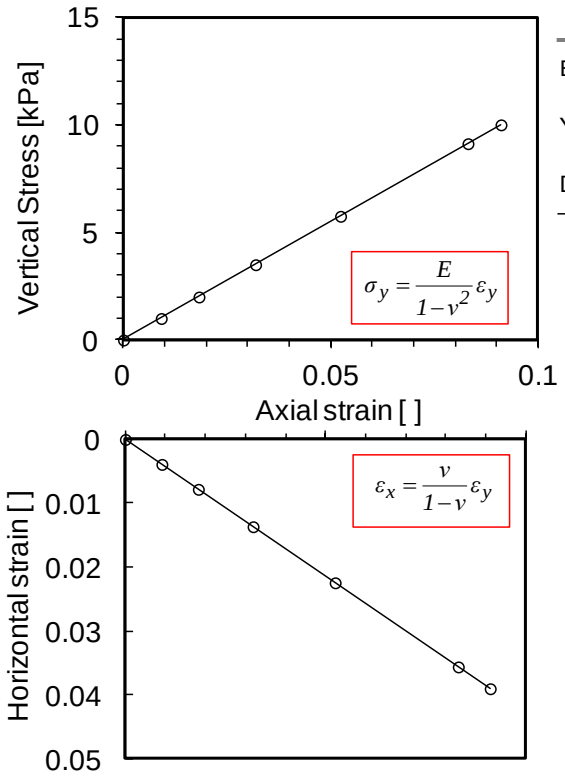

Element type	Plane Strain
Young's modulus E [MPa]	300
Drained Poisson's ratio υ	0.3

Figure A1. Elastic model

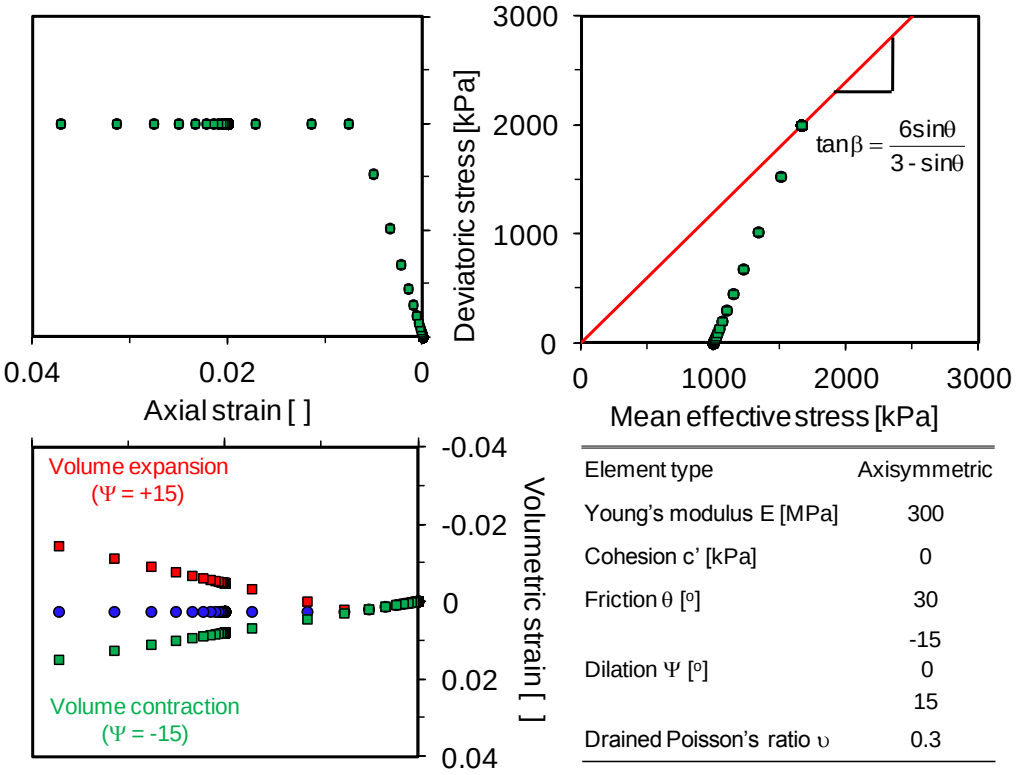

Element type	Axisymmetric
Young's modulus E [MPa]	300
Cohesion c' [kPa]	0
Friction θ [°]	30
Dilation Ψ [°]	-15 0 15
Drained Poisson's ratio υ	0.3

Figure A2. Elasto-plastic model (Note that strain hardening takes place in plane strain)

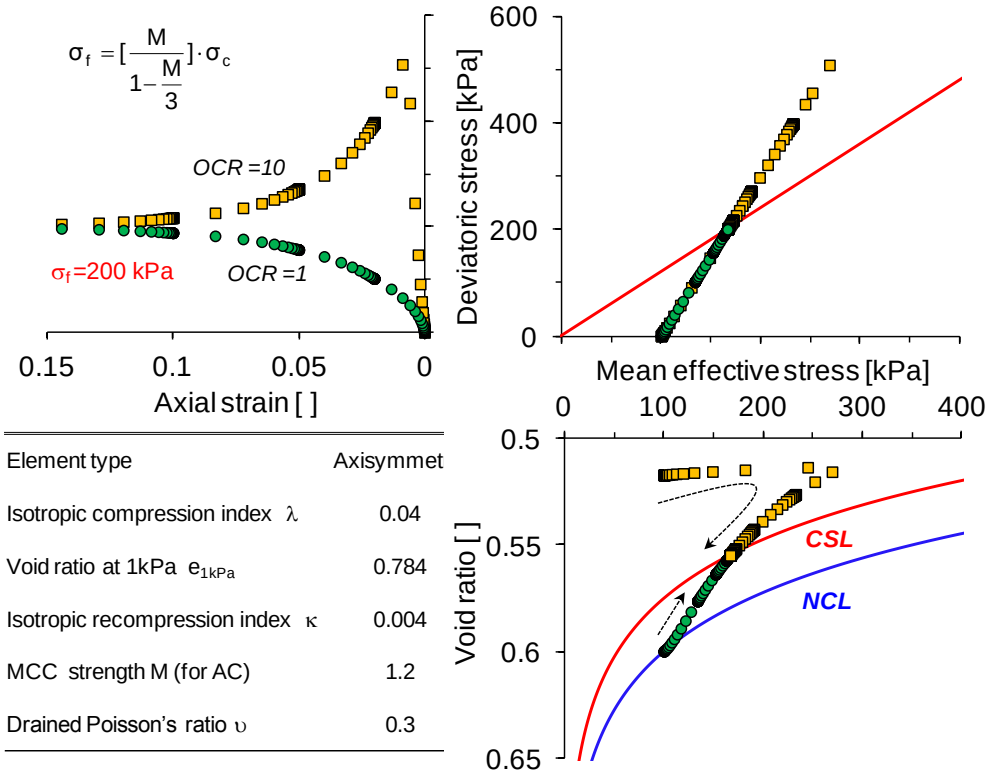

Element type	Axisymmet
Isotropic compression index λ	0.04
Void ratio at 1kPa e_{1kPa}	0.784
Isotropic recompression index κ	0.004
MCC strength M (for AC)	1.2
Drained Poisson's ratio υ	0.3

Figure A3. Modified Cam clay model

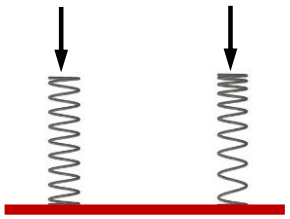

Model-independent force
Model-dependent deformation
(e.g., closed-form solution)

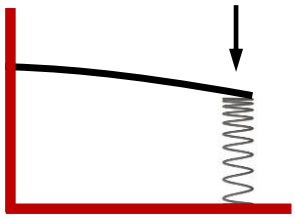

Kinematically coupled
Model-dependent force
Model-dependent deformation
(e.g., finite element analysis)

Figure A4. Geotechnical problems: Constitutive models

Boussinesq

$$\Delta\sigma_v = \frac{q}{\pi}\left[\beta + \sin\beta\cos\left(\beta + 2\alpha\right)\right]$$

$$\Delta\sigma_h = \frac{q}{\pi}\left[\beta - \sin\beta\cos\left(\beta + 2\alpha\right)\right]$$

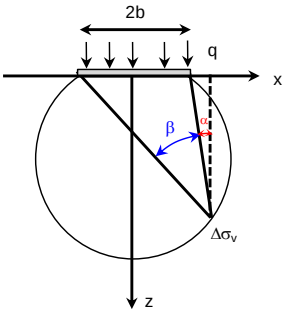

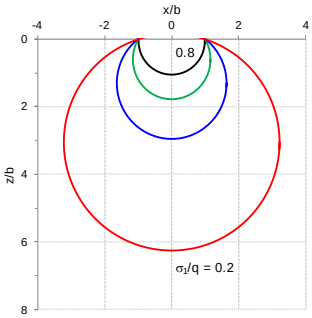

Kirsch

$$\sigma_r = p_i\frac{a^2}{r^2} + \frac{\sigma_{v\infty}}{2}\left(1 - \frac{a^2}{r^2}\right) + \frac{\sigma_{v\infty}}{2}\left(1 + \frac{3a^4}{r^4} - \frac{4a^2}{r^2}\right)\cos 2\theta$$

$$\sigma_\theta = -p_i\frac{a^2}{r^2} + \frac{\sigma_{v\infty}}{2}\left(1 + \frac{a^2}{r^2}\right) - \frac{\sigma_{v\infty}}{2}\left(1 + \frac{3a^4}{r^4}\right)\cos 2\theta$$

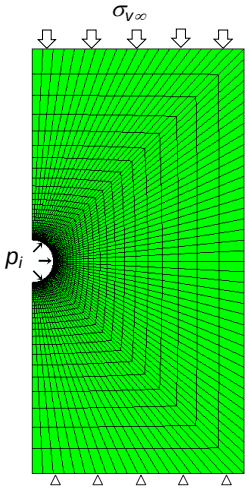

Figure A5. Geotechnical problems: Constitutive models

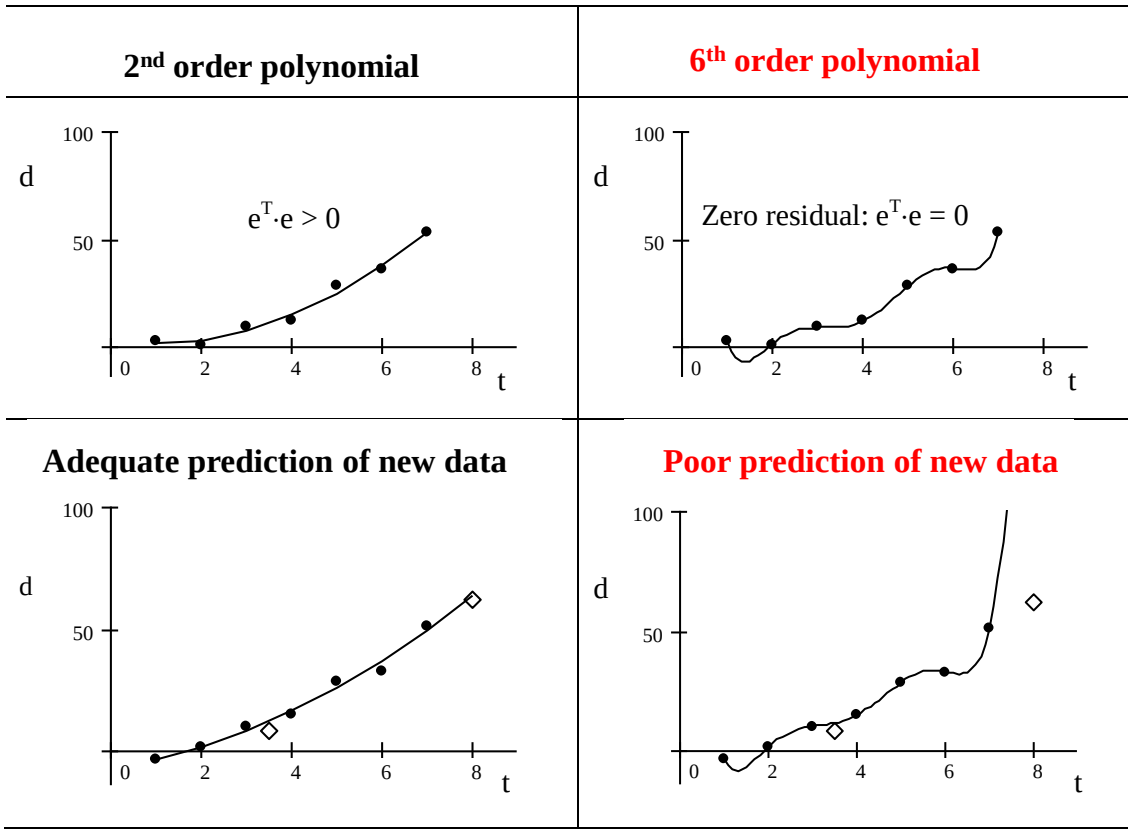

Figure A6. How much information is in the data? (Santamarina and Fratta, 2005)

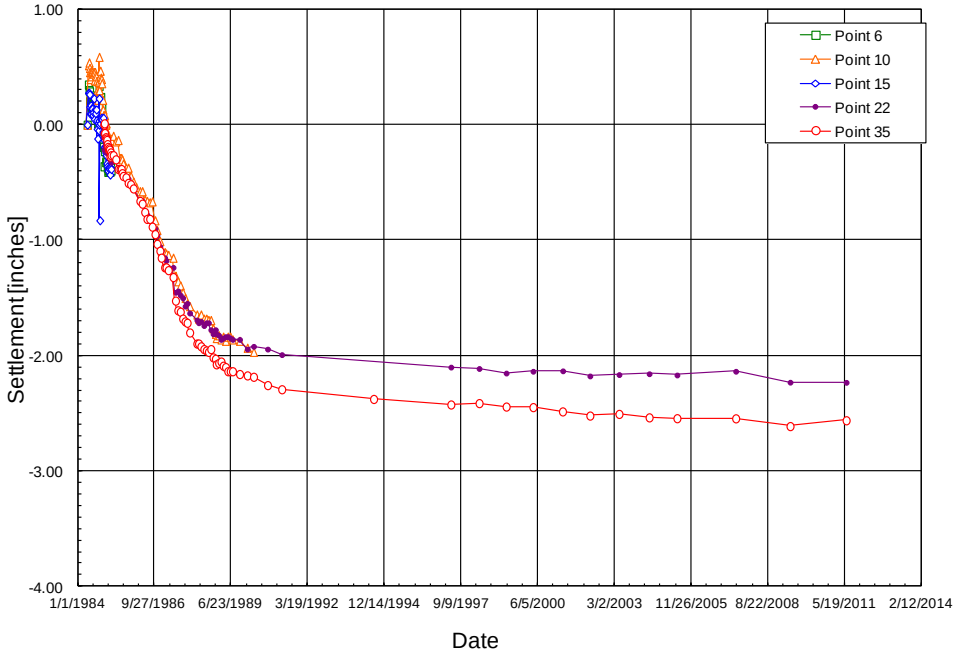

Figure A7. How much information is in these field settlement data? (data from SRNS, 2011)

APPENDIX B

EHANCED TERZAGHI'S MODEL - EXAMINATION

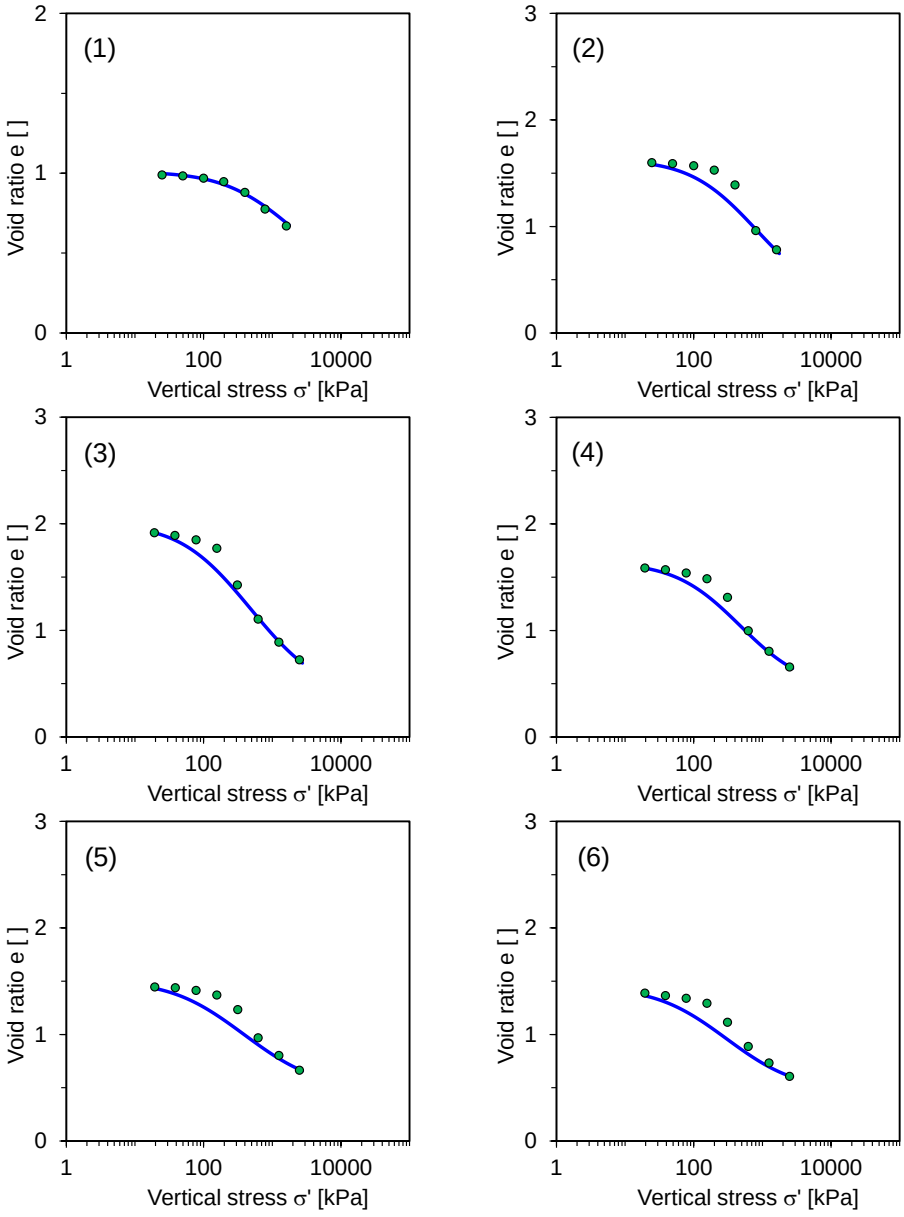

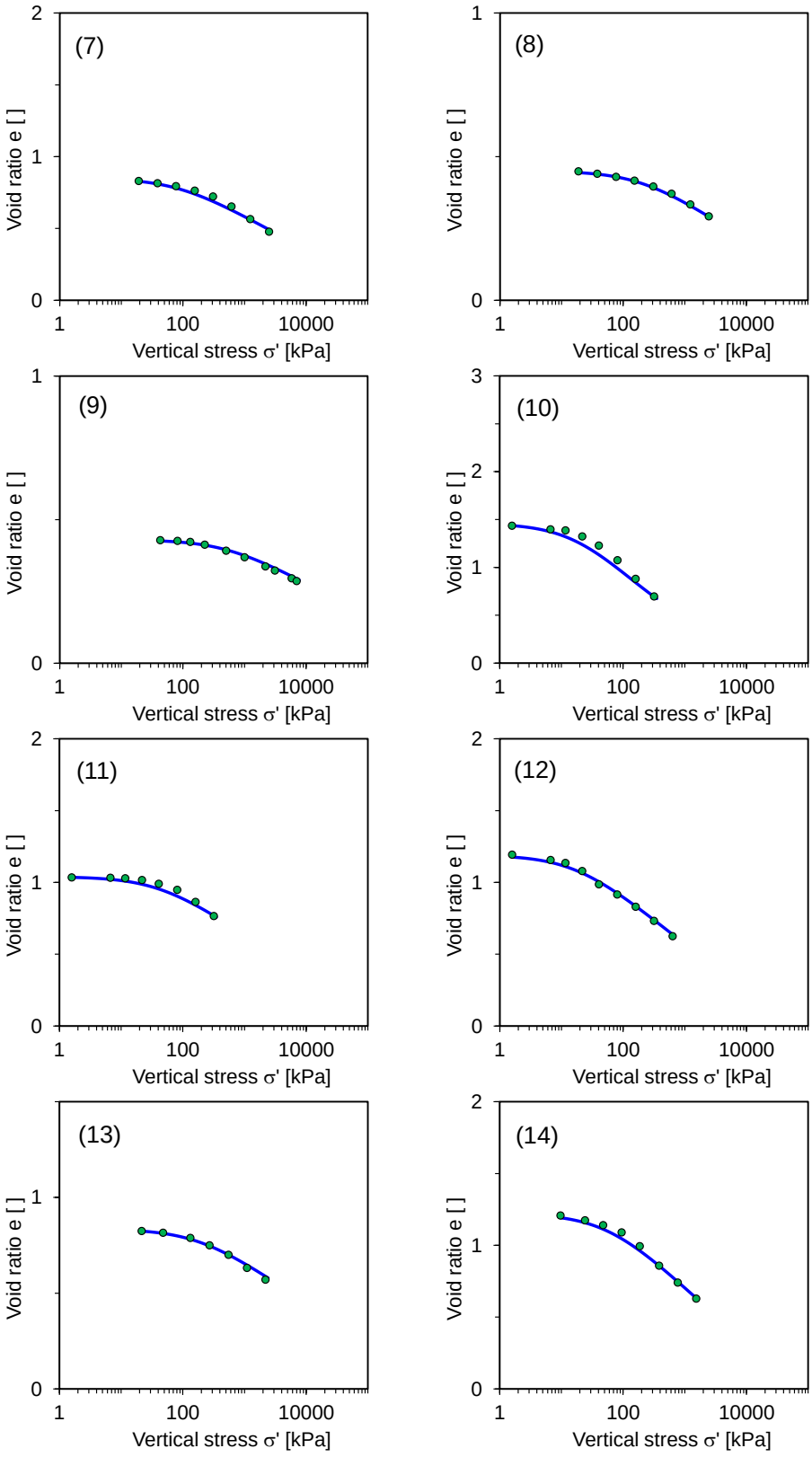
(7)
(8)
(9)
(10)
(11)
(12)
(13)
(14)
Void ratio e [ ]
Vertical stress σ' [kPa]
1
100
10000

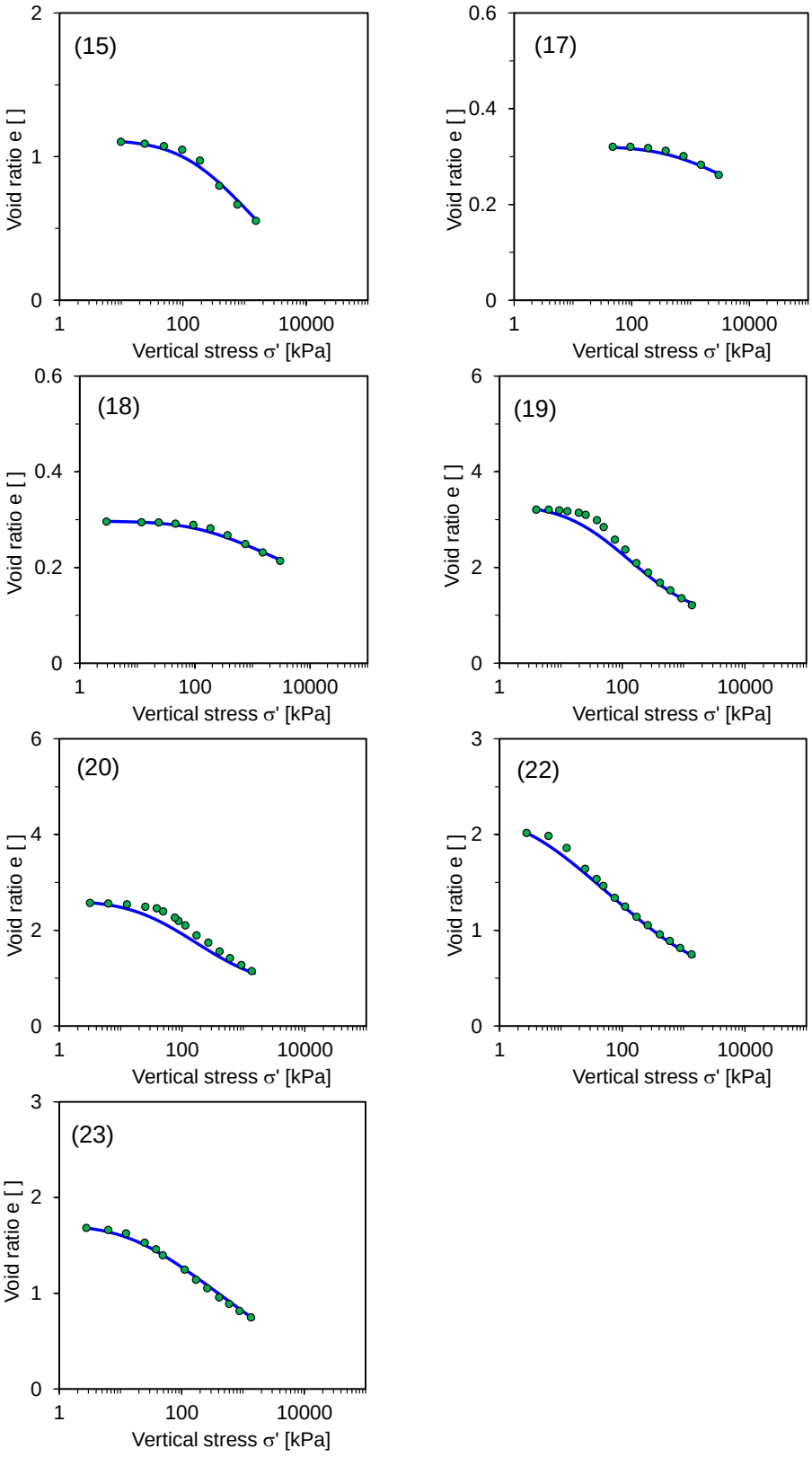
(15)
Void ratio e [ ]
Vertical stress σ' [kPa]
(17)
Void ratio e [ ]
Vertical stress σ' [kPa]
(18)
Void ratio e [ ]
Vertical stress σ' [kPa]
(19)
Void ratio e [ ]
Vertical stress σ' [kPa]
(20)
Void ratio e [ ]
Vertical stress σ' [kPa]
(22)
Void ratio e [ ]
Vertical stress σ' [kPa]
(23)
Void ratio e [ ]
Vertical stress σ' [kPa]

REFERENCES

Achmus, M., Kuo, Y.-S., and Abdel-Rahman, K. (2009). "Behavior of monopile foundations under cyclic lateral load." *Computers and Geotechnics*, 36(5), 725-735.

Ahmed, M. and Iskander, M. (2011). "Analysis of Tunneling-Induced Ground Movements Using Transparent Soil Models." *Journal of Geotechnical And Geoenvironmental Engineering*, 137(5), 525-535.

Alonso-Marroquin, F. and Herrmann, H. J. (2004). "Ratcheting of Granular Materials." *Physical Review Letters*, 92(5).

Alonso, E. E., Pinyol, N. M., and Puzrin, A. M. (2010). *Geomechanics of failures: Advanced topics*, Springer.

Amar, S. (1994). "Experimental study of the settlement of shallow foundations." *Vertical and horizontal deformations of foundations and embankments*, Vol. 2, GSP 40, 1602-1610.

Anderson, D. G. and Richart, F. E. (1976). "Effects of straining on the shear modulus of clays." *Journal of the Geotechnical Engineering Division*, 102(9), 975-987.

Aplin, A. C., Yang, Y., and Hansen, S. (1995). "Assessment of β the compression coefficient of mudstones and its relationship with detailed lithology." *Marine and Petroleum Geology*, 12(8), 955-963.

Athy, L. F. (1930). "Density, porosity, and compaction of sedimentary rocks." *AAPG Bulletin*, 14(1), 1-24.

Atkinson, J. H., Brown, E. T., and Potts, D. M. (1975). "Collapse of Shallow Unlined Tunnels in Dense Sand." *Tunnels and Tunnelling*, 7(3), 81-87.

Atkinson, J. H. and Potts, D. M. (1977a). "Subsidence Above Shallow Tunnels In Soft Ground." *Journal of the Geotechnical Engineering Division*, 103(GT4), 307-325.

Atkinson, J. H. and Potts, D. M. (1977b). "Stability of a shallow circular tunnel in cohesionless soil." *Geotechnique*, 27(2), 203-215.

Atkinson, J. H. (2000). "Non-linear soil stiffness in routine design." *Géotechnique*, 50(5), 487-508.

Azam, G., Hsieh, C. W., and Wang, M. C. (1991). "Performance of strip footing on stratified soil deposit with void." *Journal of Geotechnical Engineering*, 117(5), 753-772.

Badie, A. and Wang, M. C. (1984). "Stability of spread footing above void in clay." *Journal of Geotechnical Engineering*, 110(11), 1591-1605.

Baldi, G., Hueckel, T., and Pellegrini, R. (1988). "Thermal volume changes of the mineral–water system in low-porosity clay soils." *Canadian Geotechnical Journal*, 25(4), 807-825.

Barden, L. (1965). "Consolidation of Clay with Non-linear Viscosity." *Geotechnique*, 15(4), 345-362.

Baumgartl, T. and Köck, B. (2004). "Modeling Volume Change and Mechanical Properties with Hydraulic Models." *Soil Science Society of America*, 68(1), 57-65.

Baus, R. L. and Wang, M. C. (1983). "Bearing capacity of strip footing above void." *Journal of Geotechnical Engineering*, 109(1), 1-14.

Becker, D. E.Crooks, J. H. A.Been, K. and Jefferies, M. G. (1987). "Work as a criterion for determining in situ and yield stresses in clays." *Canadian Geotechnical Journal*, 24(4), 549-564.

Beer, E. E. d. (1970). "Experimental Determination of the Shape Factors and the Bearing Capacity Factors of Sand." *Géotechnique*, 20(4), 387-411.

Ben-Hassine, J. and Griffiths, D. V. (2013). "Geotechnical Exploration for Wind Energy Projects." *Proceedings of the 18th International Conference on Soil Mechanics and Geotechnical Engineering, Paris*, Vol. 3, Technical Committee 209, 2319-2322.

Berger, R. D. (1981). "Comparison of the gompertz and logistic equations to describe plant disease progress." *Phytopathology*, 71, 716-719.

Bobet, A. (2001). "Analytical Solutions for Shallow Tunnels in Saturated Ground." *Journal of Engineering Mechanics*, 127(12), 1258-1266.

Boone, S. J. (2010). "A critical reappraisal of “preconsolidation pressure” interpretations using the oedometer test." *Canadian Geotechnical Journal*, 47(3), 281-296.

Borja, R. I. and Lee, S. R. (1990). "Cam-Clay plasticity, Part 1: Implicit integration of elasto-plastic constitutive relations." *Computer Methods in Applied Mechanics and Engineering*, 78(1), 49-72.

Bouckovalas, G., Whitman, R., and Marr, W. (1984). "Permanent Displacement of Sand With Cyclic Loading." *Journal of Geotechnical Engineering*, 110(11), 1606-1623.

Breidenich, C.Magraw, D.Rowley, A. and Rubin, J. W. (1998). "The Kyoto Protocol to the United Nations Framework Convention on Climate Change." *The American Journal of International Law*, 92(2), 315-331.

Briaud, J. and Gibbens, R. (1999). "Behavior of Five Large Spread Footings in Sand." *Journal of Geotechnical and Geoenvironmental Engineering*, 125(9), 787-796.

Brinch Hansen, J. (1963). "Discussion of "Hyperbolic stress-strain response: cohesive soils"." *Journal of the Soil Mechanics and Foundations Division*, 89(SM 4), 241-242.

Burd, H. J.Houlsby, G. T.Chow, L.Augarde, C. E. and Liu, G. (1994). "Analysis of settlement damage to masonry structures." *Proceeding of the 3rd European Conference on Numerical Methods in Geotechnical Engineering, UK*, 203-208.

Burland, J. B. (1989). "Ninth Laurits Bjerrum Memorial Lecture: "Small is beautiful"—the stiffness of soils at small strains." *Canadian Geotechnical Journal*, 26(4), 499-516.

Burland, J. B. (1990). "On the compressibility and shear strength of natural clays." *Geotechnique*, 40(3), 329-378.

Burns and Roe Enterprises, I. (2001). "Final geotechnical investigation report - Volume I." U.S. Department of Energy.

Butterfield, R. (1979). "A natural compression law for soils (an advance on e-logp')." *Geotechnique*, 29(4), 469-480.

Calvello, M. and Finno, R. J. (2004). "Selecting parameters to optimize in model calibration by inverse analysis." *Computers and Geotechnics*, 31(5), 410-424.

Campanella, R. G. and Mitchell, J. K. (1968). "Influence of temperature variations on soil behavior." *Journal of Soil Mechanics and Foundations Division*, 94(SM3), 709-734.

Carrier, W. D. and Beckman, J. F. (1984). "Correlations between index tests and the properties of remoulded clays." *Geotechnique*, 34(2), 211-228.

Casagrande, A. (1936). "The determination of the pre-consolidation load and its practical significance." *Proceedings of the 1st International Soil Mechanics and Foundation Engineering Conference, Cambridge, Mass.*, Vol. 3, 60-64.

Cascante, G. and Santamarina, J. (1996). "Interparticle Contact Behavior and Wave Propagation." *Journal of Geotechnical Engineering*, 122(10), 831-839.

Cascante, G., Santamarina, C., and Yassir, N. (1998). "Flexural excitation in a standard torsional-resonant column device." *Canadian Geotechnical Journal*, 35(3), 478-490.

Celestino, T. B., Gomes, R. A. M. P., and Bortolucci, A. A. (2000). "Errors in ground distortions due to settlement trough adjustment." *Tunnelling and Underground Space Technology*, 15(1), 97-100.

Cha, M. S.Santamarina, J. C.Kim, H. S. and Cho, G. C. (2014). "Small-Strain Stiffness, Shear Wave Velocity and Soil Compressibility." *Journal of Geotechnical and Geoenvironmental Engineering (Accepted)*.

Chang, C. and Whitman, R. (1988). "Drained Permanent Deformation of Sand Due to Cyclic Loading." *Journal of Geotechnical Engineering*, 114(10), 1164-1180.

Chang, C. S., Misra, A., and Sundaram, S. S. (1991). "Properties of granular packings under low amplitude cyclic loading." *Soil Dynamics and Earthquake Engineering*, 10(4), 201-211.

Chen, K.Cole, J.Conger, C.Draskovic, J.Lohr, M.Klein, K.Scheidemantel, T. and Schiffer, P. (2006). "Granular materials: Packing grains by thermal cycling." *Nature*, 442(7100), 257-257.

Chen, S. L., Gui, M. W., and Yang, M. C. (2012). "Applicability of the principle of superposition in estimating ground surface settlement of twin- and quadruple-tube tunnels." *Tunnelling and Underground Space Technology*, 28(0), 135-149.

Chen, W. F. (1975). *Limit analysis and soil plasticity*, Elsevier, Amsterdam.

Chilingar, G. V. and Knight, L. (1960). "Relationship between pressure and moisture content of kaolinite, illite, and montmorillonite clays." *American Association of Petroleum Geologists Bulletin*, 44(1), 101-106.

Cho, G. C., Dodds, J., and Santamarina, J. C. (2006). "Particle shape effects on packing density, stiffness, and strength: natural and crushed sands." *Journal of Geotechnical and Geoenvironmental Engineering*, 132(5), 591-602.

Cho, G. C., Dodds, J., and Santamarina, J. (2007). "Closure to "Particle Shape Effects on Packing Density, Stiffness, and Strength: Natural and Crushed Sands" " *Journal of Geotechnical And Geoenvironmental Engineering*, 133(11), 1474-1474.

Cividini, A., Jurina, L., and Gioda, G. (1981). "Some aspects of 'characterization' problems in geomechanics." *International Journal of Rock Mechanics and Mining Sciences & Geomechanics Abstracts*, 18(6), 487-503.

Clayton, C. R. I. (2011). "Stiffness at small strain: research and practice." *Geotechnique*, 61(1), 5-37.

Clementino, R. V. (2005). "Discussion: An oedometer test study on the preconsolidation stress of glaciomarine clays." *Canadian Geotechnical Journal*, 42(3), 972-974.

Clough, W. and Schmidt, B. (1981). *Design and performance of excavations and tunnels in soft clay*, In Soft Clay engineering, E. Brand and R. Brenner, eds., Elsevier, 569-634.

Coop, M. R.Sorensen, K. K.Freitas, T. B. and Georgoutsos, G. (2004). "Particle breakage during shearing of a carbonate sand." *Géotechnique*, 54(3), 157-163.

Cording, E. J. (1991). "Control of ground movements around tunnels in soil." *Proceedings of the 9th Pan American Conference on Soil Mechanics and Foundation Engineering, Chile*, 2195-2244.

Cotecchia, F. and Chandler, R. J. (1997). "The influence of structure on the pre-failure behaviour of a natural clay." *Geotechnique*, 47(3), 523-544.

Cotecchia, F. and Chandler, R. J. (2000). "A general framework for the mechanical behaviour of clays." *Geotechnique*, 50(4), 431-447.

Crapps, D. K. (2010). "The effects of cavities upon foundation design and construction." *GeoFlorida 2010, GSP 198*, 206-223.

Dai, S. and Santamarina, J. C. (2014). "Sampling disturbance in hydrate-bearing sediment pressure cores: NGHP-01 expedition, Krishna-Godavari Basin example." *Marine and Petroleum Geology (Accepted)*.

Das, B. (1999). *Shallow foundations: Bearing capacity and Settlement*, CRC Press LLC.

Day, R. A. and Potts, D. M. (2000). "Discussion: Observations on the computation of the bearing capacity factor Nγ by finite elements." *Geotechnique*, 50(3), 301-303.

Deschamps, R. (1995). "Discussion of "Load Settlement Curve Method for Spread Footings on Sand" by Jean-Louis Briaud and Philippe Jeanjean." *Journal of Geotechnical Engineering*, 121(9), 684-685.

Dìaz-Rodrìguez, J., Leroueil, S., and Alemàn, J. (1992). "Yielding of Mexico City Clay and Other Natural Clays." *Journal of Geotechnical Engineering*, 118(7), 981-995.

Drucker, D. C. and Prager, W. (1952). "Soil mechanics and plastic analysis or limit design." *Quarterly of Applied Mathematics*, 10(2), 157-165.

Duncan, J. M. and Chang, C. Y. (1970). "Non-linear analysis of stress and strain in soils." *Journal of the Soil Mechanics and Foundations Division, Proceedings of the American Society of Civil Engineers*, 96(5).

Elhakim, A. F. (2005). "Evaluation of shallow foundation displacements using soil small-strain stiffness." Ph.D Dissertation, School of Civil and Environmental Engineering, Georgia Institute of Technology, U.S.A.

Fahey, M. and Carter, J. P. (1993). "A finite element study of the pressuremeter test in sand using a nonlinear elastic plastic model." *Canadian Geotechnical Journal*, 30(2), 348-362.

Fares, N. F. (1987). "Green's Functions for Plane-layered Elastostatic and Viscoelastic Regions with Application to 3-D Crack Analysis." Ph.D, Massachusetts Institute of Technology.

Fernandez, A. L. and Santamarina, J. C. (2001). "Effect of cementation on the small-strain parameters of sands." *Canadian Geotechnical Journal*, 38(1), 191-199.

Finn, W. D. L. and Vaid, Y. P. (1977). "Liquefaction potential from drained constant volume cyclic simple shear tests." *Proceeding of the 6th World Conference on Earthquake Engineering, New Delhi, India*, Session 6, 7-12.

Finn, W. D. L. (1981). "Liquefaction potential: Developments since 1976." *Proceedings of the International Conference on Recent Advances in Geotechnical Earthquake Engineering and Soil Dynamics*, 2, 655-681.

Finno, R. and Calvello, M. (2005). "Supported Excavations: Observational Method and Inverse Modeling." *Journal of Geotechnical and Geoenvironmental Engineering*, 131(7), 826-836.

Franzius, J. and Potts, D. (2005). "Influence of Mesh Geometry on Three-Dimensional Finite-Element Analysis of Tunnel Excavation." *International Journal of Geomechanics*, 5(3), 256-266.

Frydman, S. and Burd, H. J. (1997). "Numerical studies of bearing capacity factor Nγ." *Journal of Geotechnical and Geoenvironmental Engineering*, 123(1), 20-29.

García-Rojo, R. and Herrmann, H. J. (2005). "Shakedown of unbound granular material." *GM*, 7(2-3), 109-118.

Gioda, G. (1980). "Indirect identification of the average elastic characteristics of rock masses." *International Conference on Structural Foundations on Rock*, Sydney, Australia, 65-73.

Gioda, G. and Maier, G. (1980). "Direct search solution of an inverse problem in elastoplasticity: Identification of cohesion, friction angle and in situ stress by pressure tunnel tests." *International Journal for Numerical Methods in Engineering*, 15(12), 1823-1848.

Gioda, G. and Sakurai, S. (1987). "Back analysis procedures for the interpretation of field measurements in geomechanics." *International Journal for Numerical and Analytical Methods in Geomechanics*, 11(6), 555-583.

Gioda, G. and Locatelli, L. (1999). "Back analysis of the measurements performed during the excavation of a shallow tunnel in sand." *International Journal for Numerical and Analytical Methods in Geomechanics*, 23(13), 1407-1425.

Gompertz, B. (1825). "On the Nature of the Function Expressive of the Law of Human Mortality, and on a New Mode of Determining the Value of Life Contingencies." *Philosophical Transactions of the Royal Society of London*, 115, 513-583.

Goto, S.Tatsuoka, F.Shibuya, S.Kim, Y. S. and Sato, T. (1991). "A simple gauge for local strain measurements in the laboratory." *Soil and foundations*, 31(1), 149-167.

Greenspan, M. (1944). "Effect of a small hole on the stresses in a uniformly loaded plate." *Quarterly Applied Math*, 2(1), 60-71.

Gregory, A. S.Whalley, W. R.Watts, C. W.Bird, N. R. A.Hallett, P. D. and Whitmore, A. P. (2006). "Calculation of the compression index and precompression stress from soil compression test data." *Soil and Tillage Research*, 89(1), 45-57.

Griffiths, D. V. (1982). "Computation of bearing capacity factors using finite elements." *Geotechnique*, 32(3), 195-202.

Griffiths, F. J. and Joshi, R. C. (1990). "Clay Fabric Response to Consolidation " *Applied Clay Science*, 5(1), 37-66.

Grozic, J. L. H., Lunne, T., and Pande, S. (2003). "An oedometer test study on the preconsolidation stress of glaciomarine clays." *Canadian Geotechnical Journal*, 40(5), 857-872.

Guedes, P. F. M. and Santos Pereira, C. (2000). "The role of the soil k0 value in numerical analysis of shallow tunnels." *Proceedings of International Symposium on Geotechnical Aspects of Underground Construction in Soft Ground, Rotterdam*, 379-384.

Hansen, J. B. (1969). "A mathematical model for creep phenomena in clay." *Proceeding of 7th International Conference on Soil Mechenics and Foundation Engineering*, Specialty Session 12, 12-18.

Hansen, J. B. (1970). *A revised and extended formula for bearing capacity*, Bulletin No. 28, Danish Geotechnical Institute.

Hanzawa, H. (1989). "Evaluation of design parameters for soft clays as related to geological stress history." *Journal of the Japanese Geotechnical Society, Soils and Foundations*, 29(2), 99-111.

Hardin, B. (1987). "1D Strain in Normally Consolidated Cohesionless Soils." *Journal of Geotechnical Engineering*, 113(12), 1449-1467.

Hardin, B. O. (1978). "The nature of stress-strain behaviou for soils. State-of-the-art report." *Proceedings of the ASCE Geotechnical Engineering Division Specialty Conference*, Vol. 1, 3-90.

Hashash, Y. M. A., Phillips, C., and Groholski, D. R. (2010). "Recent advances innon-linearsiteresponseanalysis." *Fifth international conference on recent advances in geotechnical engineering and soil dynamics*, San Diego.

Hendron, A. J. (1963). "The Behavior of Sand in One Dimensional Compression." Ph.D, University of Illinois, Urbana, USA.

Hendron, A. J., Jr.Mesri, G.Gamble, J. C. and Way., G. (1969). "Compressibility Characteristics of Shales Measured by Laboratory and In Situ Tests." *ASTM STP 477*, 137- 153.

Hight, D. W.Böese, R.Butcher, A. P.Clayton, C. R. I. and Smith, P. R. (1992). "Disturbance of the Bothkennar clay prior to laboratory testing." *Geotechnique*, 42(2), 199-217.

Hjiaj, M., Lyamin, A. V., and Sloan, S. W. (2005). "Numerical limit analysis solutions for the bearing capacity factor Nγ." *International Journal of Solids and Structures*, 42(5–6), 1681-1704.

Hollowell, W. T., Pilkey, W. D., and Sieveka, E. M. (1988). "System identification of dynamic structures." *Finite Elements in Analysis and Design*, 4(1), 65-77.

Hong, Z., Tateishi, Y., and Han, J. (2006). "Experimental Study of Macro- and Microbehavior of Natural Diatomite." *Journal of Geotechnical And Geoenvironmental Engineering*, 132(5), 603-610.

Hong, Z. S., Yin, J., and Cui, Y. J. (2010). "Compression behaviour of reconstituted soils at high initial water contents." *Geotechnique*, 60(9), 691-700.

Hong, Z. S.Zeng, L. L.Cui, Y. J.Cai, Y. Q. and Lin, C. (2012). "Compression behaviour of natural and reconstituted clays." *Geotechnique*, 62(4), 291-301.

Houlsby, G. T. and Wroth, C. P. (1991). "The variation of shear modulus of a clay with pressure and overconsolidation ratio." *Soils and Foundations*, 31(3), 138–143.

Houlsby, G. T. and Wroth, C. P. (1991). "The variation of shear modulus of a clay with pressure and overconsolidation ratio." *Soil Mechanics and Foundation Engineers*, 31(3), 138-143.

Hsieh, C. W. (1991). "Footing behavior and stability analysis method for strip surface footing above continuous circular void."Ph.D., The Pennsylvania State University, Ann Arbor.

Iwasaki, T., Tatsuoka, F., and Takagi, Y. (1978). "Shear moduli of sands under cyclic torsional shear loading." *Soil and Foundations*, 18(1), 39-56.

Jacobsz, S. W.Standing, J. R.Mair, R. J.Hagiwara, T. and Sugiyama, T. (2004). "Centrifuge modelling of tunnelling near driven piles." *Soils and Foundations*, 44(1), 49-56.

Jamiolkowski, M.Lancellotta, R.LoPresti, D. C. F. and Pallara, O. (1994). "Stiffness of Toyoura sand at small and intermediate strain." *Proceeding of the 13th International Conference on Soil Mechanics and Foundation Engineering, New Delhi*, 1, 169-172.

Janbu, N. "The resistance concept applied to deformation of soils." *Proc., Proceedings of the 7th International Conference on Soil Mechanics and Foundation Engineering*, Balkema, Rotterdam, the Netherlands, 191-196.

Jardine, R. J., Symes, M. J., and Burland, J. B. (1984). "The Measurement of soil stiffness in the triaxial apparatus." *Geotechnique*, 34(3), 323-340.

Jardine, R. J.Potts, D. M.Fourie, A. B. and Burland, J. B. (1986). "Studies of the influence of non-linear stress-strain characteristics in soil-structure interaction." *Geotechnique*, 36(3), 377-396.

Jose, B. T., Sridharan, A., and Abraham, B. M. (1989). "Log-log method for determination of preconsolidation pressure." *ASTM Geotechnical Testing Journal*, 12(3), 230-237.

Jovičić, V. and Coop, M. R. (1997). "Stiffness of coarse-grained soils at small strains." *Geotechnique*, 47(3), 545-561.

Juárez-Badillo, E. (1981). "General compressibility equation for soils." *Proceedings of the 10th International Conference on Soil Mechanics and Foundation Engineering, Stockholm, Sweden*, Vol. 1, 171-178.

Karig, D. E. and Hou, G. (1992). "High-stress consolidation experiments and their geologic implications." *Journal of Geophysical Research: Solid Earth*, 97(B1), 289-300.

Kaufman, R. I. and Sherman, W. C., JR. (1964). "Engineering Measurements for the Port Allen Lock." *Journal of the Soil Mechanics and Foundations Division*, 90(5), 221-248.

Kavanagh, K. T. (1973). "Experiment versus analysis: computational techniques for the description of static material response." *International Journal for Numerical Methods in Engineering*, 5, 503-515.

Kirsch, G. (1898). "Die theorie der elastizitat und die bedurfnisse der festigkeitslehre." *Zeitschrift des Vereines deutscher Ingenieure*, 42(28), 797-807.

Kochanov, W. E. (1999). "Sinkholes in Pennsylvania: Pennsylvania Geological Survey." *Educational Series 11*, Department of Conservations and Natural resources.

Koiter, W. T. (1960). *General theorems for elastic-plastic solids*, Amsterdam, The Netherlands.

Kondner, R. L. (1963). "Hyperbolic Stress-Strain Response: Cohesive Soils." *Journal of the Soil Mechanics and Foundations Division, Proceedings of the American Society of Civil Engineers*, 89(1), 115-143.

Ku, T. and Mayne, P. W. (2013). "Yield stress history evaluated from paired in-situ shear moduli of different modes." *Engineering Geology*, 152(1), 122-132.

Kulhawy, F. H. (2004). "On the Axial Behavior of Drilled Foundations." *GeoSupport 2004, ASCE, GSP 124*, 34-51.

Ladd, C. C. and DeGroot, D. J. (2003). "Recommended practice for soft ground site characterization: The Arthur Casagrande Lecture." *Proceedings of the 12th Panamerican Conference on Soil Mechanics and Geotechnical Engineering, USA*, Cambridge, MA, 1-55.

Larrahondo, J. M. (2011). "Carbonate diagenesis and chemical weathering in the southeastern United States: some implications on geotechnical behavior." Ph.D. thesis., School of Civil and Environmental Engineering, Georgia Institute of Technology.

Lehane, B. and Cosgrove, E. (2000). "Applying triaxial compression stiffness data to settlement prediction of shallow foundations on cohesionless soil." *Proceedings of the ICE - Geotechnical Engineering*, 143(4), 191-200.

Leoni, M., Karstunen, M., and Vermeer, P. A. (2008). "Anisotropic creep model for soft soils." *Geotechnique*, 58(3), 215-226.

Leroueil, S.Roy, M.La Rochelle, P.Brucy, F. and Tavenas, F. (1979). "Behavior of destructured natural clays." *Journal of the Geotechnical Engineering Division*, 105(6), 759-778.

Leroueil, S., Tavenas, F., and Locat, J. (1985). "Discussion: Correlations between index tests and the properties of remoulded clays." *Geotechnique*, 35(2), 223-226.

Leroueil, S. (1996). "Compressibility of Clays: Fundamental and Practical Aspects." *Journal of Geotechnical Engineering*, 122(7), 534-543.

Loukidis, D. and Salgado, R. (2009). "Bearing capacity of strip and circular footings in sand using finite elements." *Computers and Geotechnics*, 36(5), 871-879.

Lunne, T. and Long, M. (2006). "Review of long seabed samplers and criteria for new sampler design." *Marine Geology*, 226(1–2), 145-165.

Luong, M. P. (1980). "Stress-strain aspects of cohesionless soils under cyclic and transient loading." *Proceeding of the International Symposium on Soils under cyclic and transient loading*, Rotterdam, Netherlands, 315-324.

Lutenegger, A. J. and Adams, M. T. (1998). "Bearing capacity of footings on compacted sand." *Procedings of 4th International Conference on Case Histories in Geotechnical Engineering, St. Louis, Missouri, USA*, 1216-1224.

Mair, R. J., Gunn, M. J., and O'Reilly, M. P. (1981). "Ground movements around shallow tunnels in soft clay." *Proceedings of 10th International Conference on Soil Mechanics and Foundation Engineering, Stockholm*, 1, 323-328.

Mair, R. J. (1993). "Developments in geotechnical engineering research: applications to tunnels and deep excavations. Unwin Memorial Lecture 1992." *Proceedings of Institution of Civil Engineers, Civil Engineering*, Vol. 97, 27-41.

Mair, R. J., Taylor, R. N., and Bracegirdle, A. (1993). "Subsurface settlement profiles above tunnels in clays." *Geotechnique*, 43(2), 315-320.

Mair, R. J. (2008). "Tunnelling and geotechnics: new horizons." *Geotechnique*, 58(9), 695-736.

Manoharan, N. and Dasgupta, S. P. (1995). "Bearing capacity of surface footings by finite elements." *Computers & Structures*, 54(4), 563-586.

Marshall, A. M.Farrell, R.Klar, A. and Mair, R. J. (2012). "Tunnels in sands: the effect of size, depth and volume loss on greenfield displacements." *Geotechnique*, 62(5), 385-399.

Mayne, P. W. and Kulhawy, F. H. (1982). "k_0-OCR relationships in soil." *Journal of Geotenical Engineering Division*, 108(6), 851-872.

Mayne, P. W. and Holtz, R. D. (1985). "Effect of principal stress rotation on clay strength." *Proceeding of the 11th International Conference on Soil Mechanics and Foundation Engineering, SanFrancisco*, Vol. 2, 579-582.

Mayne, P. W. (1994). "CPT-based prediction of footing response." *Predicted and Measured Behavior of Five Spread Footings on Sand, GSP 41*, 214-218.

Mayne, P. W.Coop, M. R.Springman, S. M.Huang, A.-B. and Zornberg, J. G. (2009). "Geomaterial behavior and testing." *Proceeding of the 17th International Conference on Soil Mechanics and Foundation Engineering, Alexandria, Egypt*, Vol. 4, 2777-2872.

Mayne, P. W. and Woeller, D. J. (2014). "Generalized Direct CPT Method for Evaluating Footing Deformation Response and Capacity on Sands, Silts, and Clays." *Geo-Congress 2014 Technical Papers*, 1983-1997.

Mesri, G. and Olson, R. E. (1971). "Consolidation Characteristics of Montmorillonite." *Geotechnique*, 21(4), 341-352.

Mesri, G., Rokhsar, A., and Bohor, B. F. (1975). "Composition and compressibility of typical samples of Mexico City clay." *Geotechnique*, 25(3), 527-554.

Mesri, G. and Godlewski, P. M. (1977). "Time and Stress Compressibility Inter relationship." *Journal of the Geotechnical Engineering Division*, 103(GT5), 417-430.

Mesri, G. and Castro, A. (1987). "Concept and During Secondary Compression." *Journal of Geotechnical Engineering*, 113(3), 230-247.

Meyerhof, G. G. (1963). "Some recent research on the bearing capacity of foundations." *Canadian Geotechnical Journal*, 1(1), 16-26.

Mitchell, J. K. (1976). *Fundamentals of soil behavior*, Wiley, New York.

Moh, Z. C., Daniel, H. J., and Hwang, R. N. (1996). "Ground movements around tunnels in soft ground." *Proceedings of International Symposium on Geotechnical Aspects of Underground Construction in Soft Ground, London*, 36-42.

Morgan, K. and Ntambakwa, E. (2008). "Wind Turbine Foundations Behavior and Design Considerations." *American Wind Energy Association Windpower Conference, Houston, USA.*

Morris, P. H. (2002). *Geotechnical compressibility and consolidation parameters and correlations for remoulded fine-grained marine and riverine sediments / by Peter Morris and David Lockington*, CRC for Sustainable Tourism, Gold Coast, Qld.

Muir Wood, D. (1990). *Soil behaviour and critical state soil mechanics*, Cambridge University Press.

Nagaraj, T. S. and Murthy, B. R. S. (1986). "A critical reappraisal of compression index equations " *Geotechnique* 36(1), 27-32.

Narsilio, G. A. and Santamarina, J. C. (2008). "Terminal densities." *Geotechnique*, 58(8), 669-674.

Niemunis, A., Wichtmann, T., and Triantafyllidis, T. (2005). "A high-cycle accumulation model for sand." *Computers and Geotechnics*, 32(4), 245-263.

O' Reilly, M. P. and New, B. M. (1982). "Settlements above tunnels in the United Kingdom: their magnitude and prediction." *Proceedings of Tunneling*, 173-181.

Oikawa, H. (1987). "Compression curve of soft soils " *Journal of the Japanese Geotechnical Society, Soils and Foundations*, 27(3), 99-104.

Onitsuka, K.Hong, Z.Hara, Y. and Shigeki, Y. (1995). "Interpretation of oedometer test data for natural clays." *Journal of the Japanese Geotechnical Society, Soils and Foundations*, 35(3), 61-70.

Osipov, V. I., Bik, N. N., and Rumjantseva, N. A. (1987). "Cyclic swelling of clays." *Applied Clay Science*, 2(4), 363-374.

Pacheco, S. F. (1970). "A new graphical construction for determination of the preconsolidation stress of a soil sample." *Proceedings of the 4th Brazilian Conference of Soil Mechanics and Foundation Engineering*, 2(1), 225-232.

Pang, C. H., Yong, K. Y., and Dasari, G. R. (2005). "Some considerations in finite element analysis of tunnelling." *Proceedings of the International World Tunnel Congress and the 31st ITA General Assembly*Istanbul, Turkey.

Pasten, C. and Santamarina, J. C. (2011). "Energy geo-storage - analysis and geomechanical implications." *KSCE J Civ Eng*, 15(4), 655-667.

Pasten, C., Shin, H., and Santamarina, J. (2014). "Long-Term Foundation Response to Repetitive Loading." *Journal of Geotechnical and Geoenvironmental Engineering*, 140(4), 04013036.

Peck, R. B. (1969). "Deep Excavations and Tunneling in Soft Ground." *Proceedings of the 7th International Conference on Soil Mechanics and Foundation Engineering, Mexico City*, 225 - 290.

Pejon, O. J. and Zuquette, L. V. (2002). "Analysis of cyclic swelling of mudrocks." *Engineering Geology*, 67(1–2), 97-108.

Perret, D., Locat, J., and Leroueil, S. (1995). "Strength development with burial in fine-grained sediments from the Saguenay Fjord, Quebec." *Canadian Geotechnical Journal*, 32(2), 247-262.

Pestana, J. M. and Whittle, A. J. (1995). "Compression model for cohesionless soils." *Geotechnique*, 45(4), 611-631.

Potts, D. M. (2003). "Numerical analysis: a virtual dream or practical reality?" *Geotechnique*, 53(6), 535-573.

Puzrin, A. M. and Burland, J. B. (1996). "A logarithmic stress-strain function for rocks and soils." *Géotechnique*, 46(1), 157-164.

Puzrin, A. M. and Burland, J. B. (1998). "Non-linear model of small-strain behaviour of soils." *Géotechnique*, 48(2), 217-213.

Quigley, R. M. and Thompson, C. D. (1966). "The Fabric of Anisotropically Consolidated Sensitive Marine Clay." *Canadian Geotechnical Journal*, 3(2), 61-73.

Rajendran, S. (2010). "A technique to develop mesh-distortion immune finite elements." *Computer Methods in Applied Mechanics and Engineering*, 199(17–20), 1044-1063.

Ramberg, W. and Osgood, W. R. (1943). "Description of stress-strain curves by three parameters." *Technical Note No. 902, National advisory committee for aeronautics*.

Rampello, S., Viggiani, G. M. B., and Amorosi, A. (1997). "Small-strain stiffness of reconstituted clay compressed along constant triaxial effective stress ratio paths." *Géotechnique*, 47(3), 475-489.

Rinaldi, V. A. and Santamarina, J. C. (2008). "Cemented soils: small strain stiffness." *Proceeding of the 4th International Symposium on Deformational Characteristics of Geomaterials, Atlanta, Georgia, USA*, Vol. 1, 267-274.

Rochelle, P. L.Sarrailh, J.Tavenas, F.Roy, M. and Leroueil, S. (1981). "Causes of sampling disturbance and design of a new sampler for sensitive soils." *Canadian Geotechnical Journal*, 18(1), 52-66.

Rodrıguez-Roa, F. (2000). "Observed and calculated load–settlement relationship in a sandy gravel." *Canadian Geotechnical Journal*, 37(2), 333-342.

Rodrıguez-Roa, F. (2002). "Ground Subsidence due to a Shallow Tunnel in Dense Sandy Gravel." *Journal of Geotechnical and Geoenvironmental Engineering*, 128(5), 426-434.

Roscoe, K. H. and Burland, J. B. (1968). *On the generalized stress–strain behaviour of wet clay.*, London: Cambridge University Press.

Rouse, P. C. (2010). "Comparison of methods for the measurement of the angle of repose of granular materials." *Geotechnical Testing Journal*, 37(1), 1-5.

Rowe, P. W. and Peaker, K. (1965). "Passive earth pressure measurements." *Geotechnique*, 15(1), 57-78.

Sakurai, S. and Takeuchi, K. (1983). "Back analysis of measured displacements of tunnels." *Rock Mech Rock Engng*, 16(3), 173-180.

Sallfors, G. (1975). "Preconsolidation Pressure of Soft Highly Plastic Clays." Ph.D. Dissertation, Chalmers University of Technology, Gothenburg, Sweden.

Santagata, M. and Germaine, J. (2002). "Sampling Disturbance Effects in Normally Consolidated Clays." *Journal of Geotechnical and Geoenviromental Engineering*, 128(12), 997-1006.

Santamarina, J. C. and Cascante, G. (1996). "Stress anisotropy and wave propagation: a micromechanical view." *Canadian Geotechnical Journal*, 33(5), 770-782.

Santamarina, J. C., Klein, K. A., and Fam, M. A. (2001). *Soils and waves*, Wiley, Chichester, England.

Santamarina, J. C. and Fratta, D. (2005). *Discrete Signals and Inverse Problems: An Introduction for Engineers and Scientists*, ASCE Press.

Santamarina, J. C. and Shin, H. S. (2009). "Frictional Phenomena in Granular Media." *Meso-scale Shear Physics in Earthquake and Landslide Mechanics, Editors: Y.H. Hatzor, J. Sulem, I. Vardoulakis, CRC Press*, 157-188.

Sawczuk, A. (1974). "Shakedown analysis of elastic-plastic structures." *Nuclear Engineering and Design*, 28(1), 121-136.

Sawicki, A. (1994). "Elasto-plastic interpretation of oedometric test." *Archives of Hydro-Engineering and Environmental Mechanics*, 41(1-2), 111-131.

Sawicki, A. and Swidzinski, W. (1995). "Cyclic compaction of soils, grains and powders." *Powder Technology*, 85(2), 97-104.

Schmertmann, J. (1983). "A Simple Question About Consolidation." *Journal of Geotechnical Engineering*, 109(1), 119-122.

Schmertmann, J. (1984). "Closure to "A Simple Question about Consolidation" by John M. Schmertmann (January, 1983)." *Journal of Geotechnical Engineering*, 110(5), 673-673.

Schmertmann, J. (1991). "The Mechanical Aging of Soils." *Journal of Geotechnical Engineering*, 117(9), 1288-1330.

Schmertmann, J. M. (1955). "The undisturbed consolidation behavior of clay." *Transactions American Society of Civil Engineers*, 120(1), 1201-1233.

Schmidt, B. (1969). "Settlements and ground movements associated with tunneling in soil." Ph.D., University of Illinois at Urbana-Champaign.

Schofield, A. N. and Wroth, C. P. (1968). *Critical state soil mechanics*, McGraw-Hill.

Shannon and Wilson, I. (2007). "Geotechnical Engineering Report - Geotechnical Investigation Phase II: Salt Waste Processing Facility." U.S. Department of Energy.

Sharp, R. and Booker, J. (1984). "Shakedown of Pavements Under Moving Surface Loads." *Journal of Transportation Engineering*, 110(1), 1-14.

Shin, H. S. and Santamarina, J. C. (2009). "Mineral Dissolution and the Evolution of k0." *Journal of Geotechnical and Geoenvironmental Engineering*, 135(8), 1141-1147.

Skempton, A. W. (1944). "Notes on compressibility of clays." *Quarterly Journal of the Geological Society, London*, 100(2), 119-135.

Skempton, A. W. (1969). "The consolidation of clays by gravitational compaction." *Quarterly Journal of the Geological Society*, 125(1-4), 373-411.

Sridharan, A., Abraham, B. M., and Jose, B. T. (1991). "Improved technique for estimation of preconsolidation pressure." *Geotechnique*, 41(2), 263-268.

Sridharan, A. and Nagaraj, A. B. (2000). "Compressibility behaviour of remoulded, fine grained soils and correlation with index properties." *Canadian Geotechnical Journal*, 37(3), 712–722

Sridharan, A. and Nagaraj, H. B. (2000). "Compressibility behaviour of remoulded, fine-grained soils and correlation with index properties." *Canadian Geotechnical Journal*, 37(3), 712-722.

SRNS (2011). "Settlement of the vitrification building at the Defense Waste Processing Facility: K-ESR-S Area." U.S. Department of Energy.

Stokoe, K. H. and Santamarina, J. C. (2000). "Seismic-Wave-Based Testing in Geotechnical Engineering." *GeoEng 2000* Melbourne, Australia, November, pp. 1490-1536 (State-of-the-Art).

Sultan, N., Delage, P., and Cui, Y. J. (2002). "Temperature effects on the volume change behaviour of Boom clay." *Engineering Geology*, 64(2–3), 135-145.

Tatsuoka, F.Jardine, R. J.LoPresti, D.DiBenedetto, H. and Kodaka, T. (1997). "Theme lecture: characterising the pre-failure deformation properties of geomaterials." *Proceeding of the 14th International Conference on Soil Mechanics and Foundation Engineering, Hamburg, Germany*, Vol. 4, 2129-2164.

Terzaghi, K. (1943). *Theoretical Soil Mechanics*, John Wiley & Sons, New York.

Terzaghi, K. and Peck, R. B. (1948). *Soil Mechanics in Engineering Practice*, John Wiley and Sons, New York

Terzaghi, K. and Richart, R. E. (1952). "Stresses in Rock About Cavities." *Geotechnique*, 3(2), 57-90.

Thomann, T. G. and Hryciw, R. D. (1990). "Laboratory measurement of small strain shear modulus under ko conditions." *Geotechnical Testing Journal*, 13(2), 97-105.

Tripathy, S. and Subba Rao, K. (2009). "Cyclic Swell–Shrink Behaviour of a Compacted Expansive Soil." *Geotech Geol Eng*, 27(1), 89-103.

Vardanega, P. and Bolton, M. (2013). "Stiffness of Clays and Silts: Normalizing Shear Modulus and Shear Strain." *Journal of Geotechnical and Geoenvironmental Engineering*, 139(9), 1575-1589.

Verruijt, A. and Booker, J. R. (1996). "Surface settlements due to deformation of a tunnel in an elastic half plane." *Geotechnique*, 46(4), 753-756.

Vesic, A. S. (1973). "Analysis of ultimate loads of shallow foundations." *Journal of Soil Mechanics and Foundation Division*, 93(SM3), 45-73.

Viggiani, G. and Atkinson, J. H. (1995). "Stiffness of fine-grained soil at very small strains." *Geotechnique*, 45(2), 249-265.

Viklander, P. (1998). "Permeability and volume changes in till due to cyclic freeze/thaw." *Canadian Geotechnical Journal*, 35(3), 471-477.

Vorster, T.Klar, A.Soga, K. and Mair, R. (2005). "Estimating the Effects of Tunneling on Existing Pipelines." *Journal of Geotechnical and Geoenvironmental Engineering*, 131(11), 1399-1410.

Vucetic, M. and Dobry, R. (1991). "Effect of Soil Plasticity on Cyclic Response." *Journal of Geotechnical Engineering*, 117(1), 89-107.

Walton, W. H., Sangrey, D. A., and Miller, S. A. (1983). "Geotechnical Engineering Characterization of Hydraulically Piston-Cored Deep Ocean Sediments." *Deep Sea Drilling Project Reports*, 72, 537-549.

Wang, M. C. and Badie, A. (1985). "Effect of underground void on foundation stability." *Journal of Geotechnical Engineering*, 111(8), 1008-1019.

Wang, M. C. and Hsieh, C. W. (1987). "Collapse Load of Strip Footing Above Circular Void." *Journal of Geotechnical Engineering*, 113(5), 511-515.

Wichtmann, T., Niemunis, A., and Triantafyllidis, T. (2007). "On the influence of the polarization and the shape of the strain loop on strain accumulation in sand under high-cyclic loading." *Soil Dynamics and Earthquake Engineering*, 27(1), 14-28.

Wichtmann, T., Niemunis, A., and Triantafyllidis, T. (2010). "On the determination of a set of material constants for a high-cycle accumulation model for non-cohesive soils." *International Journal for Numerical and Analytical Methods in Geomechanics*, 34(4), 409-440.

Wichtmann, T., Niemunis, A., and Triantafyllidis, T. (2010). "Strain accumulation in sand due to drained cyclic loading: On the effect of monotonic and cyclic preloading (Miner's rule)." *Soil Dynamics and Earthquake Engineering*, 30(8), 736-745.

Woodward, P. K. and Griffiths, D. V. (1998). "Observations on the computation of the bearing capacity factor Nγ by finite elements." *Geotechnique*, 48(1), 137-141.

WSRC (1999). "Historical review of significant investigations and current understanding of soft zone origin, extent and stability." *Project Report*, U.S. Department of Energy.

WSRC (2007). "Salt Waste Processing Facility Dynamic Settlement Evaluation." U.S. Department of Energy.

Yeo, B. Das, B. M. Yen, S. C. and Puri, V. K. (1994). "Permanent settlement of shallow foundation on sand due to cyclic loading " *Proceeding of the International Symposium on Pre-failure deformation characteristics of geomaterials, Sapporo, Japan*, Vol. 1, 635 - 640.

Yoon, H.-K.Lee, C.Kim, H.-K. and Lee, J.-S. (2011). "Evaluation of preconsolidation stress by shear wave velocity." *Smart Structures and Systems*, 7(4), 275-287.

Yun, T. and Santamarina, J. (2005). "Decementation, Softening, and Collapse: Changes in Small-Strain Shear Stiffness in Loading." *Journal of Geotechnical and Geoenvironmental Engineering*, 131(3), 350-358.